sciendo

Contributions to Geophysics and Geodesy Vol. 49/1, 2019 (1–10)

Seismic activity on the territory of Slovakia in 2016

Róbert KYSEL[1,2,*], Andrej CIPCIAR[1,2], Zuzana CHOVANOVÁ[1,3], Kristián CSICSAY[1], Lucia FOJTÍKOVÁ[1,4], Martin GÁLIS[1,2], Miriam KRISTEKOVÁ[1,2]

[1] Earth Science Institute of the Slovak Academy of Sciences, Dúbravská cesta 9, P. O. Box 106, 840 05 Bratislava, Slovak Republic

[2] Faculty of Mathematics, Physics and Informatics, Comenius University in Bratislava, Mlynská dolina, 842 48 Bratislava, Slovak Republic

[3] Faculty of Natural Sciences, Comenius University in Bratislava, Mlynská dolina, Ilkovičova 6, 842 15 Bratislava, Slovak Republic

[4] Institute of Rock Structure and Mechanics of the Czech Academy of Sciences, V Holesovickach 94/41, 182 09, Prague 8, Czech Republic

Abstract: The National Network of Seismic Stations of Slovakia (NNSS) consists of eight short period and five broadband permanent seismic stations and a data centre located at the Earth Science Institute of the Slovak Academy of Sciences (ESI SAS). The NNSS recorded and detected 10888 seismic events from all epicentral distances in 2016. Totally 87 earthquakes originated in the territory of Slovakia in 2016. This paper provides basic information on the configuration of the NNSS, routine data processing, seismic activity on the territory of Slovakia in 2016 as well as macroseismic observations collected in 2016.

Key words: Slovakia, National Network of Seismic Stations, seismicity, macroseismic observations

1. Introduction

The seismic activity on the territory of Slovakia and adjacent areas has been reported on the daily basis by the so-called Seismo Reports published on the web sites of the Department of Seismology, ESI SAS `http://www.seismology.sk/Seismo_Reports/reports.html` and in annual reports as a part of the project Partial monitoring system – Geological factors (*Liščák et al., 2017*) which is solved with a contract between ESI SAS and State Geological Institute of Dionýz Štúr. The aim of this paper is to provide a quick

*corresponding author: e-mail: robert.kysel@savba.sk

doi: 10.2478/congeo-2019-0001

overview of earthquakes which originated on the territory of Slovakia or were macroseismically felt on the territory of Slovakia in 2016.

2. Seismic stations operating in 2016

The seismic monitoring of the Slovak territory is provided by the NNSS operated by the ESI SAS (*ESI SAS, 2004*), *Local Seismic Network in Eastern Slovakia* operated by the Faculty of Mathematics, Physics and Informatics of the Comenius University in Bratislava and local network of seismic stations around NPPs Jaslovské Bohunice and Mochovce operated by Progseis Ltd. company. The networks of seismic stations cooperate and the exchange of data is on the regular basis. The positions of the seismic stations on the territory of Slovakia are shown in Fig. 1.

In 2016 the NNSS consisted of thirteen permanent seismic stations, from which eight are short period and five are broadband. Broadband stations are: Červenica (CRVS), Kolonické sedlo (KOLS), Modra (MODS), Vyhne (VYHS) and Železná studnička (ZST). Short period stations are: Hurbanovo (HRB), Iža (SRO1), Kečovo (KECS), Liptovská Anna (LANS), Moča (SRO2), Stebnícka Huta (STHS) and Šrobárová (SRO). The HRB

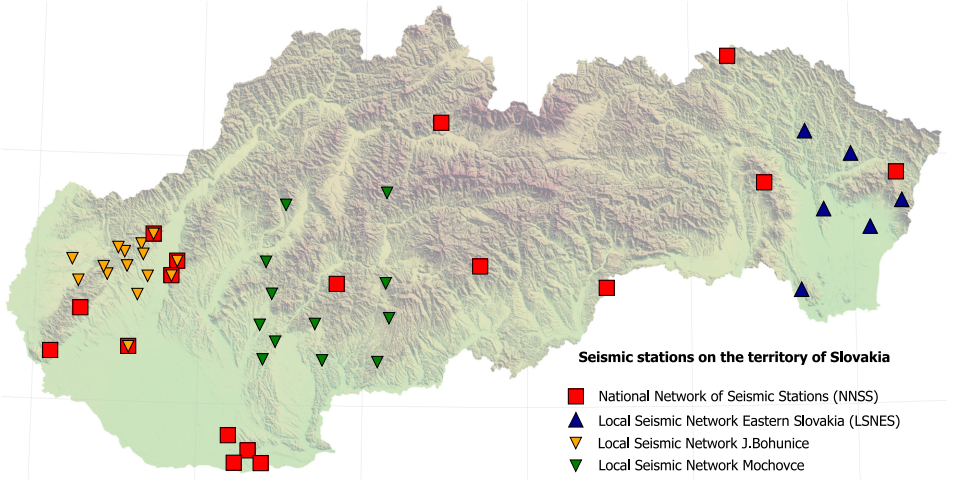

Fig. 1. Seismic stations operational on the territory of Slovakia in 2016.

is the oldest NNSS seismic station that has been in operation since 1909 (*Pajdušák, 1997*). In 2016, the seismic station Izabela (IZAB) has been added to the NNSS as a new permanent short period seismic station. This station has been jointly operated by ESI SAS and Progseis Ltd. company. In this year the seismic station MODS has been upgraded with a 6-channel 32-bit digitizer and an EpiSensor has been installed. The NNSS permanent seismic stations and their instrumentation are summarized in Table 1. More details can be found on the web page `http://www.seismology.sk/National_Network`.

Table 1. Equipment of seismic stations of the NNSS operating in 2016.

Station	**ISC code**	**Lat. [°N]**	**Long. [°E]**	**Alt. [m]**	**Sensor**	**DAS**	**Sampl. freq.**	**Data format**
Bratislava Žel. Studnička	ZST	48.196	17.102	250	3×SKD	Wave24	100/sec	mSEED
Červenica	CRVS	48.902	21.461	476	STS-2	Wave24	100/sec	mSEED
Vyhne	VYHS	48.493	18.836	450	STS-2	Wave24	100/sec	mSEED
Modra-Piesok	MODS	48.373	17.277	520	STS-2	Wave32	100/sec	mSEED
Hurbanovo	HRB	47.873	18.192	115	2× Mainka	Analog	–	smoked paper
Izabela	IZAB	48.569	19.713	450	3×SM3	Wave24	100/sec	mSEED
Iža	SRO1	47.7622	18.2328	111	ViGeo	Gaia	100/sec	mSEED
Kečovo	KECS	48.483	20.486	345	LE3D	Wave24	100/sec	mSEED
Kolonické sedlo	KOLS	48.933	22.273	460	Guralp-6T-30s	Wave32	100/sec	mSEED
Liptovská Anna	LANS	49.151	19.468	710	LE3D	SEMS	100/sec	mSEED
Moča	SRO2	47.763	18.394	109	Guralp-40T-1s	Wave24	100/sec	mSEED
Stebnícka Huta	STHS	49.417	21.244	534	LE3D	Wave24	100/sec	mSEED
Šrobárová	SRO	47.813	18.313	150	3× SKM-3	Wave24	100/sec	mSEED

Four additional short period seismic stations has been operated on the jointly bases of ESI SAS and the other institutions. The seismic stations Banka (BAN), Podolie (POD) and Jalšové (JAL) located in the Little Carpathians has been operated in cooperation with Progseis Ltd. company and the Institute of Rock Structure and Mechanics of the Czech Academy of Sciences (IRSM CAS) (*Fojtíková et al., 2015*). The seismic station Pusté Úľany (PULA) has been operated in cooperation with the IRSM CAS. These stations have been installed as temporary seismic stations.

3. Data processing

Digital data from all NNSS stations (except the analog seismic station HRB) are transfered in real-time to the data centre at the ESI SAS either by the internet or satelite telemetry. Software package SeisComp3 (*Weber et al., 2007*) and SeedLink server are used for data acquisition and exchange.

Beside observations from the NNSS stations the data centre at ESI SAS also use the data from the above mentioned local networks of seismic stations in Slovakia and observations from networks of neighbouring countries: Austrian Seismic Network (*ZAMG – Zentralanstalt für Meterologie und Geodynamik, 1987*), Czech Regional Seismic Network (*Institute of Geophysics, Academy of Sciences of the Czech Republic, 1973*), Hungarian National Seismological Network (*Kövesligethy Radó Seismological Observatory, 1992*), Local seismological network for monitoring NPP Dukovany (*Institute of Physics of the Earth Masaryk University, 2014*), GEOFON Seismic Network (*GEOFON Data Center, 1993*), *Polish Seismological Network*. These stations forms a so-called Regional Virtual Network of ESI SAS that consists of approximately 55 seismic stations.

Routine analysis of the digital recordings at the ESI SAS has been performed by the Unix package Seismic handler (*Stammler, 1993*). Interactive locations of seismic events within Seismic Handler are performed by external program LocSat. The collected digital observations are manually processed on the daily basis. The epicentre locations are based on the IASPI91 traveltime curves. Local magnitudes has been determined from the maximum vertical trace amplitudes of Sg waves, using the pre-defined Seismic Handler formula for local events. Continuous raw seismic data from the NNSS are stored in a local archive and seismic data interpretations (together with information on equipment of stations) are stored in a web accessible database.

4. Seismic activity in 2016

The NNSS analyzed 10888 local, regional and teleseismic events in 2016. More than 40600 seismic phases were determined. Seismic events identified as quarry blasts were excluded from further processing and were not

included in the event statistics. All events recorded by the NNSS and analyses at the data centre at ESI SAS has been reported in the so-called Seismo Reports and published on the above mentioned web sites of the Department of Seismology, ESI SAS.

Altogether 87 seismic events located by the NNSS originated in the territory of Slovakia in 2016 (Fig. 2). Known quarry blasts are not included in this number. 28 earthquakes reached local magnitude 1.0 or more and are listed in Table 2. The strongest earthquake was detected on April 18 at 13:20 UTC with local magnitude M_L 1.9.

The seismicity of the Slovak territory is dominated by the Little Carpathians and Komárno seismic source zones. The strongest earthquake in the Little Carpathians source zone was detected on the December 12 at 21:43 UTC with local magnitude M_L 1.4. The strongest earthquake in the Komárno source zone was detected on the June 23 at 21:52 UTC with local magnitude M_L 1.4. Although the low level of seismic activity from the last decades remained unchanged in 2016, these two source zones remains of the primary interest for the monitoring of seismic activity within the territory of Slovakia.

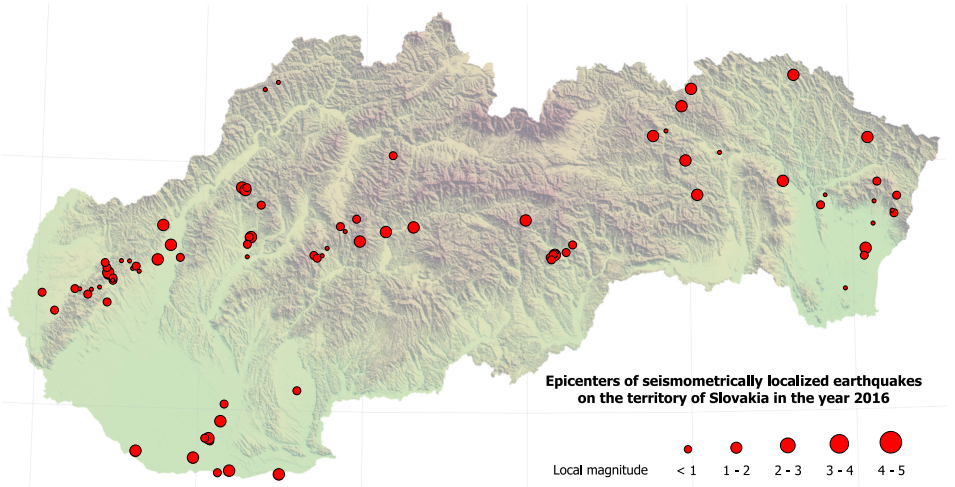

Fig. 2. Map of epicentres of local earthquakes originated on the territory of Slovakia in 2016. Diameters of the circles are proportional to local magnitudes.

Table 2. List of earthquakes originated on the territory of Slovakia in 2016 with $M_L \geq 1.0$.

Date [YYYY-MM-DD]	**Origin Time (UTC) [HH:MM:SS]**	**Lat. [°N]**	**Lon. [°E]**	**Depth [km]**	M_L **[NNSS]**	I_0 **[°EMS]**	**Region**
2016-01-24	22:18:56.83	48.64	20.17	0	1.6		Revúca Highlands
2016-02-13	21:34:17.90	48.75	19.30	0	1.0		Upper Hron River region
2016-03-31	09:10:51.76	47.74	18.50	0	1.2		Šamorín – Komárno – Štúrovo
2016-04-15	12:56:16.97	48.65	22.08	2.4	1.5		Eastern Slovak Lowland
2016-04-15	17:30:25.25	48.70	18.30	0.2	1.0		Strážov Mts.
2016-04-18	13:20:39.86	49.24	20.96	0	1.9		Čergov Mts.
2016-05-03	05:12:59.03	47.88	18.07	0	1.0		Šamorín – Komárno – Štúrovo
2016-05-05	08:18:20.67	49.36	21.66	21.6	1.6		Laborec Highlands
2016-05-29	08:26:21.82	47.80	17.98	1.5	1.1		Šamorín – Komárno – Štúrovo
2016-06-01	05:34:50.91	48.54	17.43	1.9	1.1		Little Carpathians
2016-06-10	07:43:05.26	48.88	21.05	0	1.1		Šariš
2016-06-23	21:52:19.25	47.75	18.20	0	1.4		Šamorín – Komárno – Štúrovo
2016-06-24	08:44:43.24	48.74	17.76	8.3	1.3	3	Little Carpathians
2016-06-25	00:33:01.20	48.73	19.13	0	1.1		Banská Bystrica region
2016-06-30	19:35:51.24	48.60	17.73	2	1.1		Little Carpathians
2016-07-11	10:37:40.28	49.31	21.02	4.2	1.6		Čergov Mts.
2016-07-26	10:46:55.58	48.93	21.58	6	1.1		Slanské Hills
2016-07-30	09:36:11.71	49.10	22.11	0	1.5		Laborec Highlands
2016-08-07	19:20:12.61	48.69	18.97	0	1.4		Kremnica Mts.
2016-08-13	22:30:30.47	48.90	18.24	1	1.3		Strážov Mts.

Table 2. Continued from the previous page.

Date [YYYY-MM-DD]	Origin Time (UTC) [HH:MM:SS]	Lat. [°N]	Lon. [°E]	Depth [km]	M_L [NNSS]	I_0 [°EMS]	Region
2016-08-25	04:58:42.28	47.95	18.14	0	1.3		Šamorín – Komárno – Štúrovo
2016-08-26	23:50:14.51	48.89	18.26	2.4	1.1		Strážov Mts.
2016-09-29	05:58:11.72	48.78	19.99	0	1.3		Muráň Plateau
2016-10-09	20:45:11.06	47.82	17.63	0	1.4		Šamorín – Komárno – Štúrovo
2016-10-17	11:39:51.89	49.02	20.98	7.1	1.6		Šariš
2016-11-25	09:29:47.57	49.12	20.78	0	1.4		Levoča Mts.
2016-12-12	21:43:31.28	48.66	17.81	3.7	1.4		Little Carpathians

5. Macroseismic observations

Two earthquakes were macroseismically felt on the territory of Slovakia in 2016, one with the epicentre in Austria and one with the epicentre on the territory of Slovakia (Table 3). These two earthquakes were also seismometrically observed and processed. Intensities were estimated by the European Macroseismic Scale 1998 (EMS-98) introduced by *Grünthal (1998)*.

The earthquake on April 25 at 10:28 UTC with epicentre near Vienna, Austria and local magnitude 4.1 was macroseismically felt on 9 locations within the territory of Slovakia (Table 4). 12 macroseismic questionnaires were filled. People reported weak trembling or shaking and acoustic effects

Table 3. List of macroseismically observed earthquakes on the territory of Slovakia in 2016.

Date [YYYY-MM-DD]	Origin Time (UTC) [HH:MM:SS]	Lat. [°N]	Lon. [°E]	Depth [km]	M_L [NNSS]	I_0 [°EMS]	Region
2016-04-25	10:28:23.6	48.02	16.16	14.1	4.0	5–6	Austria
2016-06-24	08:44:43.2	48.74	17.76	8.3	1.3	3	Little Carpathians

Table 4. Macroseismic observations for April 25, 2016 earthquake, 10:28 UTC.

Locality	**Lat.** [°**N**]	**Lon.** [°**E**]	**No. of questionnaires**	***I*** [°**EMS-98**]
Bratislava 5	48.111	17.112	3	3
Bratislava 4	48.159	17.052	2	3
Bratislava 1	48.147	17.102	1	3
Galanta	48.198	17.734	1	3
Kolíňany	48.351	18.229	1	3
Orechová Potôň	48.036	17.564	1	3
Pezinok	48.298	17.270	1	3
Modrý Kameň	48.248	19.324	1	felt
Veľká Lomnica	49.112	20.354	1	felt

– rumbling. The maximum intensity on the territory of Slovakia was determined at 3° EMS-98.

The earthquake on June 24 at 8:44 UTC with epicentre in the northern part of Little Carpathians (near Nové Mesto nad Váhom) and local magnitude 1.3 was macroseismically felt on 1 location (Table 5). 2 macroseimic questionnaires were filled. The event was described as a light trembling. The epicentral intensity was determined at 3° EMS-98.

Table 5. Macroseismic observations for June 24, 2016 earthquake, 8:44 UTC.

Locality	**Lat.** [°**N**]	**Lon.** [°**E**]	**No. of questionnaires**	***I*** [°**EMS-98**]
Nové Mesto nad Váhom	48.758	17.829	2	3

6. Conclusion and discussion

The NNSS is operated by the ESI SAS, Bratislava. In 2016 a new seismic station Izabela was added to the NNSS and an EpiSensor was installed in the Little Carpathians source zone in seismic station MODS. Data from all stations (except station HRB) are transferred in real-time to the data centre at Bratislava. Data processing and routine analysis are performed digitally by interactive seismological software Seismic Handler. Digital data

are accessible both on-line and off-line in standard data format. So-called Seismo Reports of seismic events recorded by NNSS are published on the web page of the ESI SAS http://www.seismology.sk/Seismo_Reports/reports.html.

Epicentres and local magnitudes were determined for 87 earthquakes originated in the territory of Slovakia in 2016. Weak seismic activity was recorded from several seismic source zones: Little Carpathians, Komárno, Strážov Mts., Čergov Mts., Revúca Highlands and Vihorlat Mts.

Acknowledgements. The authors have been supported by the Slovak Foundation Grant VEGA 2/0188/15 and The Slovak Research and Development Agency Grant APVV-16-0146.

References

ESI SAS (Earth Science Institute of the Slovak Academy of Sciences), 2004: National Network of Seismic Stations of Slovakia. Deutsches GeoForschungsZentrum GFZ, Other/Seismic Network, doi: 10.14470/FX099882.

Fojtíková L., Kristeková M., Málek J., Sokos E., Csicsay K., Záhradník J., 2015: Quantifying capability of a local seismic network in terms of locations and focal mechanism solutions of weak earthquakes. Journal of Seismology, **20**, 1, 93–106, doi: 10.1007/s10950-015-9512-1.

GEOFON Data Center, 1993: GEOFON Seismic Network. Deutsches GeoForschungsZentrum GFZ, Other/Seismic Network, doi: 10.14470/TR560404.

Grünthal G. (Ed.), 1998: European Macroseismic Scale 1998 EMS-98. Cahiers du Centre Européen de Géodynamique et de Séismologie, **15**, Luxembourg, 101 p., http://gfzpublic.gfz-potsdam.de/pubman/item/escidoc:56109.

Institute of Geophysics, Academy of Sciences of the Czech Republic, 1973: Czech Regional Seismic Network. International Federation of Digital Seismograph Networks, Other/Seismic Network, doi: 10.7914/SN/CZ.

Institute of Physics of the Earth Masaryk University (Czech), 2014: IPE_EDU. International Federation of Digital Seismograph Networks, Other/Seismic Network, doi: 10.7914/SN/D1.

Kövesligethy Radó Seismological Observatory (Geodetic and Geophysical Institute, Research Centre for Astronomy and Earth Sciences, Hungarian Academy of Sciences (MTA CSFK GGI KRSZO)), 1992: Hungarian National Seismological Network. Deutsches GeoForschungsZentrum GFZ, Other/Seismic Network, doi: 10.14470/UH028726.

Liščák P., Petro Ľ., Papčo J., Cipciar A., Csicsay K., Kristeková M., Bednárik M., Briestenský M., Bella P., Správa slovenských jaskýň, 2017: Partial Monitoring System – Geological Factors, Subsystem 02: Tectonic and seismic activity of the territory, Geological work number 207, Report for 2016 (Čiastkový monitorovací systém – Geologické faktory, Podsystém 02: Tektonická a seizmická aktivita, číslo geologickej úlohy 207, správa za obdobie: rok 2016), State Geological Institute of Dionýz Štúr, Regional centre Košice, 36, http://dionysos.gssr.sk/cmsgf/files/Hodn_monitor_2016/02_Tektonicka_aktivita_2016.pdf (in Slovak).

Local Seismic Network of Eastern Slovakia. Faculty of Mathematics, Physics of the Earth and Informatics, Comenius University, html://www.fyzikazeme.sk/mainpage/index_en.htm.

Pajdušák P., 1997: Historical seismic instruments at the stations Hurbanovo (HRB) and Skalnaté pleso (SPC) of Slovakia. Cahiers du Centre Européen de Géodynamique et de Séismologie, **13**, 49–60.

Polish Seismological Network (PLSN), Institute of Geophysics Polish Academy of Sciences, https://www.igf.edu.pl/stacje-en.php.

Stammler K., 1993: Seismichandler—Programmable multichannel data handler for interactive and automatic processing of seismological analyses. Computers & Geosciences, **19**, 2, 135–140, doi: 10.1016/0098-3004(93)90110-Q.

Weber B., Becker J., Hanka W., Heinloo A., Hoffmann M., Kraft T., Pahlke D., Reinhardt J., Thoms H., 2007: SeisComp3 – automatic and interactive real time data processing. Geophysical Research Abstracts In EGU General Assembly, **9**, 09129.

ZAMG – Zentralanstalt für Meterologie und Geodynamik, 1987: Austrian Seismic Network. International Federation of Digital Seismograph Networks, Other/Seismic Network, doi: 10.7914/SN/OE.

sciendo

Contributions to Geophysics and Geodesy Vol. 49/1, 2019 (11–23)

Surface temperature of plant tissues. Which method of air temperature measurement fits best?

Tomáš LITSCHMANN[1], Tomáš STŘEDA[2,3]

[1] AMET,
Žižkovská 1230, 691 02, Velké Bílovice, Czech Republic,
e-mail: amet@email.cz

[2] Department of Crop Science, Breeding and Plant Medicine, Mendel University in Brno,
Zemědělská 1665/1, 613 00 Brno, Czech Republic,
e-mail: streda@mendelu.cz

[3] Department of Meteorology and Climatology, Czech Hydrometeorological Institute,
Brno Branch, Kroftova 43, 616 67 Brno, Czech Republic

Abstract: Climate change is contributing to an increased risk of flower damage by late spring frosts. Monitoring flower temperature is critical for the timely start of frost protection systems. However, there are many weak points that complicate the use of this method. The aims of this study were to: i) find the method of air temperature measurement with the best relationship to the surface temperature of plant tissues and ii) quantify the differences between plant tissues surface temperature and ambient temperature during different weather situations. The surface temperature of plant tissues (budding leaves of grapevine, apricot flower, and unripe pear fruit), air temperature and humidity in the radiation shield, wet bulb temperature and air temperature with an unsheltered thermometer were measured at ten-minute intervals in the spring months. The average temperatures obtained by the individual methods as well as the lowest temperatures were determined from each measurement. Differences between air temperatures and plant surface temperatures, including variation ranges, were also determined. An unsheltered thermometer, in which the energy balance corresponds approximately to that of the evaluated plant surfaces, provided the best relationship with plant tissue temperature. The air temperature measured by the standard method (in a Stevenson screen or in the radiation shield) was almost always higher than the temperature of the plant tissue during periods of negative energy balance. The difference between the minimum temperatures was approximately 0.5 °C. Temperatures more than 1.5 °C higher than the actual temperature of plant tissues were measured in extreme cases.

Key words: flower temperature, leaf temperature, agricultural meteorology, cold damage, frost damage, microclimate

doi: 10.2478/congeo-2019-0002

1. Introduction

Increased interest in the issue of spring frosts is caused by the bioclimatic impacts of climate change in recent decades. Current regional studies on Central Europe state that an earlier onset of the phenological phase or the "beginning of apricot flowering" occurred for approximately 13 days in the period 1940–2008, i.e., 2 days per decade (*Chuchma et al., 2016*). A similar result has been documented for an evaluation of long-term phenological data series of wild-growing plants (*Stehnová et al., 2017; Stehnová et al., 2018*). Earlier flowering increases the risk of frost damage to flowers by late spring frosts.

There are numerous methods of microclimate modification and for mitigating cold damage to horticultural crops. These include stack heaters, wind machines, helicopters, fog generators, covers, and various irrigation methods such as flooding (*Morrow and Martsolf, 2004*). However, the timing of the implementation of these methods depends on the precise determination and prediction of risk conditions.

It is often assumed that the temperature of plant tissues corresponds to the air temperature measured by the standard method. In one of the first complex works to evaluate the difference between carnation flower temperature and air temperature, *Hanan (1965)* described that the radiation, air velocity and air temperature effects were not as high as expected. This was confirmed by *Hanan (1970)* in follow-up research. Under certain conditions of wind velocity, solar radiation and air temperature, differentials between red carnation flower temperature and air temperature exceeded 10 °C, whereas white flowers were close to the ambient air temperature.

Some complications in predicting flower temperature are as follows:

i) The air temperature is monitored, while it is truly the plant temperature that is usually predicted from two meteorological parameters: the air temperature and an estimate of the radiational cooling (*Morrow and Martsolf, 2004*). Meteorological data differing from the actual conditions of canopy microclimate are often used for this purpose. Compared to the canopy microclimate, the conditions at a standard climatological station are characterized by a reduction of temperature extremes, a wetter environment with lower variability, precipitation interception, reduced air speed, occurrence of diffuse solar radiation, etc. (*Středa et al., 2011*).

ii) Flower colour can significantly influence flower interior temperature due to differences in how the pigments absorb and reflect different wavelengths of light (*Seymour et al., 2009; Mu et al., 2010*). *Mu et al. (2010)* have determined the effect of petal colour on the interior temperature of *Gentiana leucomelaena* flowers, which have two colours (blue and white). Relative to the ambient temperature, the flower temperature was 1.27 °C higher in the white flowers but was 0.41 °C lower in the blue flowers. The ambient temperature was closely correlated with the flower frequency, i.e., white flowers were more likely to be associated with low temperature than blue flowers. *Savvides et al. (2017)* described differences of several degrees Celsius (–4.1 to 3.8 °C) between the apical meristem temperature and air temperature in cucumber and tomato plants when the air temperature was kept at ∼20 °C as a function of other environmental factors that influence the heat budget of the apical meristem such as radiation, air humidity, wind speed, and plant traits. *Shrestha et al. (2018)* found that the relationship between flower temperature and ambient temperature was non-significant for 4 samples, non-linear for 11 samples, linear for 3 samples and positive linear for 13 samples (30 plant species with 31 samples), and they found no significant correlation between temperature modulation type group and/or either colour or shape in our sample species.

iii) One of the more unusual tactics for promoting cross-pollination occurs in flowers that raise their temperatures by producing their own heat (*Seymour and Schultze-Motel, 1997*). The flowers of some plants produce enough heat to raise their temperatures by as much as tens of degrees Celsius above air temperature (by increasing heat production to approximately 1000 mW). The greatest heat producer, *Arum maculatum*, generates 0.4 watts per gram in its florets. A 125-gram spadix of *Philodendron selloum* produces about nine watts of heat to maintain a temperature of 40 °C in a 10 °C ambient environment (*Seymour, 1997*). In montane forests on sunny days with very low wind speeds, meristem (not flower) temperatures can be 15 °C higher than the air temperature (*Wilson et al., 1987*). Analogously, a study by *Little et al. (2016)* found that some sub-Antarctic herbs exhibited leaf and floral temperatures that were higher than the ambient temperature (leaves and inflorescences were 9 °C and 11 °C higher than the ambient temper-

ature respectively).

iv) The insufficiently explored "critical temperatures" for predicting flower damage on fruit trees are another problem. As a rule, it is not clear how these temperatures were obtained. The deficiency of this concept is the fact that different types of cooling have not been taken into account (*Dětinský and Havlík, 1990*).

The main question addressed by this paper is which temperature measurement methodology is best for predicting and mitigating damage to crops by frost. The ideal method should be applicable for a wide range of weather situations. It should also be as close as possible to the temperature of the threatened plant tissues.

2. Materials and methods

The measurements were carried out during a period from the 10^{th} of April 2018 to the 9^{th} of May 2018 (Table 1) in the experimental area of Moravský Žižkov (South Moravia, Czech Republic), which has a long-term average annual air temperature of 9.2 °C, an average annual precipitation of 482 mm, and a long-term average monthly temperature of 9.7 °C in April and of 14.5 °C in May. The surface temperature of the plant tissues (surface thermometer), the air temperature and air humidity in a radiation shield (sheltered thermometer and humidity meter), the wet bulb temperature with an unsheltered thermometer (thermometer covered with a wet cloth; wet temperature), and the air temperature with an unsheltered thermometer were measured at ten-minute intervals. The sensors were located at the same height in the immediate vicinity of the crop. The air temperature in the radiation shield at a standard height of 2 m and the wind speed at a height

Table 1. Overview of measurement dates for individual plant surfaces.

Plant species	**Measured surface**	**Beginning of measurement**	**End of measurement**
apricot	flower	10^{th} April 2018	16^{th} April 2018
pear	flower	16^{th} April 2018	22^{nd} April 2018
grapevine	leaves	22^{nd} April 2018	1^{st} May 2018
pear	green fruit	1^{st}May 2018	9^{th} May 2018

of 6 m above the terrain were measured at a distance of several metres. The air temperature was measured with a DS18B20 sensor (Maxim Integrated, San Jose, California, USA). Air humidity was measured with a HIH-4000 sensor (Honeywell, Golden Valley, Minnesota, USA).

An infrared temperature sensor, the Omega OS211-LT, connected to a MeteoUNI data logger (AMET, Velké Bílovice, Czech Republic), was used to measure the surface temperatures of the plant tissues – Fig. 1.

The period from sunset to sunrise, when plants and unsheltered thermometers were not affected by shortwave radiation, was evaluated. Air temperature measurement in the radiation shield was chosen as the standard method of determining the air temperature. According to *Snyder and de Melo-Abreuet (2005)*, it is advisable to use a wet bulb thermometer in situations preceded by a rainy season or intense dew. The length of time that the plant tissues are covered with dew varies overnight, but the wet bulb thermometer loses heat by evaporation permanently. Consequently, a variant with an unsheltered thermometer placed close to the measured surface was also realized. In the case of rain or dew, the presence of liquid water on its surface is similar to that of the examined tissues.

Fig. 1. Measurement of the surface temperature of plant tissues with an infrared sensor.

3. Results and discussion

The courses of air temperature, air humidity and the surface temperature of the budding leaf during representative weather conditions are shown in Figs. 2 and 3. Cases with low wind speeds not exceeding 0.5 $\mathrm{m\,s^{-1}}$ and

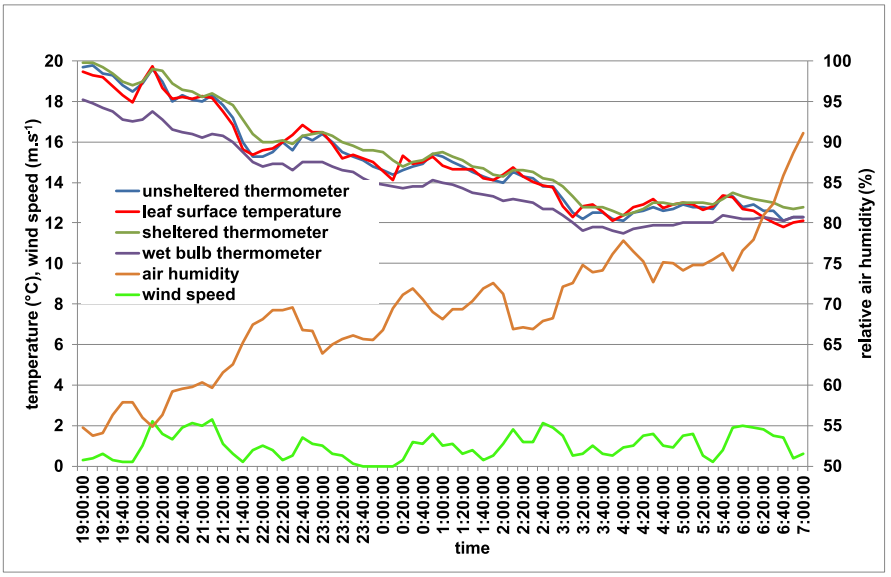

Fig. 2. The courses of air temperatures and the surface temperature of the budding leaves of grapevine on the 25–26th of April 2018 (no wind, low air humidity).

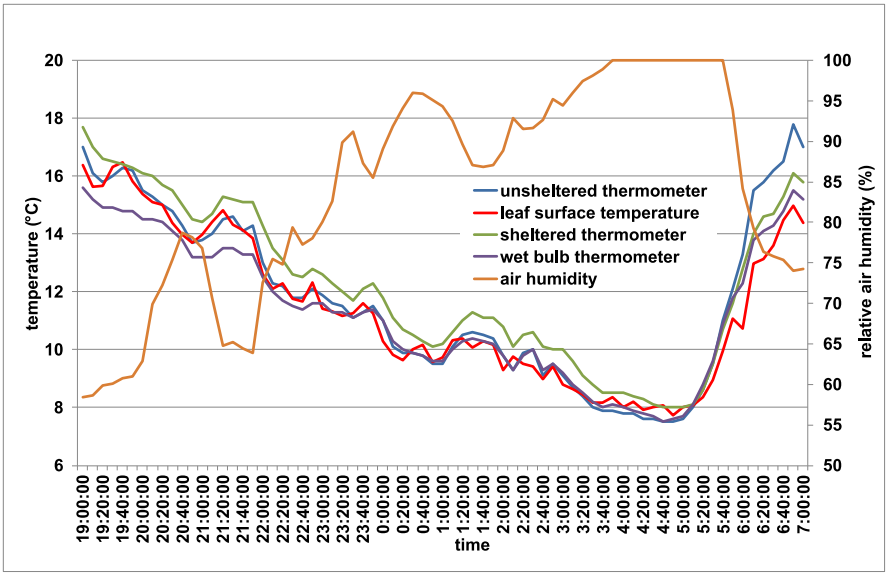

Fig. 3. The courses of air temperatures and the surface temperature of the budding leaves of grapevine on the 24–25th of April 2018 (no wind, low air humidity).

with varying relative air humidity have been selected. In the first case, the air humidity during the night ranged from 60–75% and only began to rise rapidly close to the morning. Therefore, the wet temperature was below the leaf surface temperature for most of this time and approached it when the humidity increased. Although the wet thermometer showed a lower value almost all night, the values were most similar when the stand temperature was low. On the other hand, the air temperature measured by the sheltered thermometer was almost always higher than the temperature of the stand and higher even when the stand temperature was at its minimum. Relatively good congruence between the unsheltered thermometer and the temperature of the crop was shown during the whole monitoring period.

The period of higher relative humidity was considerably longer in the second case. After air humidity rose above 85%, all three curves (leaf temperature, wet temperature, and the temperature measured with an unsheltered thermometer) almost coincide (even when the minimum is reached). The fastest temperature increase was measured with the unsheltered thermometer after sunshine was recorded; the increase in the surface temperature of the budding leaves was lowest.

It is obvious that a good relationship can be expected between the surface temperature of plant tissues and the temperature measured with the unsheltered thermometer. For the wet thermometer, the magnitude of deviation depends on the air humidity or the occurrence of precipitation (Fig. 4). The difference between the temperature of the wet thermometer and the flower temperature was greater than 2 °C before rain. The unsheltered thermometer showed a very good relationship with the flower temperature before the rain. Its values came close to those of the wet thermometer due to moistening by the rain. The air temperature measured in the shield indicated higher values than the actual flower temperature.

Fig. 5 shows the significantly different meteorological situation that occurred the following night. The radiation character of night weather and windlessness contributed to a sharp drop in air temperatures and the surface temperatures of apricot flowers. The surface temperature of flowers during this type of weather fell to its lowest value. A similar state can be expected even when temperatures drop to or below 0 °C, i.e., to a level with a risk of flower damage from frost. This course confirms the effect of the cooling character on the reaction of thermometers of various constructions. This

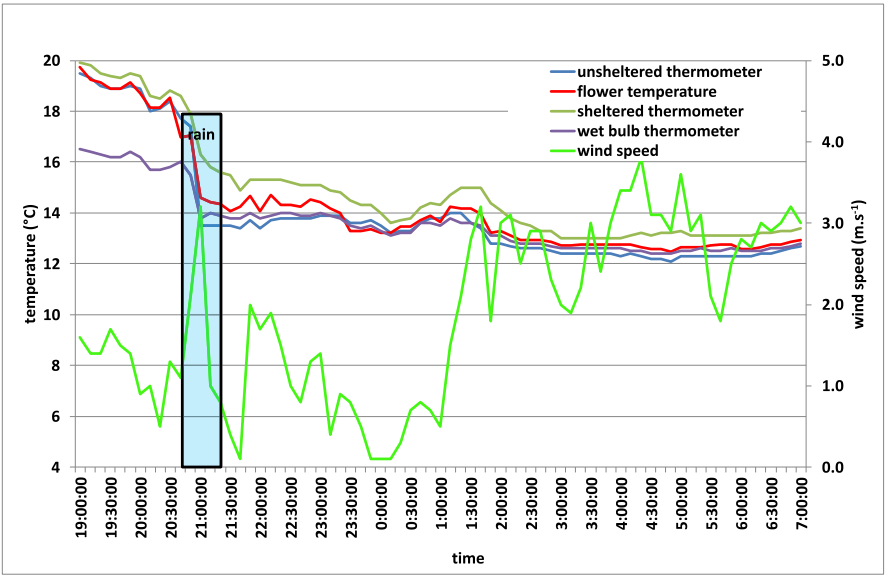

Fig. 4. The courses of air temperature and the surface temperature of the apricot flowers on the 12–13th of April 2018.

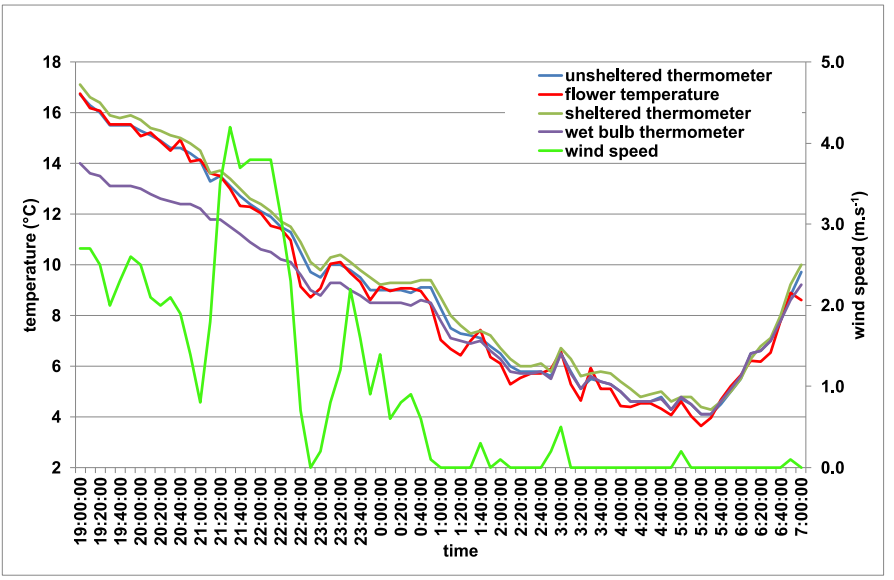

Fig. 5. The courses of air temperatures and the surface temperature of the apricot flowers on the 13–14th of April 2018.

fact has a significant influence on the success of agro-meteorological models for the prediction of frost on vegetation.

A statistical evaluation of the deviations between the measured minimum air temperatures and the surface temperature is presented in Figs. 6 to 9.

In terms of minimum temperatures, the smallest differences were found using a wet thermometer or unsheltered thermometer. The maximum deviation for the budding vine leaf was –0.74 °C, in the other investigated/examined cases it reached lower values. The highest deviations were detected between the surface temperature of the plant tissues and the air temperature measured in the radiation shelter in close proximity to the given surface as well as at a nearby meteorological station at a height of 2 m. These temperatures were higher by 0.4–0.8 °C on average. The highest deviations were observed in the budding leaves of the grapevine, where they reached 1.5 °C. *Dětinský and Havlík (1990)* state that there is a temperature difference of 0.3 °C between the cherry blossom surface and the temperature measured in the Stevenson screen at a height of 2 m during advection at night time; this difference increased to 0.9–1.3 °C in the case of cherry leaves during the radiation fog, where the vegetation surface is always cooler.

Based on the average deviations determined from all three night measurements (Fig. 9) the best relationship was observed for the unsheltered thermometer, while the wet thermometer usually showed a lower temperature and the sheltered thermometer measured a higher temperature.

The temperature of a plant organ is generally very close to air temperature except in a few specific cases, for example when radiation and vapor pressure deficit are low (*Savvides et al., 2013*). On the basis of energy balance, unshaded plant parts have a different balance of longwave radiation and eventually latent heat at night. During clear nights, the surface temperature of objects close to the Earth's surface is lower than the ambient air temperature due to longwave radiation (*Curtis, 1936*). Flowers have few or no stomata and therefore do not exhibit transpirational cooling. At night, when the radiant energy balance is negative, the buds or flowers may be expected to be colder than the atmosphere, and warmer than the air when the sun is shining during the light part of the day (*Grace, 2006*). They may be similar to the surface temperature of non-living parts of plants (*Středa et al., 2015*) and significantly different in comparison to the surface temperature of green plant parts.

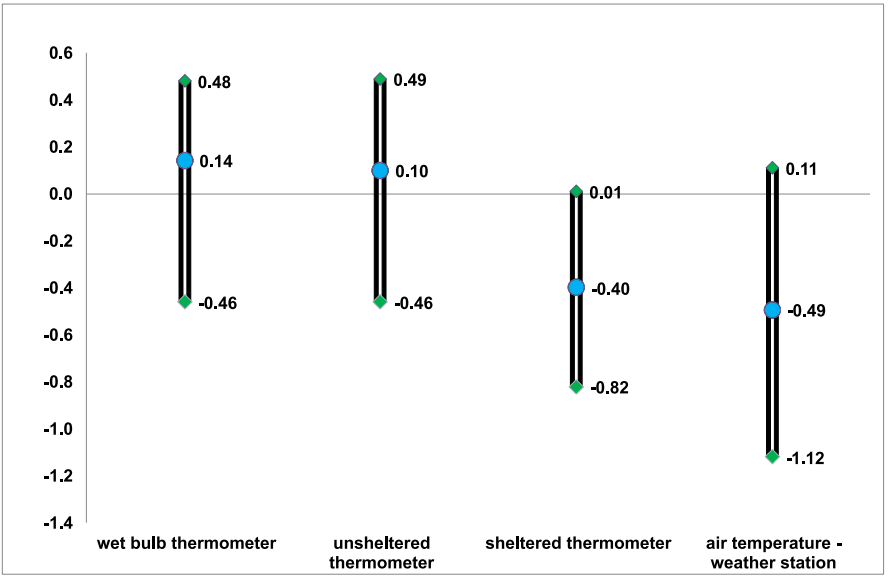

Fig. 6. Average and range of variation between the minimum flower temperatures and the minimum air temperatures.

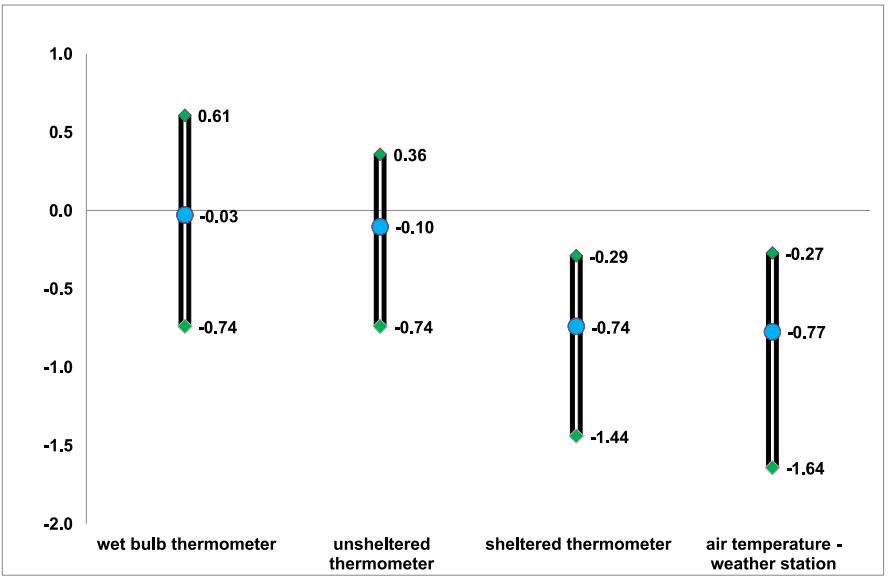

Fig. 7. Average and range of variation between the minimum budding grapevine leaf temperatures and the minimum air temperatures.

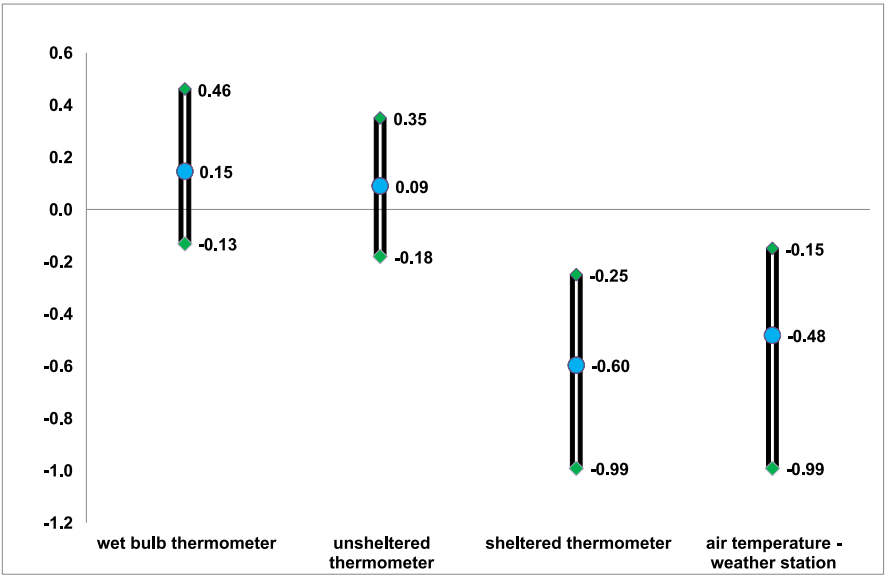

Fig. 8. Average and range of variation between the minimum temperatures of pear fruit and the minimum air temperatures.

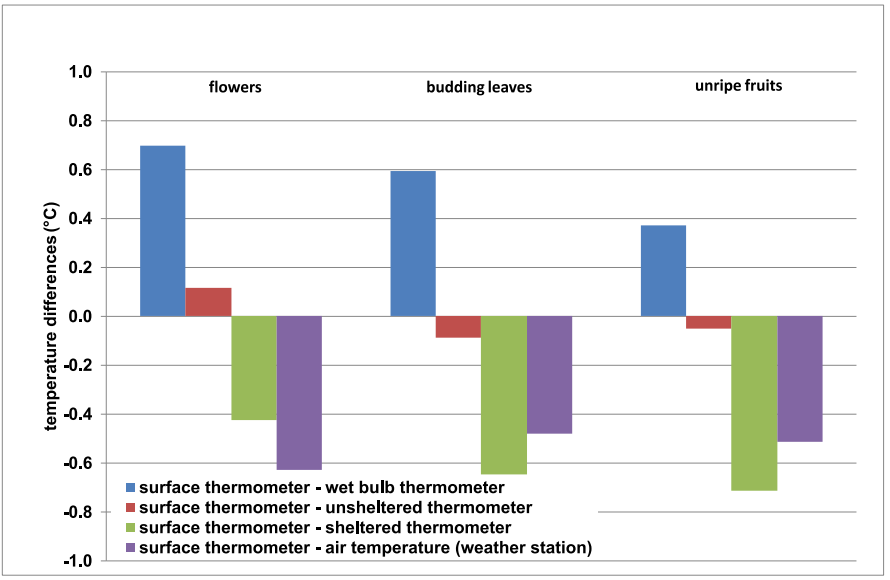

Fig. 9. Average differences between the air temperatures monitored by different methods and the surface temperatures of various plant tissues.

4. Conslusion

The air temperature measured in the standard way (in the Stevenson screen or in the radiation shield) is almost always higher than the temperature of the plant tissue during periods of negative energy balance. A sheltered thermometer always shows higher temperatures throughout the whole night. A wet bulb thermometer only has a good relationship with the temperature of plant tissues during minimum temperatures. This is mainly because the highest relative air humidity is reached at the moment minimum air temperature is reached. A wet thermometer, depending on the relative air humidity, can show a temperature that is even several degrees lower at night. If it were used to control frost protection, it would run prematurely. An unsheltered thermometer, in which the energy balance corresponds approximately to that of the evaluated plant tissues, provides the best relationship with the temperature of the plant tissues.

Acknowledgements. This research was financially supported by projects of the National Agency of Agricultural Research Ministry of Agriculture No. QJ1530181.

References

Chuchma F., Středová H., Středa T., 2016: Bioindication of climate development on the basis of long-term phenological observation. In MendelNet 2016: Proceedings of International PhD Students Conference. Brno: Mendel University in Brno, 380–383.

Curtis O. F., 1936: Leaf temperatures and the cooling of leaves by radiation. Plant Physiology, **11**, 2, 343–364, doi: 10.1104/pp.11.2.343.

Dětinský F., Havlík V., 1990: Orchards frost protection with artificial fog (Protimrazová ochrana ovocných sadů umělou mlhou). Práce a studie č. 17, ČHMÚ, 53 p. (in Czech).

Grace J., 2006: The temperature of buds may be higher than you thought. New Phytologist, **170**, 1, 1–3, doi: 10.1111/j.1469-8137.2006.01675.x.

Hanan J. J., 1965: Preliminary measurements of flower temperature. Flower Grower's Association Bulletin, **188**, 1–4.

Hanan J. J., 1970: Statistical analysis of flower temperatures in the carnation. Journal of the American Society of Horticultural Science, **95**, 68–73.

Little L., Eidesen P. B., Müller E., Dickinson K. J. M., Lord J. M., 2016: Leaf and floral heating in cold climates: do sub-Antarctic megaherbs resemble tropical alpine giants? Polar Research, **35**, 1–11, doi: 10.3402/polar.v35.26030.

Morrow C. T., Martsolf J. D., 2004: Mitigating Cold Damage in Horticultural Crops. Crop, Environment and Bioinformatics, **1**, 272–296.

Mu J., Li G., Sun S., 2010: Petal Color, Flower Temperature, and Behavior in an Alpine Annual Herb, *Gentiana leucomelaena* (*Gentianaceae*). Arctic, Antarctic, and Alpine Research, **42**, 2, 219–226, doi: 10.1657/1938-4246-42.2.219.

Savvides A., van Leperen W., Dieleman J. A., Marcelis L. F. M., 2017: Leaf initiation rate is determined by more than just air temperature: considerations for greenhouse climate control and crop modeling. Acta Horticulturae, **1170**, 417–424, doi: 10.17660/ActaHortic.2017.1170.51.

Savvides A., van Leperen W., Dieleman J. A., Marcelis L. F. M., 2013: Meristem temperature substantially deviates from air temperature even in moderate environments: is the magnitude of this deviation species-specific? Plant Cell and Environment, **36**, 11, 1950–1960, doi: 10.1111/pce.12101.

Seymour R. S., 1997: Plants that warm themselves. Scientific American, **276**, 3, 104–109.

Seymour R. S., Maass E., Bolin J. F., 2009: Floral thermogenesis of three species of *Hydnora* (*Hydnoraceae*) in Africa. Annals of Botany, **104**,5, 823–832, doi: 10.1093/aob/mcp168.

Seymour R. S., Schultze-Motel P., 1997: Heat-producing flowers. Endeavour, **21**, 3, 125–129, doi: 10.1016/S0160-9327(97)80222-0.

Shrestha M., Garcia J. E., Bukovac Z., Dorin A., Dyer A. G., 2018: Pollination in a new climate: Assessing the potential influence of flower temperature variation on insect pollinator behaviour. PLOS ONE, **13**, 8, e0200549, doi: 10.1371/journal.pone.0200549.

Snyder R. L., de Melo-Abreu J. P., 2005: Frost protection: fundamentals, practice and economics, Volume 1. Food and Agriculture Organization of the United Nations, Rome, http://www.fao.org/3/a-y7223e.pdf.

Stehnová E., Středová H., Rožnovský J., Středa T., 2017: Phenological observations and their possible use within the monitoring allergens. In: Public recreation and landscape protection – with nature hand in hand. Brno: Mendel University in Brno, 241–248.

Stehnová E., Středová H., Středa T., 2018: Determination of the time of occurrence of selected allergens with using long-term phenological series. In Public recreation and landscape protection – with nature hand in hand! Brno: Mendel University in Brno, 103–108.

Středa T., Litschmann T., Středová H., 2015: Relationship between tree bark surface temperature and selected meteorological elements. Contributions to Geophysics and Geodesy, **45**, 4, 299–311, doi: 10.1515/congeo-2015-0026.

Středa T., Středová H., Rožnovský J., 2011: Orchards microclimatic specifics. In Bioclimate: Source and Limit of Social Development. Nitra: Slovak Agricultural University, 132–133.

Wilson C., Grace J., Allen S., Slack F., 1987: Temperature and stature: a study of temperatures in montane vegetation. Functional Ecology, **1**, 4, 405–413.

sciendo

Contributions to Geophysics and Geodesy Vol. 49/1, 2019 (25–36)

Smart method of agricultural drought regionalization: A winter wheat case study

Tomáš STŘEDA[1,2], Hana STŘEDOVÁ[1,2], Filip CHUCHMA[1,2], Josef KUČERA[3], Jaroslav ROŽNOVSKÝ[2]

[1] Faculty of AgriSciences, Mendel University in Brno, Zemědělská 1665/1, 613 00 Brno, Czech Republic, e-mail: streda@mendelu.cz

[2] Department of Meteorology and Climatology, Czech Hydrometeorological Institute, Brno Branch, Kroftova 43, 616 67 Brno, Czech Republic

[3] Department of Land Consolidation, Research Institute for Soil and Water Conservation, Brno Branch, Lidická 25/27, 602 00 Brno, Czech Republic

Abstract: The occurrence of drought during flowering (usually from the end of May to the beginning of June) is the most hazardous timing in terms of the possible negative impact of agricultural drought on winter wheat, which is the most cultivated crop in the Czech Republic (about 800000 ha). Lack of water, often accompanied by high temperatures, negatively affects the number of grains in the wheat ear and the tissue development of the developing grain, with consequent impacts on yield and quality of product. With the use of a) long-term time series of agrometeorological data (1961–2010), b) long-term phenological time series of winter wheat (1981–2010), and c) soil conditions data (available water capacity of soils of the Czech Republic) for the arable soil, the ratio of actual evapotranspiration and potential evapotranspiration for the period of 1961–2010, used as an indicator of agricultural drought (lack of water) for wheat, was calculated. The innovative aspect of this categorization of the territory of the Czech Republic according to the risk of occurrence of agricultural drought for winter wheat is considering drought from the aspect of the plant, i.e., evaluation based on the actual consumption of water by the vegetation. This is a very sophisticated procedure. Frequently, water content in soils data, presented as an output of some models, do not fully indicate the possible negative impacts on yield generation because the plants themselves are typically not considered. The method used in this study is universally applicable and allows comparisons of regions at the local, regional, and supra-regional levels. For estimation of the development of agronomic drought in the future, the basic water balances in the growing seasons of 1961–2010 and 2071–2100 were compared using a climate scenario. The forecast indicates a significant deterioration of agricultural drought in the region with probable direct impacts on agricultural production.

Key words: evapotranspiration, soil moisture, phenology, wheat, ALADIN, agroclimatology

doi: 10.2478/congeo-2019-0003

1. Introduction

Precipitation in the Czech Republic is characterized by considerable spatial and temporal variability. In addition to certain types of synoptic situations, this variability is also due to orographic influences, such as increase of precipitation with increasing altitude and slope exposure. Additionally, the quantity and distribution of precipitation in central Europe are expected to change in the future (*Škvarenina et al., 2009; Nikolova et al., 2016*). Climate models predict moderate growth of rainfall by the year 2050, on average, for the whole of the Czech Republic. Compared with the long-term average of 1961–2000, precipitation should increase in Moravia compared to Bohemia, as suggested by the ALADIN model. Furthermore, this model assumes a 15% reduction in precipitation in winter, an increase in rainfall of up to 20% in the autumn period, and a 10% increase in the summer period. A slight decrease in rainfall totals is expected by 2100 according to the outlook. From the point of view of distribution of rainfall over the course of the year, *Středová et al. (2011)* and *Středová and Středa (2015)* suggested that there might be an increase in the number of days without precipitation from the current 79.9 days to 141.6 days between 2071 and 2100. A simultaneous increase in the mean sum of effective temperatures above 10 °C from the current 2717 °C to 3732 °C is also predicted. These changes will increase the evapotranspiration requirements of the environment where stands will be exposed. Despite the fact that drought is a relatively recent problem in central Europe (*Klimešová et al., 2017; Procházková et al., 2016*), it is seen as a long-term serious abiotic stress affecting yields of agricultural crops throughout the world (*Boyer, 1982*).

The easiest way to define dry areas in the Czech Republic seems to be through the course of the 500 mm isohyet of average annual precipitation. Calculations of scenario values of potential evapotranspiration predict a significant increase in drought risk in the Czech Republic. As a result of estimation of meteorological and hydrological indexes, central and southern Moravia, central and northwestern Bohemia, and lower and central Polabí and Povltaví will be more vulnerable to drought (*Kalvová et al., 2002*). *Kohut et al. (2009)* carried out a detailed analysis of the development of water conditions in the Czech Republic for the period of 1961–2000. The results of the analysis showed that soil moisture is already decreasing at present.

The limiting value for C3 cereals (e.g., wheat, barley, oat, rye), where there is no reduction in transpiration, is a soil moisture in the root zone value of about 50–65% of the available water capacity. However, long-term values lower than 45% of usable water capacity are characteristic of the intensely utilized agricultural areas of the Czech Republic up to about 300 m above sea level.

Blum (2005) defines the onset of drought as a period when the plant water demand is not satisfied and plant water deficit occurs. *Lipiec et al. (2013)* define drought as the result of water flow imbalance between the evapotranspiration demands of the environment and the transport of water in the soil-root system. Generally, plant stress caused by drought can be determined by measuring the water potential of leaves (*Jones, 2007*). Values of –0.5 MPa indicate slight stress caused by drought resulting in significant slowing of growth. To the contrary, values of around –1.5 MPa indicate very strong stress caused by drought, with loss of cell turgescence and wilt.

Drought causes reduction of the number of founding grains during generative phases (*Lawlor et al., 1981*), and the flowering stage of development is the critical period during which water shortages have the greatest impact. The properties of a plant's root system may increase the plant's ability to receive water. Hence, the root system has received great interest as the organ responsible for the tolerance to drought of some crop varieties (*Středa et al., 2012*).

The water consumption of cereals varies within about 300–800 $\mathrm{l\,kg^{-1}}$ of dry matter above ground according to the conditions of the environment and the period of growth. Winter cereals need at least 500–600 mm of precipitation, or 500–600 $\mathrm{l\,m^{-2}}$, for high yields and about 8 $\mathrm{t\,ha^{-1}}$ or more for the entire growing season. The availability of soil moisture, global radiation, and saturation deficit are the main determinants of transpiration (*Du et al., 2011; She et al., 2012; Zeppel et al., 2008*). The daily, as well as the long-term, course of these variables influences the transpiration flow of the plant (*Naithani et al., 2012*). In the event of drought stress, it is assumed that soil moisture will have the greatest effect on the transpiration process (*Matejka et al., 2005*). Changes in transpiration intensity are considered an indicator of drought stress on the plant. This inspired the authors to develop an internationally applicable universal method for categorization of areas according to the risk of occurrence of agricultural drought for winter wheat.

2. Material and methods

2.1. Categorization of the territory of the Czech Republic according to the risk of occurrence of agricultural drought for winter wheat

The input data for calculation of the ratio of actual evapotranspiration (aE: evapotranspiration affected by the amount of water in the soil) and potential evapotranspiration (pE: the maximum demands on the environment for evaporation and transpiration) consisted of a set of calculated daily values of aE and pE for the period of 1961–2010 with the use of a method of calculation according to Penman-Monteith's methodology (*Penman, 1948*). For the purposes of the entire calculation "Agrometeorological Computing and Information System" AVISO (*Kohut, 2007; Kohut et al., 2009*) which uses selected algorithms (modified Penman-Monteith method) and is a Czech alternative to the similar English model MORECS (The Meteorological Office Rainfall and Evaporation Calculation System) was used (*Thompson et al., 1981; Hough et al., 1997*). The model is based on the combined Penman-Monteith's equation for the calculation of evapotranspiration in a modified manner. The input meteorological data are: air temperature and air humidity in the form of water vapor, sunshine duration, wind speed and precipitation. To analyze the actual evapotranspiration (aE) were performed for winter wheat with the using of AVISO model and methodology *Allen et al. (1998)*.

The data were calculated from an input of calculated series of meteorological variables (*Skalák et al., 2008*) of the points of a regular 10×10 km grid network (789 points within the Czech Republic). The aE and pE values for winter wheat were calculated on the basis of the phenological and biological specifics of the species, and the specific hydrolimit was derived for each calculation grid point from the available water capacity layer. The average date of the beginning of flowering was determined from the phenological layer of the beginning of the flowering of winter wheat (1981–2010 i.e. the longest available homogeneous area-wide data series; database of the Czech Hydrometeorological Institute) for each grid point, and the calculation period was set to within 10 days before and 10 days after that date. Long-term (1961–2010) aE and pE were calculated for each grid point of the specified period. These values were subsequently used to determine the ratio sum aE/sum pE, and the resulting set of grid points with the assigned

aE/pE ratios for the period of 1961–2010 was created. A GIS dot layer was subsequently created from these data.

The values for the individual points were interpolated using the local linear regression method with an altitude dependence with the estimated value correction to maintain a value corresponding to the location of the station (ClidataDEM method used in the CLIDATA database of the Czech Hydrometeorological Institute). The resulting raster model was then processed in the ArcGIS 10.3 software environment and subsequently blotted out by the nearest neighbor method. Raster layers were then reclassified into individual categories with a step of 0.04 and converted to polygons. Only areas classified as arable land were selected from the resulting polygon layer. The resulting map output was created in the GIS environment.

2.2. Potential water balance in the growing season

The basic parts of the water balance of a given area are precipitation and evapotranspiration, which along with drainage forms the loss component. Because of the complex interactions between soil, vegetation, and atmosphere, evapotranspiration is very difficult to quantify. The total amount of evaporated water depends primarily on the meteorological conditions prevailing at the site. The determining factors are, above all, intensity of sunshine, albedo and surface roughness, wind speed, air temperature, and air humidity. Because this is a large number of factors, reference is made to actual (or potential) evapotranspiration for each crop calculated by the Penman-Monteith equation in the AVISO model (*Kohut et al., 2009*).

In order to capture the future climate trend, scenario data were created at the Czech Hydrometeorological Institute. The scenario data were created by integration of the regional climate model ALADIN-Climate/CZ within the CECILIA international project. As part of this project, climatic conditions for Central Europe were simulated using ALADIN-Climate/CZ with a resolution of 10 km. The simulation was carried out with using the A1B emission scenario (according to IPPC). Based on simulations of the ALADIN-10 model, the water balance (difference of precipitation and actual evapotranspiration) in the growing season (i.e. April to September) for the periods of 1961–2010 and 2071–2100 was calculated for the Czech Republic (details in *Chuchma et al., 2017*).

3. Results and discussion

3.1. Categorization of the territory of the Czech Republic according to risk of occurrence of agricultural drought for winter wheat

The aim of the analysis and mapping of the outcomes was to define areas with increased risk of agricultural drought occurrence during the critical growth and development phase of winter wheat vegetation (flowering) in the territory of the Czech Republic based on a sophisticated synthesis of a) long-term time series of agrometeorological data, b) long-term phenological time series of winter wheat, and c) soil conditions data (available water capacity of Czech soils) for the arable land category (Fig. 1). The risk of occurrence of agricultural drought for winter wheat according to drought indicator aE/pE on the territory of the Czech Republic was categorized to six the same range intervals. Since in this case we deal with a relative risk

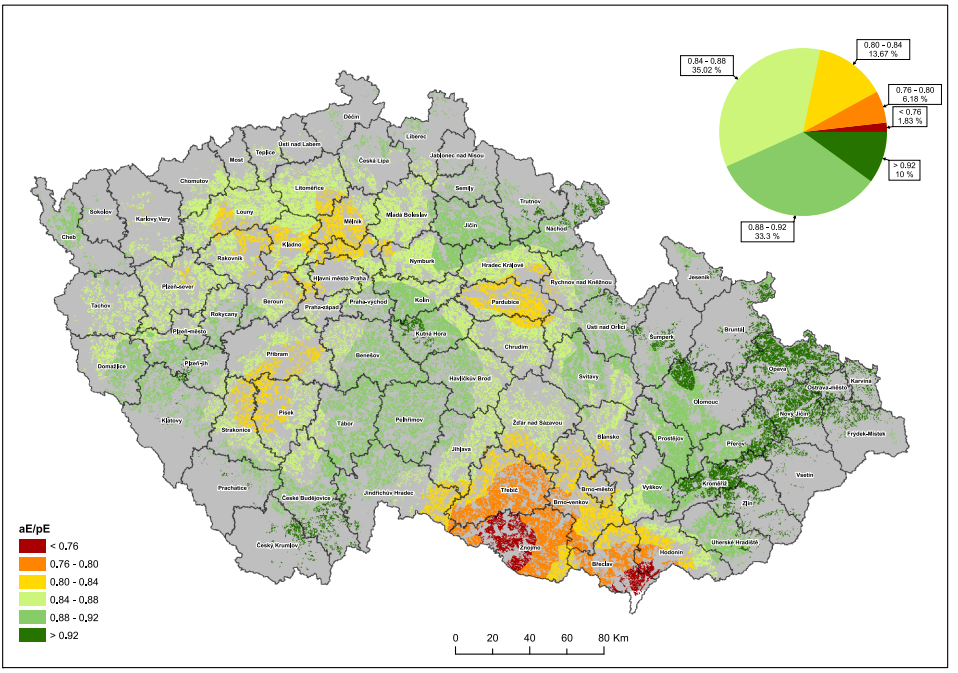

Fig. 1. Categorization of the territory of the Czech Republic using aE/pE according to the risk of occurrence of agricultural drought for winter wheat (1961–2010).

quantification, these categories do not correspond to climatological or hydrologic drought categories.

In accordance with the research priorities of the Ministry of Agriculture for the period 2017–2025, the map provides partial information for optimization of crop representation in each locality, organization and optimization of farming techniques, use of minimization and soil conservation technologies for better soil retention, utilization of varieties tolerant to drought, and the potential for using an effective irrigation system at the time when plants most need water.

It should be possible to refine the application of countermeasures leading to soil protection, especially against wind erosion and nutrient loss, thus ensuring all of their functions and sustainable arable farming. The developed method (map) will, among other uses, be applicable to legislative and non-legislative documents of the Ministry of Agriculture intending to mitigate the impacts of agricultural activities on natural resources, including land. The documents are useful for the verification of previous outputs with possible application in the Ministry of Agriculture.

3.2. Potential water balance in the growing season

Rožnovský et al. (2015) used for the calculated long-term values of water balance from grassland (mm) during vegetation period eight categories (less than –150 mm to more than 150 mm), out of which six were given by intervals of 50 mm and two tail (no danger risk of drought – exceptional risk of drought). Nevertheless, for our evaluation mere eight categories are insufficient, because water balance lower than –150 mm fits for significant part of the Czech Republic. Verbal categorization of those categories has not been set yet.

Figs. 2 and 3 show the values of potential water balance for the periods of 1961–2010 and 2071–2100, respectively. For the period of 1961–2010, the most significant interval of water balance is the interval of 0 to –50 mm (Table 1). This interval is represented broadly on 21.73% of the territory of the Czech Republic. Negative values of water balance show areas where potential evapotranspiration prevails over rainfall. A total of 71.55% of the Czech Republic is within the range of potential evapotranspiration from 0 to less than –250 mm. Water balance values in the growing season lower

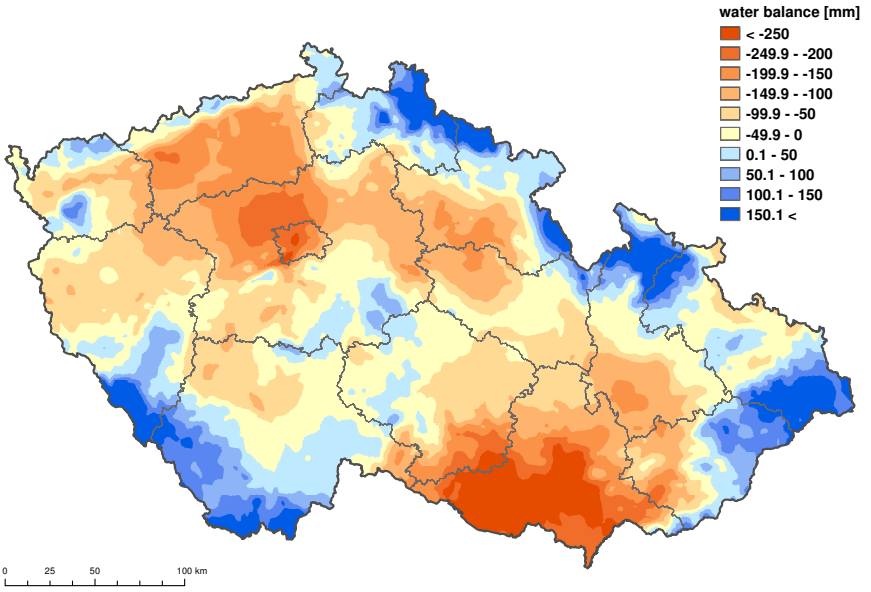

Fig. 2. Water balance in the growing season for the period of 1961–2010.

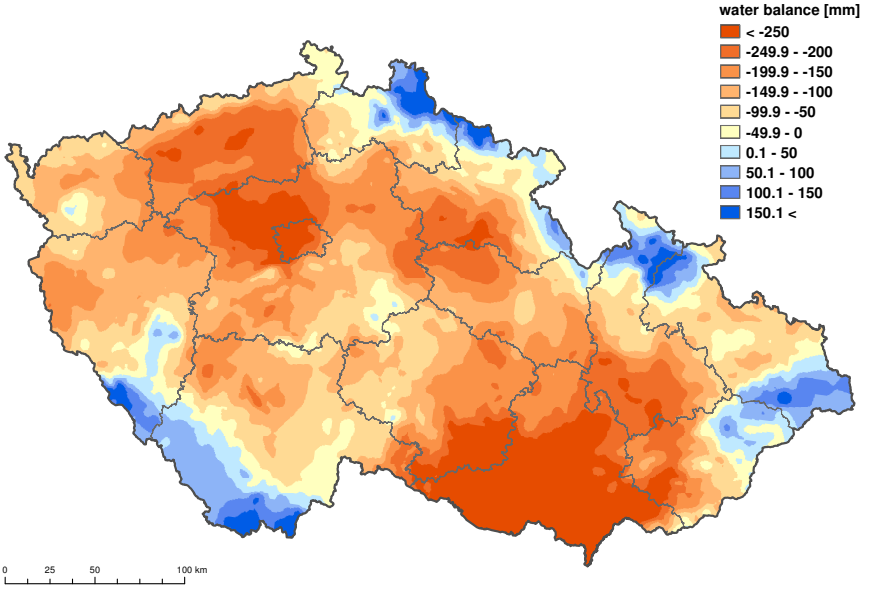

Fig. 3. Water balance in the growing season for the period of 2071–2100.

than –250 mm are typical for the most fertile parts of the Czech Republic (southern Moravia, Polabí), where the land is used mainly for agricultural purposes. Greater predominance of potential evapotranspiration over rainfall could pose a major problem in the future, especially in the context of drought threat. Additionally, in 28.43% of the territory of the Czech Republic, precipitation totals in the growing season are greater than potential evapotranspiration. These regions are mainly mountain and foothill areas. These findings should also be perceived in the context of officially set farm land prices, where the highest prices and, in theory, the most productive land correspond to sites where drought is already being monitored and is predicted to increase in the future. In the soils traditionally considered as the most fertile, water is gradually becoming a limiting factor.

Table 1. Area of individual categories of potential water balance in the growing season for 1961–2010 and 2071–2100.

1961–2010		**2071–2100**	
mm	**% of the territory**	**mm**	**% of the territory**
< -250	3.66	< -250	10.99
$-250 - -200$	3.68	$-250 - -200$	12.37
$-200 - -150$	8.59	$-200 - -150$	17.34
$-150 - -100$	14.15	$-150 - -100$	19.41
$-100 - -50$	19.74	$-100 - -50$	18.60
$-50 - 0$	21.73	$-50 - 0$	8.50
$0 - 50$	13.29	$0 - 50$	4.59
$50 - 100$	5.69	$50 - 100$	4.39
$100 - 150$	4.25	$100 - 150$	2.33
$150 <$	5.20	$150 <$	1.48

A map layer of water balance during the growing season of 2071–2100 was created on the basis of emission scenario A1B (Intergovernmental Panel on Climate Change [IPCC]). Based on the analysis, in the future, potential evapotranspiration will prevail over precipitation in most of the territory of the Czech Republic, specifically 87.21% of the territory. According to estimates, this means a 15.66% increase compared to the period of 1961–2010. In the period of 2071–2100, the largest part of the Czech Republic (18.60%) will fall within the water balance range –100 to –50 mm. Consequently, a significant extension of sites with potential evapotranspiration predominant over precipitation is expected. In the future, a predominance

of precipitation over potential evapotranspiration during the growing season is expected only in mountainous areas. Between 2071 and 2100, there will be a pronounced decline in water balance values at all altitudes compared to the reference period of 1961–2000. More frequent occurrence and higher intensity of drought can therefore be expected.

4. Summary

The innovative aspect of the method of categorization of the territory of the Czech Republic according to the risk of occurrence of agricultural drought for winter wheat is considering drought occurrence from the aspect of the plant, i.e., evaluation based on the actual need of water by the vegetation.

The resulting maps also define areas as at risk that appear to be less risky on standard maps; however, depending on actual precipitation, these areas correspond to areas of wheat agriculture affected by drought in recent years. The map therefore forms a basis for wheat cultivation targeted for relevant features and for regionalization of varieties.

The comparison of the water balance in the growing season for the periods of 1961–2010 and 1971–2100 predicts a significant deterioration of agricultural drought in the region.

Acknowledgements. This research was supported financially by the National Agency of Agricultural Research Ministry of Agriculture (project Nos. QJ1510098 and QK1720285).

References

Allen R. G., Pereira L. S., Raes D., Smith M., 1998: Crop evapotranspiration. Guidelines for computing crop water requirements. FAO Irrigation and Drainage Paper No. 56, FAO, Roma, 301 p.

Blum A., 2005: Drought resistance, water-use efficiency, and yield potential – are they compatible, dissonant, or mutually exclusive? Australian Journal of Agricultural Research, **56**, 1159–1168, doi: 10.1071/AR05069.

Boyer J. S., 1982: Plant productivity and environment. Science, **218**, 4571, 443–448, doi: 10.1126/science.218.4571.443.

Chuchma F., Středová H., Středa T., Rožnovský J., Svejkovská A., 2017: Climatic regionalization update in terms of estimated pedologic-ecological system (Aktualizace klimatických regionů v rámci systému bonitovaných půdně ekologických jednotek). Brno: Mendelova univerzita v Brně, 96 p. (in Czech).

Du S., Wang Y. L., Kume T., Zhang J. G., Otsuki K., Yamanaka N., Liu G. B., 2011: Sapflow characteristics and climatic responses in three forest species in the semiarid Loess Plateau region of China. Agricultural and Forest Meteorology, **151**, 1–10, doi: 10.1016/j.agrformet.2010.08.011.

Hough M., Palmer S., Weir A., Lee M., Barrie I., 1997: The Meteorological Office Rainfall and Evaporation Calculation System: MORECS version 2.0. Meteorological Office, Bracknell, 82 p.

Jones H. G., 2007: Monitoring plant and soil water status: established and novel methods revisited and their relevance to studies of drought tolerance. Journal of Experimental Botany, **58**, 2, 119–130, doi: 10.1093/jxb/erl118.

Kalvová J., Kašpárek L., Janouš D., Žalud Z., Kazmarová H., 2002: Specification of the climate change impact scenarios for the territory of the Czech Republic and estimation of this impact on hydrological regime, agricultural sector, forest management and human health in CR (Zpřesnění scénářů projekce klimatické změny na území České republiky a odhadů projekce klimatické změny na hydrologický režim, sektor zemědělství, sektor lesního hospodářství a na lidské zdraví v ČR). NKP: Praha, 151 p. (in Czech).

Klimešová J., Procházková P., Středa T., 2017: Significant decreasing trend of moisture conditions during the growing season in the Central Europe. Proceedings of 24th international PhD students conference (MENDELNET 2017). Mendel University in Brno, Brno, 76–80.

Kohut M., 2007: Water balance of agricultural landscape. Doctoral Dissertation, Mendel University in Brno, Brno, 128 p. (in Czech).

Kohut M., Rožnovský J., Chuchma F., 2009: The long-term soil moisture reserve variability in the Czech Republic based on the AVISO model. In: Sustainable Development and Bioclimate, Stará Lesná, Slovakia. Slovak Academy of Sciences: Bratislava, 160–161.

Lawlor D. W., Day W., Johnston A. E., Legg B. J., Parkinson K. J., 1981: Growth of spring barley under drought: crop development, photosynthesis, dry-matter accumulation and nutrient content. The Journal of Agricultural Science, **96**, 1, 167–186, doi: 10.1017/S002185960003197X.

Lipiec J., Doussan S., Nosalewicz A., Kondracka K., 2013: Effect of drought and heat stresses on plant growth and yield: a review. International Agrophysics, **27**, 4, 463–477, doi: 10.2478/intag-2013-0017.

Matejka F., Hurtalová T., Rožnovský J., Chalupníková B., 2005: Effect of soil moisture on evapotranspiration of a maize stand during one growing season. Contributions to Geophysics and Geodesy, **35**, 3, 219–228.

Naithani K. J., Ewers B. E., Pendall E., 2012: Sap flux-scaled transpiration and stomatal conductance response to soil and atmospheric drought in a semi-arid sagebrush

ecosystem. Journal of Hydrology, **464–465**, 176–185, doi: 10.1016/j.jhydrol.2012.07.008.

Nikolova N., Nejedlík P., Lapin M., 2016: Temporal variability and spatial distribution of drought events in the lowlands of Slovakia. Geofizika, **33**, 2, 119–135, doi: 10.15233/gfz.2016.33.10.

Penman H. L., 1948: Natural evaporation from open water, bare soil and grass. Proceedings of the Royal Society of London, Series A, **193, 1032**, 120–145, doi: 10.1098/rspa.1948.0037.

Procházková P., Chuchma F., Středa T., 2016: Drought severity in intensive agricultural areas by means of the EDI index. Contributions to Geophysics and Geodesy, **46**, 4, 289–305, doi: 10.1515/congeo-2016-0017.

Rožnovský J., Kohut M., Chuchma F., 2015: Agricultural drought during vegetation period in the Czech Republic. Towards to Climatic Services, Nitra, Slovakia, 1–5.

She D., Xia Y., Shao M., Peng S., Yu S., 2012: Transpiration and canopy conductance of Caragana korshinskii trees in response to soil moisture in sand land of China. Agroforestry Systems, **87**, 3, 1–10, doi: 10.1007/s10457-012-9587-4.

Skalák P., Štěpánek P., Farda A., 2008: Validation of ALADIN-Climate/CZ for present climate (1961–1990) over the Czech Republic. Időjárás, **112**, 191–201.

Škvarenina J., Tomlain J., Hrvol J., Škvareninová J., Nejedlík P., 2009: Progress in dryness and wetness parameters in altitudinal vegetation stages of West Carpathians: Time-series analysis 1951–2007. Időjárás, **113**, 47–54.

Středa T., Dostál V., Horáková V., Chloupek O., 2012: Effective use of water by wheat varieties with different root system sizes in rain-fed experiments in Central Europe. Agricultural Water Management, **104**, 2, 203–209.

Středová H., Chuchma F., Středa T., 2011: Climatic factors of soil estimated system. Bioclimate: Source and limit of social development. Topolčianky, Slovakia, Nitra: SPU in Nitra, 137–138.

Středová H., Středa T., 2015: Agroclimatic conditions of the Czech Republic – development and influence on agricultural production. Seed and seedlings. Praha: Czech University of Life Sciences Prague, 22–27.

Thompson N., Barrie I. A., Ayles M., 1981: The Meteorological Office Rainfall and Evaporation Calculation System: MORECS. Meteorological Office, Bracknell, **45**, 71 p.

Zeppel M. J. B., Macinnis-Ng C., Yunusa I. A. M., Whitley R. J., Eamus D., 2008: Long term trends of stand transpiration in a remnant forest during wet and dry years. Journal of Hydrology, **349**, 1-2, 200–213, doi: 10.1016/j.jhydrol.2007.11.001.

sciendo

Contributions to Geophysics and Geodesy Vol. 49/1, 2019 (37–66)

Review on the role of geoelectrical surveys in characterizing and deriving the constraints and hydrogeological conditions in semi arid Khanasser Valley region in Syria

Jamal ASFAHANI

Atomic Energy Commission, P. O. Box 6091, Damascus, Syria
tel: +963116111926; fax: 963116112289, e-mail: cscientific@aec.org.sy

Abstract: This paper is a general review which basically focuses on the role of geoelectrical surveys in characterizing and deriving the constraints and hydrogeological conditions in semi arid Khanasser valley region and its surroundings in Northern Syria. Schlumberger configuration has been used to carry out ninety six vertical electrical soundings VES, distributed on nine transverse and three longitudinal profiles. Their quantitative 1D interpretations with different techniques yield to develop several alternative approaches, that enable us to derive and determine the hydrological parameters of the structures controlled by the groundwater distributions. Two different northern and southern geological structures separated by Hobs-Serdah water divided line were electrically characterized. Both of them are of very conductive zones of a resistivity less than 4 Ωm, and related to the intrusion of salty water in Quaternary and Paleogene aquifers. The qualitative interpretation of the iso-apparent resistivity maps for different $AB/2$ spacings has allowed the delineation of those two structures. Those two identified structures have their evident influences on the distributions of thicknesses, resistivity, salinity, hydraulic conductivity, and transmissivity of both Quaternary and Paleogene aquifers. The high resistivity exceeding 300 Ωm on the measured VES is a very good signal of the presence of basalt formation of upper Miocene age in Jebel Al Hass in the west and Jebel Shbith in the east. The geometry and the electrical characteristics of Quaternary and Paleogene aquifers and the top of Maestrichtian have been well recognized. Quaternary paleosabkhas, fractured zones and tectonic features of the subsurface of Khanasser valley have been delineated through analyzing VES distributions along the executed longitudinal and transverse profiles. Different empirical relationships have been already established through coupling geoelectrical resistivity and hydrochemical data, which allows to derive and establish different salinity maps for different $AB/2$ spacings, and to outline the boundaries between fresh, brackish and saline waters. Two different alternative approaches have been also developed for geophysically computing and estimating the hydraulic conductivity and the transmissivity of the aquifers in the study region. The different hydrogeophysical approaches developed in this integrated geophysical research project for water resource management have been successfully applied in Khanasser valley, and can be recommended to be practiced in similar worldwide areas.

doi: 10.2478/congeo-2019-0004

Key words: electrical resistivity methods, hydrogeology, semi-arid regions, Khanasser valley, Syria

1. Introduction

The growing population problem and the development projects lead to increasing demand for groundwater as a national target. The application of very severe water management practical laws, however, have the ability to improve water quality and its use. Hydrogeological modeling procedure is a useful practice tool for water conservation and tables protection (*Jaworska-Szule, 2009; Takhur, 2016*), but sufficient details about groundwater quantity, quality and movements are required for its successful application. We cannot unfortunately use the boreholes of prohibitive coast to get a precise hydrogeological schema. The relevant solution is therefore to incorporate the geophysical measurements to allow and elaborate such an hydrogeological procedure.

The DC geoelectrical methods are considered as primary geophysical tools, that play a dominant role in groundwater exploration. In fact, the resistivity parameter is intrinsic in such water researches, and more controlled by the water-related attributes than by the resistivity value of solid rock. A subsurface sedimentary layer could be often subdivided into distinct geoelectrical units depending on the water content and the degree of salinity. Moreover, different empirical and semi empirical relationships have been already developed between the resistivity (ρ) and hydraulic conductivity (K) of an aquifer (*Chandra et al., 2008; Niwas and Singhal, 1985; Niwas and Singhal, 1981; Heigold et al., 1979; Kelly, 1977*). Different power empirical law equations have been thereafter constructed between the different aquifer parameters and those obtained by geoelectrical resistivity techniques (*Massoud et al., 2010; Attwa et al., 2009; Soupios et al., 2007; Purvance and Andericevic, 2000; Arétouyap et al., 2015, 2017, 2018; Tizro et al., 2010, 2012; Kazakis et al., 2016; Niwas et al., 2011; Niwas and Celik, 2012*).

Apparent resistivity measurements (ρa) obtained through application of the geoelectrical (DC) methods are used to derive the resistivity distribution in the subsurface medium. The field resistivity data are quantitatively interpreted, where different possible solutions could by obtained by the inversion methods. The only inversed acceptable solution model is the one,

which produces the best fit between measured apparent resistivity data and theoretical generated curve. The 1D inversed layered model is assumed while interpreting the vertical electrical sounding (VES), if the subsurface is basically 1D in the vicinity of the sounding location, and if the perturbations due to shallow lateral inhomogeneities are minimal. The 1D inversion practiced in this research for interpreting the field VES resistivity data has given quite reasonable results regarding the evaluated depths of geological interfaces in the study region. The VES technique is therefore still common and largely used for deep groundwater exploration problems, especially in semi-arid areas (*Skinner and Heinson, 2004; Asfahani, 2007a; Asfahani, 2010a; Chandra et al., 2010; Eleraki et al., 2010; Khalil, 2012; Metwaly et al., 2012*).

The study area is one of the integrated research sites of International Centre for Agriculture in Arid Dry Areas (ICARDA) National Resource Management Program. The choosing of this site is justified by addressing problems attached to the marginal dry land environments. The poverty and the relative easy accessibility, the diversity and dynamics of the natural resources and livelihoods, make the study region of Khanasser valley as a suitable prime candidate. The scientific program in this site includes regular monitoring of ground water levels and water chemistry, water use assessment, recharge studies, pumping tests, and geoelectrical investigation surveys. All those mentioned applied techniques in this project are oriented towards providing information for the formulation of sustainable resource management strategies and determining potential ground-water use. It is a fruit of collaboration between three scientific organizations, Syrian Atomic Energy Commission (AECS), ICARDA, and Bonn University, Germany.

This paper represents a general review that describes, summarizes and concentrates on the applications of the geoelectrical VES technique for solving different hydrogeological problems encountered in the semi arid regions such as Khanasser valley, Northern Syria (Fig. 1). This review paper aimed therefore at clarifying the integrated geoelectrical results that we have already obtained during the realization of this above project. The interested readers however are advised to consult our different cited papers in order to get more detailed information about all the different technical approaches discussed in this present review. The ten specific cited related papers, treating the different developed approaches, have discussed in more details all

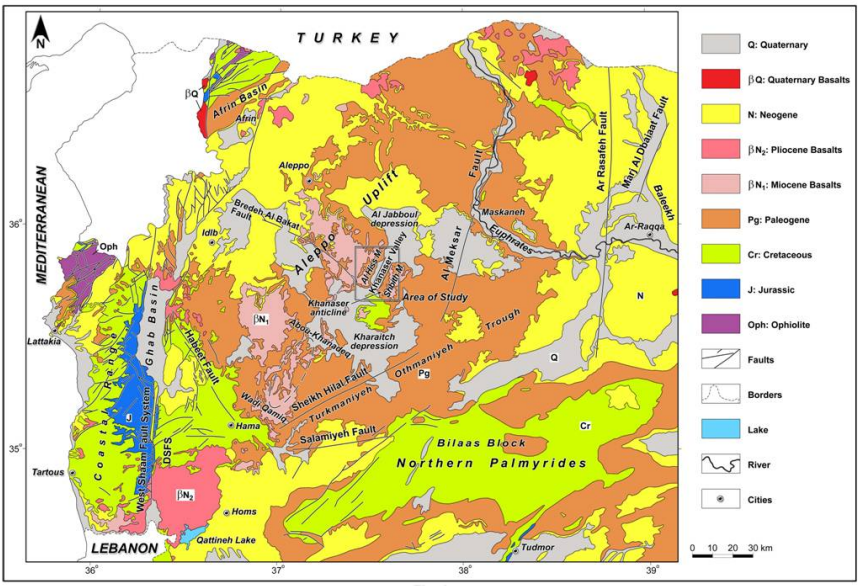

Fig. 1. Location of the Khanasser valley, Northern Syria and its geology.

the technical aspects related to the assumptions and interpretations.

The main objectives of the geoelectrical surveys carried out in Khanasser valley and its surroundings are therefore to cover the following geophysical research topics:

1. Determine the geometrical characteristics of both Quaternary and Paleogene aquifers in the Khanasser valley, and basalt of Al-Hess and Shbith mountains.
2. Clarify the tectonic and evolution scenario characteristics of the study area, especially the geological structures related with groundwater distribution.
3. Relate the geoelectrical resistivity data with aquifer hydrogeological parameters and transfer the measured resistivity maps to subsurface salinity and groundwater quality maps.
4. Evaluate the salt water intrusion phenomenon in the studied Khanasser valley region.
5. Determine the groundwater flow directions in the Quaternary and Pale-

ogene aquifers in the Khanasser valley by using circular multi directional VES.

6. Develop and apply purely alternative geophysical approaches for deriving the hydraulic parameters of the aquifers in the study area.

2. Geology and Hydrogeology

Khanasser Valley of north-south direction is located in Northern Syria, approximately 70 km southeast of Aleppo city, and directly south of the salt lake of Jaboul. It is located 300–400 m above sea level, between the hill ranges of Jebel Al Hass in the west and of Jebel Shbith in the east as indicated on the Khanasser valley geological map (Fig. 1). The Maestrichtian "Cr2m", is the oldest formation in the area, and considered as a water-confining layer of 150–200 m thickness (*Ponikarov, 1964*). The lithological outcrops of the study Khanasser valley consist of clay, clayey limestone flints, marl. The phosphate interbeds are observed in the southern part of the valley region.

The maximum thickness of the Paleogene formation "Pg", situated on the top of Maestrichtian, is more than 220 m. It consists of clayey, chalky limestones and silicified limestones, related to Lower Eocene and the Middle Eocene formations (*Ponikarov, 1964*). Localized aquifers with low productivity are contained in both the middle and the lower Eocene (*ACSAD, 1984*).

On the top of the Paleogene rock, the Upper Miocene basalts, "BN1,3", are located and found in the west on Jebel Al Hass, and in the east on Jebel Shbith. These basaltic formations of an average thickness of 10 m, and a maximum of more than 40 m do not contain ground-water resources in the Khanasser valley.

The Quaternary deposit of more than 25 m thickness exists in the centre of the valley, and consists of alluvial and lacustrine, proluvial, deposits. We can also find the gypsum in the lacustrine deposits. The Quaternary formation holds unconfined ground water in conglobreccia and sometimes in sand.

The semi-arid conditions dominate the valley, located at the fringe of the Syrian steppe (*Hoogeveen and Zobisch, 1999*). The valley is characterized

by an annual rainfall of 200–250 mm, with high annual and inter-annual variability (*Soumi, 1991*). The total surface of the study Khanasser valley is 322.5 km^2. The Khanasser valley is composed of a gently undulating plain with a wide shallow network dry erosion channels. The hill ranges of Jebel Shbith and Jebel Al Hass form calm rolling plateaus, which end in well-defined steep scarps towards the Khanasser valley with V-shaped erosion channels.

Hydrologically, Khanasser Valley is located on the border between two surface water catchments (*Wolfahrt, 1966, 1967; Hoogeveen and Zobisch, 1999*). The surface water drains towards a salt depression (Sabkha) in the southern part of the steppe catchment. The Jaboul catchment is related to the northern part, in which the drainage pattern is directed towards the Jaboul salt lake. Those two basins are separated by a dividing line between Al Hobs and Serdah villages (Fig. 2).

The scarcity and the salinity of water resources increasing from south to north are regarded as the main serious obstacle in the development of the Khanasser study region.

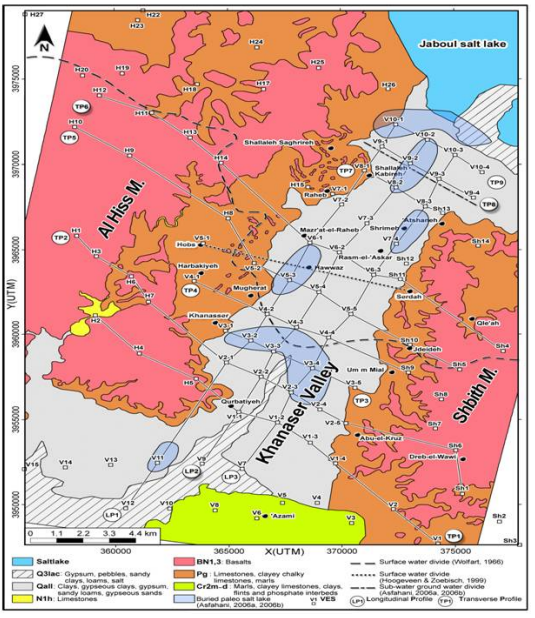

Fig. 2. Locations of the field VES in the Khanasser valley and its surroundings.

3. Geoelectrical Resistivity Field Surveys

Geoelectrical surveys have been applied in the Khanasser valley and its suroundings to electrically characterise the behaviour of both Quaternary and Paleogeane aquifers in lateral and vertical directions. Vertical electrical resistivity sounding (VES) is the main geoelectrical technique applied in this research.

Vertical Electrical Soundings (VES):

The vertical electrical resistivity variations of the subsurface formations in the Khanasser valley have been studied and characterized by applying the Vertical Electrical Sounding (VES) technique. Ninety six VES with a Schlumberger configuration have been measured in the Khanasser valley and its surroundings. The locations of those VES are shown on Fig. 2.

The *two* A and B electrodes in the applied Schlumberger configuration are used to impose the electrical current I on the study area, at varying spacing expanding symmetrically from a central point. The maximum distance between A and B of 1000 m ($AB/2 = 500$ m) has been adapted for all the VES carried out in the Khanasser study region. An additional pair of electrodes M and N at appropriate spacing are used to measure at the surface the resulting potential field ΔV.

The field apparent resistivity (ρa) obtained by applying Schlumberger array is given by the following equation:

$$\rho a = \frac{2\pi}{\frac{1}{AM} - \frac{1}{BM} - \frac{1}{AN} + \frac{1}{BN}} \frac{\Delta V}{I}, \tag{1}$$

where I is the current introduced into the earth, ΔV is the potential measured between the potential electrodes. *AM, BM, AN,* and *BN* are the distances between the different current and potential electrodes.

The resistance $\Delta V/I$ is directly measured with an Indian equipment (ACR-1), which allows to obtain subsequently the apparent resistivity (ρa) according to Eq. (1) (*Dobrin, 1976*).

The VES technique is based on the reality that the fraction of current injected into the ground penetrating below a given depth, increases with augmenting successively the separation between the electrical current A

and B electrodes. By such a VES procedure, the electrical resistivity variation with the depth below a given point on the earth surface could be easily obtained and estimated. Thus the electrical potential distribution on the surface of the earth will be affected relatively more by deep-lying inhomogeneities within the earth.

The increase of the electrode spacing $AB/2$ about a fixed point, allows to successively establish the apparent field resistivity curve "ρa" as a function of $AB/2$. *The established field resistivity curves will be used for qualitative and quantitative interpretations as will be documented and explained in this paper.*

Curve matching technique with the use of master curves (*Orellana and Mooney, 1966*) is applied and practiced to interpret the resulting field resistivity curves "ρa", and to get the initial determination of thicknesses and resistivities of corresponding layers (initial approximate model). Inverse technique program is thereafter used to accurately interpret the parameters of the approximate model, until a goodness of fit between the field apparent resistivity curve and the regenerated computed curve is obtained (*Zohdy and Bisdorf, 1989; Zohdy, 1989*). A grid comprising nine transverse profiles oriented approximately NW–SE (Fig. 2), labelled $TP1, TP2, \ldots, TP9$, and three longitudinal profiles ($LP1$, $LP2$ and $LP3$) has been designed to distribute the ninety six VES measured in the Khanasser valley. The distance between profiles was approximately 1 km and a VES was generally made every kilometer long each profile (especially in the valley itself). This observation interval was sometimes changed according to the topographic conditions (*Asfahani, 2007b*).

4. Results and Discussion

The Quaternary and Paleogene aquiferes have been described and characterized in details by conducting an integrated geoelectrical research in the study Khanasser valley, Northern Syria. The application of the geoelectrical technique is aimed at solving different hydrogeological problems, posed in the study area. Ninety six vertical electrical soundings (VES) have been therefore executed and measured in the Khanasser valley and its surroundings. The qualitative and quantitative interpretations of those 96 VES allow

us to reach several important hydrological results at two qualitative and quantitative levels as follows:

At qualitative level, the analysis and the study of the iso-apparent resistivity lines corresponding to different spacings $AB/2$ (from 3 m to 500 m) reveals essentially the presence of two hydro-geological structures. One is located in the north and the other one is located in the south in the Khanasser valley region. Those two identified structures are separated by joining line of Hobs and Serdah, where a clear deep tectonic effect is present along this joining line (*Asfahani, 2007b*).

The northern structure, which is an elongated conductive zone of N36°E direction with a very low resistivity (less than 4 Ωm) is the expression of saline groundwater intrusion in the Quaternary and Paleogene deposits. The same direction of N 36°E is remain kept for all the studied $AB/2$ spacings, which obviously indicates to the hydraulic connection between Quaternary and Paleogene in this northern structure.

The southern structure is also an elongated conductive zone of N62°E, direction with also a very low resistivity (less than 4 Ωm), due to the saline groundwater intrusion in Quaternary and Paleogene deposits (*Asfahani, 2007b*). In this southern structure, a clear separation between Quaternary and Paleogene is signalled. In fact, this result is confirmed and sustained by the fact that the axis of the conductive zone related to the Paleogene deposit becomes perpendicular to that of Quaternary at $AB/2$ spacings above 150 m. In addition, the dimensions of the southern structure attenuate at $AB/2$ spacings greater than 200m. A composite model of the spatial evolution of the two identified north and south structures is shown in Fig. 3 for $AB/2$ of 70, 100, 150, and 200 m.

At quantitative level, the assumption of one-dimensional layered models 1D is taken into consideration in this research. Curve matching technique with its master curves are used to determine an approximate model including resistivities and thickness of coresponding layers. An inverse technique program (Resist software) is thereafter used to invert this approximated model and to get the final optimum solution model. A typical field example of VES curve at VES points 10-4 and its quantitative 1D interpretation model is shown in Fig. 4.

The inversed interpretative VES results are calibrated in this research

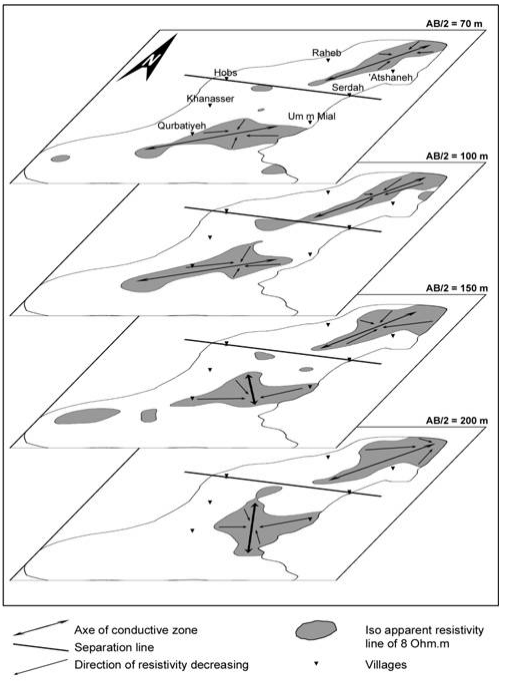

Fig. 3. Composite model for the two northern and southern structures for $AB/2$ of 70, 100, 150, and 200 m in the Khanasser valley (*Asfahani, 2007b*).

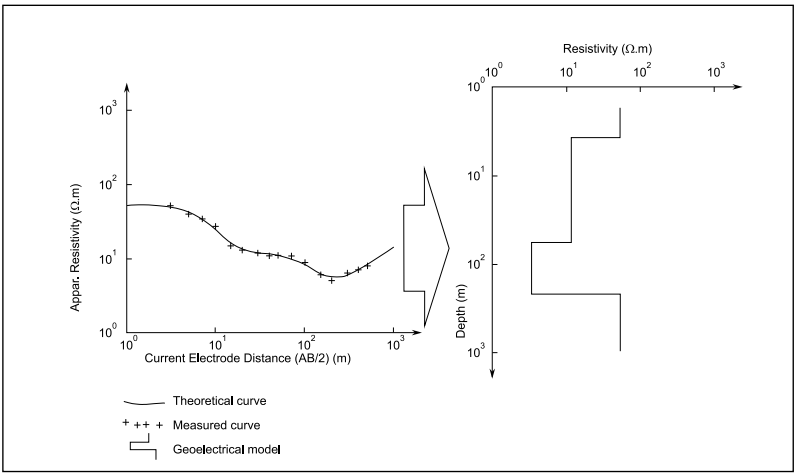

Fig. 4. Field VES at VES point 10-4 with its 1D quantitative interpretation (*Asfahani, 2007b*).

through:

- Geoelectrical response acquired of different formations surface outcrops. Each geological formation is characterized by a range of resistivity response, that must be geostatisticaly treated in order to be considered as an electrical signature for that formation. This procedure helps in delineating the subsurface extension.
- Geological cross-sections constructed from the available geological map of the area, that we compare and integrate with the obtained VES interpretation to establish a trustable subsurface image.

We could not use the available drilled wells in the study area as a source of information for the calibration, because they are of very shallow depth (< 70 m) and have no lithological description logs.

The 1D VES interpretative results obtained in this integrated geophysical research allow to solve different hydrogeological problems in the Khanasser valley as follows:

1) Determine the geometrical characteristics of both Quaternary and Paleogene aquifers in Khanasser valley. The Quaternary aquifer thickness varies between a minimum of 4.5 m at the VES V4-3 (3.3 km east of Khanasser) and a maximum of 99.4 m at the VES V9-2, 1.9 km northeast of Shallaleh Kabireh, with an average of 38.5 m. Its resistivity varies between 4.1 Ωm and 43 Ωm, with an average of 15.3 Ωm (*Asfahani, 2007b*). The Paleogene thickness varies between a minimum of 54 m at VES V11 and a maximum of 283 m at VES V4-3, with an average of 162.4 m. Its resistivity varies between 1.7 Ωm and 16 Ωm, with an average of 5.1 Ωm (*Asfahani, 2007b*).

   The top of Maestrichtian is also established. It varies between a minimum of 60.2 m at VES V1 and a maximum of 353.5 m at VES V4-4, with an average of 193.7 m. Its resistivity varies between 16 Ωm and 113 Ωm, with an average of 49 Ωm. The high resistivity of the Maestrichtian formation signaled at few locations in the study region (order of 110 Ωm) is due probably to the presence of phosphate.

   The influence of Basalt formation on the established iso-apparent resistivity maps is very well pronounced, enabling to eaisly trace and follow the boundaries of this formation, particularly in Jebel Al Hass. From the different iso-apparent resistivity maps, it is evident that basalt formation

goes down deeply. Basalt thickness in Al Hass varies between 19 m and 95.5 m, with an average of 51 m, and basalt resistivity varies between 159 Ωm and 804 Ωm, with an average of 380 Ωm. The thickness of basalt in Jebel Shbith varies between 29 m and 61 m, with an average of 44 m, while its resistivity varies between 110 Ωm and 241 Ωm, with an average of 166 Ωm (*Asfahani, 2007b*).

Fig. 5 (a and b) shows the variations of both thickness and resistivity of Quaternary, Paleogene and basalt along the longitudinal *LP1* and the transverse *TP5 profiles.*

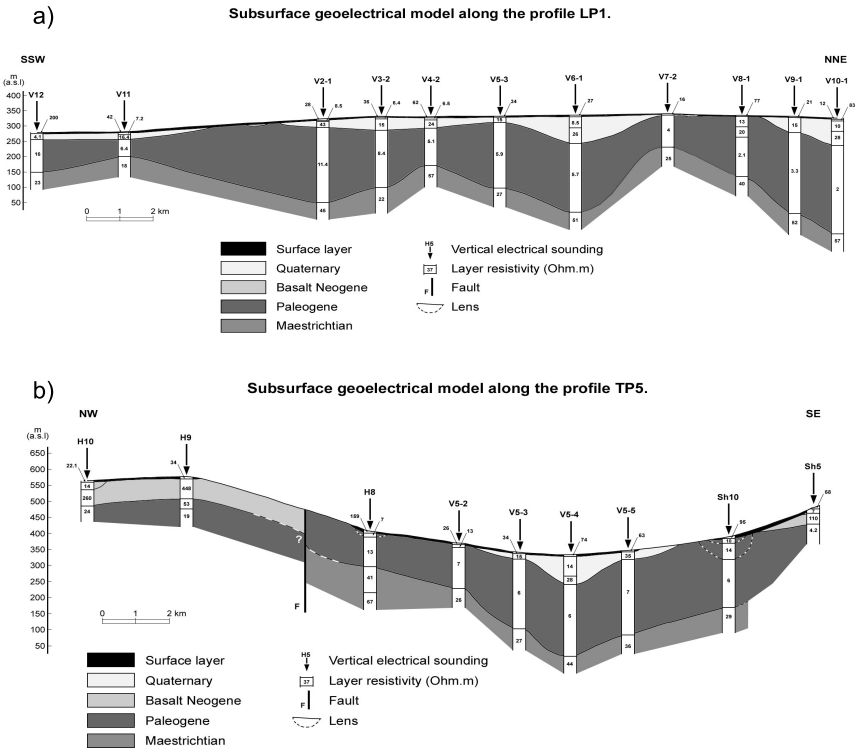

Fig. 5. Geoelectrical sections along *LP1* (a) and *TP5* (b) profiles (*Asfahani, 2007b*).

2) Pichgin and Habibullaev technique (see *Pichgin and Habibullaev, 1985*), which has been already modified and improved by *Asfahani and Radwan (2007)* is widely used in this integrated geoelectrical research to

interpret the VES data distributed along the studied longitudinal and transverse profiles. It enables to precisely define the subsurface structures and the fracured zones by using the concept of non homogeneity points "+", whose distributions reflect them strongly. The twelve executed transverse and longitudinal VES profiles have been interpreted by this technique, where interesting subsurface tectonic features have been imaged and delineated. Figs. 6 (a, b, c) and Fig. 7 show examples of using this technique for interpreting *LP2, TP1, TP6* and *TP8* profiles. The integral geophysical-tectonic interpretation of those profiles allows to determine the tectonic and evolution scenario characteristics of the study Khanasser valley region, especially the geological structures related with groundwater distribution. A reliable, fast, and economical approach applicable in arid areas of prominent relief and topography in dry areas has also been proposed to detect subsurface structures hence locating favorable and promising sites to drill fresh groundwater wells (*Asfahani and Radwan, 2007*). The valley was developed as a differentially subsiding graben during Quaternary and served temporarily as Paleo-Euphrates' course.The differential subsidence of the Khanasser graben's blocks formed characteristic structures of sharp rough morphology, smoothed later by the Paleo-Euphrates running water effect. This Khanasser graben became a greater lake extending from Al Jabboul depression to Kharaitch depression. The large paleo lake shrank gradually to its current borders, leaving behind the buried paleo salt lakes, whose locations and extensions fit very well with subsurface structures mapped by *Asfahani (2007b), Asfahani and Radwan (2007)* (Fig. 2).

The mapped subsurface horst structure groundwater divide, delineated at the center of Khanasser valley along the transverse *TP8* profile (Fig. 7) separates between the northern and southern structures. The northern one is a deeper low structure, open to the Al Jabboul salt lake with more saline water due to a southward subsurface flow. The southern one is a shallower structure with saline, brackish and fresh water, which might be explained by local dilutions caused by a runoff percolation through dense faulting networks, (Fig. 7). The groundwater divide line determined already by *Asfahani (2007b)*, is close to the surface water divide already delineated by *Hoogveen and Zobisch (1999)* rather than to that suggested by *Wolfahrt (1966)*, to the south near Khanasser town.

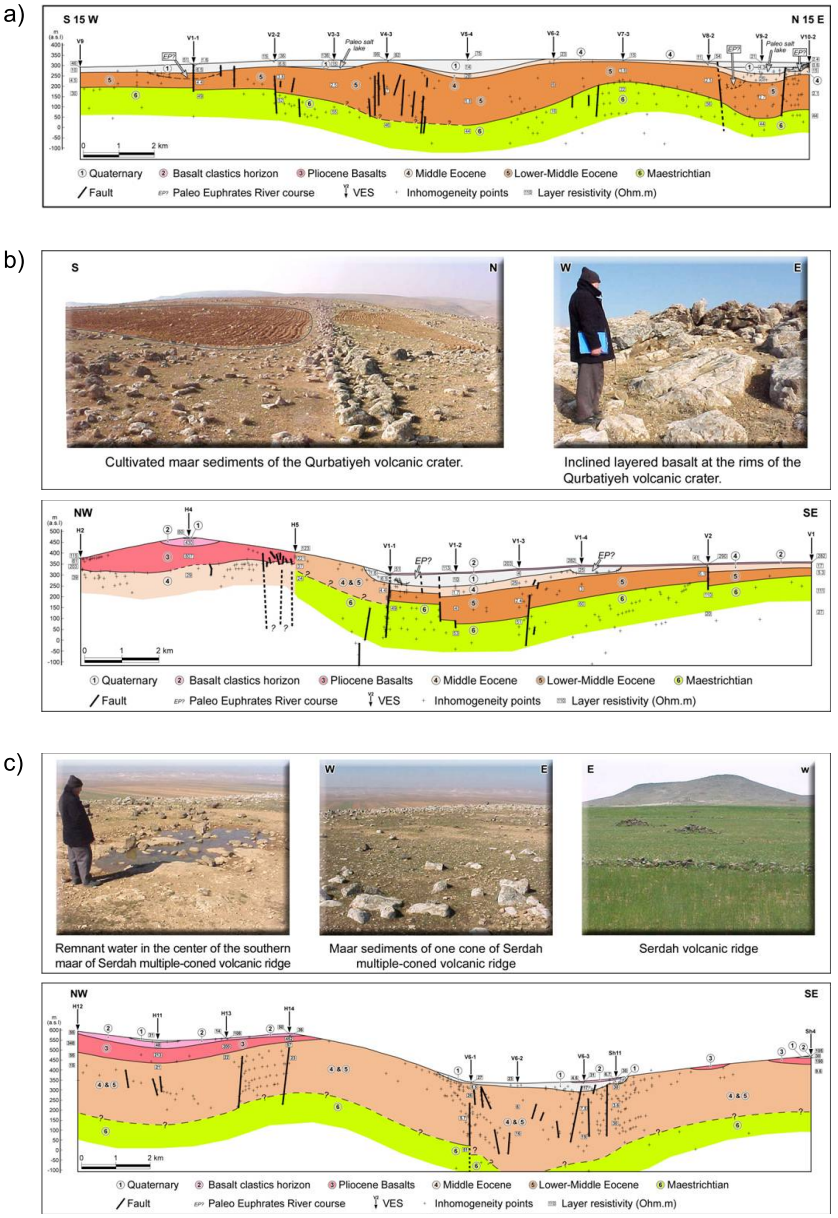

Fig. 6. Geoelectrical sections along *LP2* (a), *TP1* (b) and *TP6* (c) profiles, derived by Pichgin technique (*Asfahani and Radwan, 2007*).

Ground water flowed from this subsurface divide in the NNE direction toward the Al Jabboul depression and in the SSW direction toward the Kharaitch depression, as mentioned by *Asfahani (2007b)*.

The tectonic-oriented interpretation of the mentioned twelve profiles, explains the origin of the Khanaser Valley as N15_E deep normal faults, formed by the E–W tension which dominates in the northernmost parts of the Arabian plate. Those deep faults served as basaltic lava conduits before developing into a graben, whose central dissected blocks underwent a differential subsiding. The role of those dense faulting within the Khanasser Valley in mixing saline and fresh water is not excluded. Sulfuric water encountered in some wells drilled in the Khansser Valley may be attributed to the partial percolation of rainfall surface run-off, through bituminous chalky limestone middle Eocene intercalating levels.

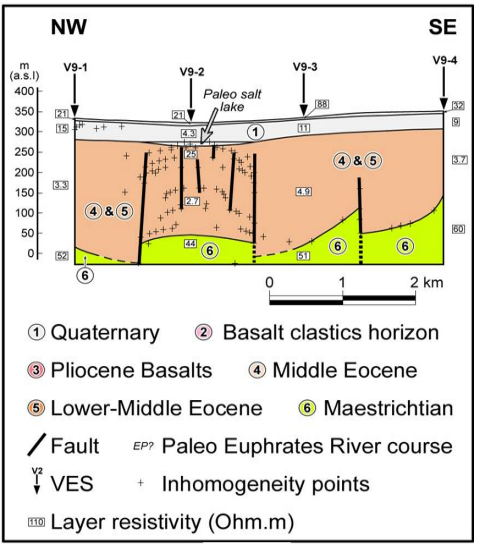

Fig. 7. Geoelectrical horst section along *TP8* profile, derived by Pichgin technique (*Asfahani and Radwan, 2007*).

3) The second concern in this hydrogeophysical investigation in the Khanasser valley is to attach the measured geoelectrical resistivity data with the aquifer hydrogeological parameters in order to transfer the established resistivity maps to subsurface groundwater quality and salinity map. The conductivity (σw) and the TDS of well-water samples exist at the vicinity

of some VES locations are calibrated together with the earth resistivities estimated from VES sounding. This is done to get empirical relationships between earth resistivity and water resistivity, and subsequently between earth resistivity and total dissolved solids (TDS), (*Asfahani, 2007c*).

Regression analysis applied on such hydrogeophysical data indicates the following empirical relationship between earth resistivity and TDS concentration.

$$\rho e = -0.0028\, TDS + 15.237\,. \tag{2}$$

According to this empirical relationship, the iso-resistivity lines of 5, 10 and 15 Ωm represent a salinity of 2844, 1935 and 1025 ppm respectively, (*Asfahani, 2007c*). It is worth mentioning that the earth resistivity values resulting from VES interpretation are representative of the Quaternary saturated zone, where the real resistivity layer corresponding to water sampling depth location was taken.

This calibrated regression relationship is used to convert the iso-apparent resistivity maps corresponding for $AB/2$ of 70, 100 and 150 m into salinity maps. The obtained salinity maps corresponding to penetration depths of 70, 100 and 150 m clearly indicate the presence of the two mentioned geological structures trending of N36°E and N62°E. Fig. 8a shows an example of the salinity map obtained in the Khanasser valley for a constant $AB/2$ of 100 m, for which the distribution of iso-saline lines clearly indicates the directions of water movement in the study region of Khanasser Valley.

Fig. 8b shows the cross sectioanl variations of the salinity along the longitudinal profile *LP3* as a function of $AB/2$ (*Asfahani, 2010b*).The iso-TDS countours have tendancy to be allongated and directed towards the surface between V1-2 and V3-4 in the high TDS region, due to the excessive fresh water depletion in this area. The quality of groundwater is affected by such a depletion and by the ascent of saline ground water deep flow, that must be avoided. The positions of the faults shown in the Fig. 8b are determined through interpreting VES data distributed along *LP3* by Pichgin and Habibuleave technique described above (*Asfahani, 2010b*).

The distribution of fresh (ρe between 10 and 15 Ωm), brackish (ρe between 5 and 10 Ωm) and salt water zones ($\rho e < 5\,\Omega$m), and their

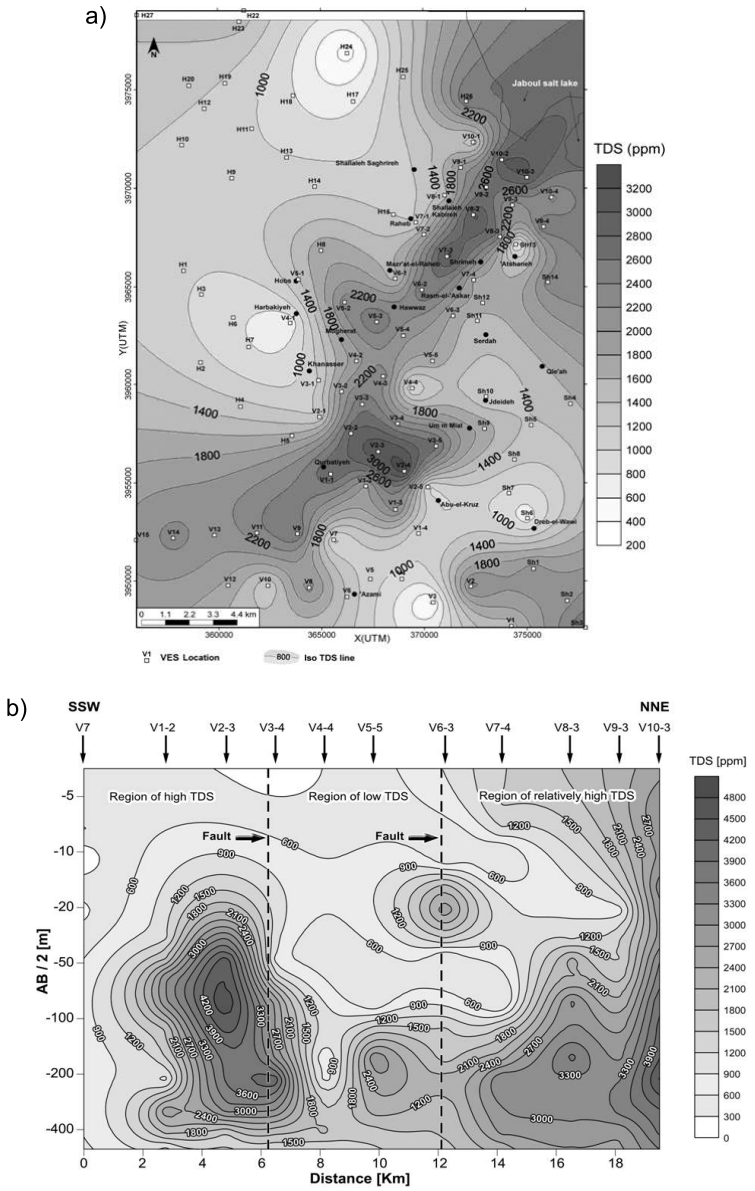

Fig. 8. (a) Salinity map for a constant $AB/2$ of 100 m in the Khanasser valley (*Asfahani, 2007c*); (b) Salinity map as a function of $AB/2$ along $LP3$ in the Khanasser valley (*Asfahani, 2010b*).

variations in space along the longitudinal profiles $LP1, LP2, LP3$ were established through converting depth quantitative interpretative models into different groundwater areas (*Asfahani, 2007c; Asfahani, 2010b*). Fig. 9 shows the distribution of those different zones obtained through integrating the results obtained for $LP1, LP2$, and $LP3$ in the Khanasser valley. The depths of interface between different water zones were determined, that must be used for proper ground-water management.

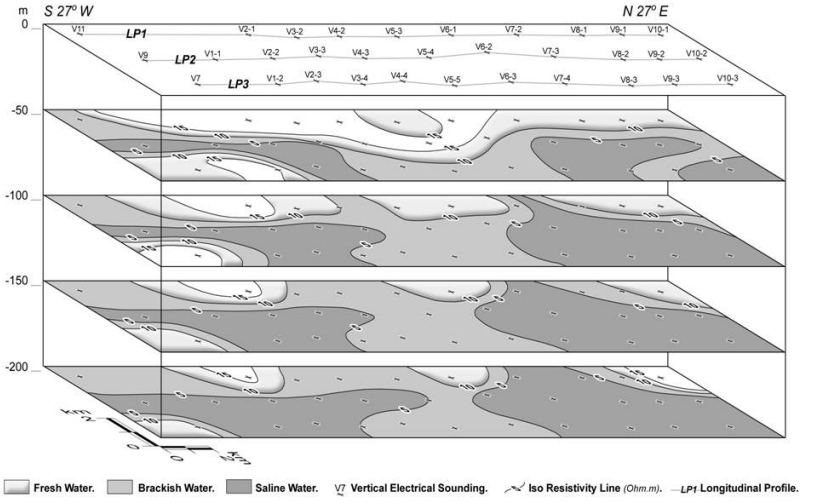

Fig. 9. Several water zones along *Lp1, Lp2*, and *Lp3* in the study Khanasser valley region (*Asfahani, 2010b*).

4) The salt water intrusion signalled in the northern part of the Khanasser valley has been also taken into consideration and studied in more details through interpreting and analyzing the profile (*Pr-1*) of 8.67 km long and of NE–SW direction. Aditional VES measurements called VB1 to VB15 have been carried out at the north of Hobs-Serdah water divide line for this intrusion purposes as shown in Fig. 10a, (*Asfahani and Abou Zakhem, 2013*). RES2DINV program is used to interpret the raw resistivity data of nine VES distributed along *Pr-1*, and to obtain the 2D inverted resistivity model as shown in Fig. 10b. The inverted model with rms of 4.9% is obtained after 5 iterations, where a real penetration depth of 80 m is reached for the lithological section corresponding for $AB/2$ from

3 to 200 m. The RES2DINV results obtained along the analyzed *Pr-1* are in an acceptable agreement with those obtained by traditional VES interpretations discussed in this paper. The evaluated TDS values computed for different $AB/2$ spacings by applying the constructed empirical relationship (3) (*Asfahani, 2007c*) between the interpreted earth resistivity and TDS concentration were traced along the *Pr-1* as a function of the $AB/2$ spacings (Fig. 10c). The arrows shown in Fig. 10c indicate obviously to the salt water propagation, reaching the surface at the VB5 location, where the contact between saline and brackish water is drawn.

Fig. 10c shows a supposed movement of saline groundwater from Jaboul salt lake towards the south, as a result of the intensive pumping and a subsequent lowering of the groundwater table. The fact that there was a groundwater divide in the middle of the valley between Atshaneh and Rasm Asker in the first half of May 2002, when pumping was still going on cannot sustain a groundwater flow caused by a hydraulic gradient towards the southern region. The salts could actually moves towards the hydraulic divide line in the form of a dense saline layer moving southward in the lower Eocene and Quaternary, where the surface of this formation was dipping to the south direction and the leakage factor of the old lake or periodical transgressions during the wet season permitted the intrusion of salt water (*Hoogeveen and Zobisch, 1999*).

The general trends of the intrusion phenomenon discussed above are also shown on the constructed geoelectrical lithological section of *Pr-1*, where three zones of groundwater quality are depicted (Fig. 10d). These zones are fresh water ($\rho e > 10\,\Omega$m), brackish (ρe between 5 and 10 Ωm) and saline groundwater ($\rho e < 5\,\Omega$m). The interfaces existing between those different water zones are also traced, where a large extension of the brackish water is observed, indicating almost its dominance along this *Pr-1* section. A remarkable low-resistive anomaly, reaching the surface, is also depicted at the VB5 location, where the well 97 of a depth of 40 m is located. This resistivity anomaly may indicate a probable saline groundwater up-coning through Quaternary deposits resulting from the intense fresh water pumping. The excessive fresh-water depletion affects therefore largely the groundwater quality by upward of deep flow of saline water, that should be necessarily avoided. It is therefore required to monitor and keep the fresh-salt water interface in a stationary situa-

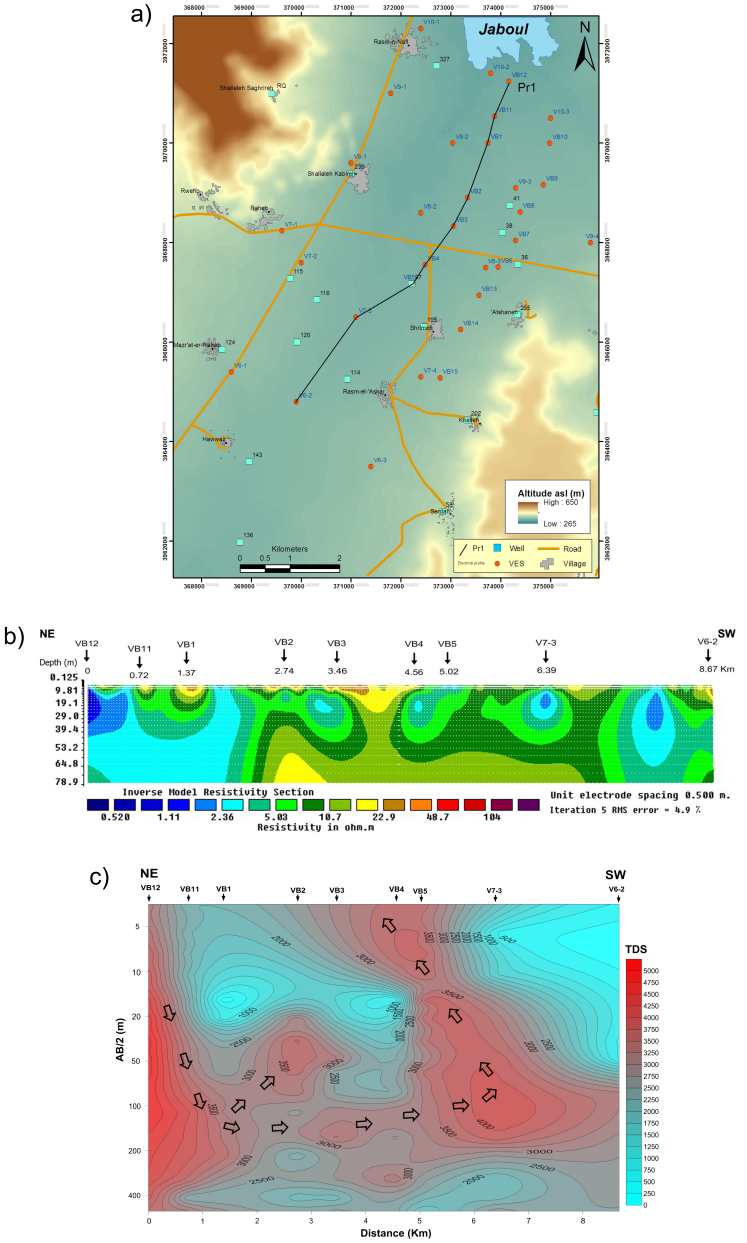

Continued on the next page.

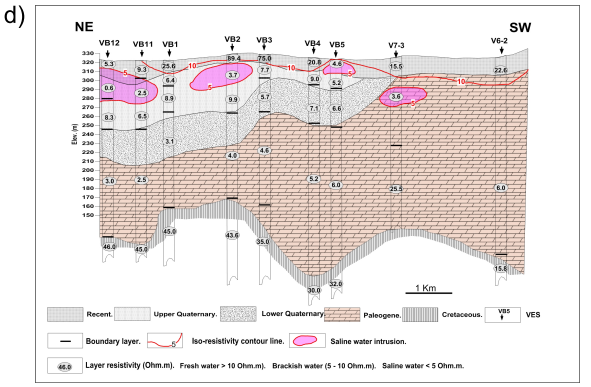

Fig. 10. (a) Location of *Pr-1* used for intrusion characterization in the Khanasser valley (*Asfahani and Abou Zakhem, 2013*); (b) 2D inverted resistivity model along *Pr-1* (*Asfahani and Abou Zakhem, 2013*); (c) TDS salinity map as a function of $AB/2$ along *Pr-1* (*Asfahani and Abou Zakhem, 2013*); (d) General intrusion trends observed along established geoelectrical *Pr-1* section (*Asfahani and Abou Zakhem, 2013*).

tion by pumping a limited amount of groundwater, and this depends on the available fresh water and the water balance in the region.

5) Azimuthal directional VES technique is practiced in this research project to delineate the groundwater flow directions in the Quaternary and Paleogene aquifers in the Khanasser valley region.

The apparent resistivity in the directional VES technique is measured for several directions through rotating an electrode array about its centre. Using this adapted effective technique, it is easy to determine the principal directions anisotropy, related directly to structural or lateral lithological changes in the subsurface (*Massoud et al., 2009; Taylor and Fleming, 1988*). The anisotropy is generally caused by the presence of fluid-filled fractures in a relatively resistive rock or soil.

Standard Schlumberger configuration is used to conduct three azimuthal resistivity soundings V6-3, V2-3, and V8-2 in the Khanasser valley along the azimuths of 0, 45, 90, and 135.

Resistivity values for different $AB/2$ spacings in V2-3 have been plotted on a polar diagram as shown in Fig. 11. The sedimentological nature of the Quaternary aquifer composed of proluvial, alluvial and lacustrine deposits is responsible on the provocation and the creation of the ob-

served anisotropy. It has been found for the three studied polar VES (V6-3, V2-3, and V8-2) a positive tendency between the transmissivity of the saturated Quaternary aquifer and the ratio of ρ_{min}/ρ_{max} (ratio of small apparent resistivity to the big apparent resistivity), for different $AB/2$ (*Asfahani, 2013*). The principal directions of groundwater flow are presented by the direction of ρ_{max} in the polar resistivity diagrams, as shown in Table 1.

Table 1. Principal directions of groundwater flow for different $AB/2$ in VES (2-3, 6-3, and 8-2).

VES No.	***AB*/2 (m)**	**Principal directions of groundwater flow**
VES 2-3	from 15 m to 500 m	NE–SW
VES 6-3	from 5 m to 50 m	N–S
	from 70 m to 500 m	NW–SE
VES 8-2	from 5 m to 40 m	N–S
	from 50 m to 200 m	E–W
	from 300 m to 500 m	NE–SW

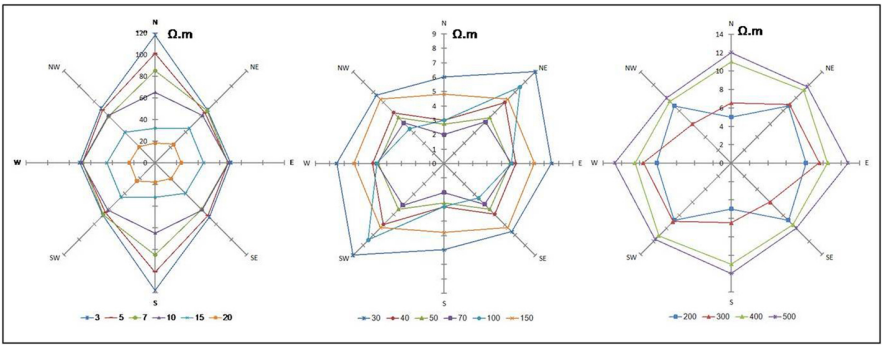

Fig. 11. Polar resistivity diagrams for different $AB/2$ in the VES 2-3 (*Asfahani, 2013*).

6) Two different purely alternative geoelectrical approaches have been developed, tested and applied during this integrated research project in the Khanasser valley region. They are designed for deriving and estimating the hydraulic parameters of hydraulic conductivity and transmissivity of both the Quaternary and Paleogene aquifers in the Khanasser valley.

The first alternative methodology takes the clay effect into account, where the hydraulic conductivity in the interpreted calibrated VES locations is firstly estimated by the use of Kozeny-Carman-Bear equation

(*Bear, 1972*). Calibrated VES soundings in this geoelectrical alternative technique are measured at the vicinity, where water samples taken from known depth of Quaternary aquifer are available. The transmissivity of the Quaternary in the Khanasser Valley is thereafter evaluated for those calibrated VES. A calibrated relation (3) between transverse resistance TR (TR is the product of the aquifer saturated thickness and its resistivity) and transmissivity T is consequently constructed, (*Asfahani, 2012, 2013*). This calibration relation permits thereafter to easily obtain the transmissivity and the hydraulic conductivity, even in the VES locations where no water samples exist.

The calibration relation constructed between TR and T has the following form (*Asfahani, 2012*):

$$TR = 5.758\ {}^{*}T^{1.015}\,, \tag{3}$$

with R^2 of 0.736.

According to the clay geoelectrical alternative approach, the transmissivity of the Quaternary aquifer in the Khanasser Valley attains its maximum of 131.6 m^2/day (Fig. 12a).

The transmissivity of the Paleogene aquifer is also estimated by adapting an average hydraulic conductivity (K) of 0.0054 m/day (*Asfahani, 2013*). The low productivity characterizes the Paleogene aquifer. Its transmissivity value varies between a minimum of 0.31 m^2/day observed at V2-3, and a maximum of 1.54 m^2/day observed at V4-3, with an average of 0.94 m^2/day as indicated in Fig. 12b (*Asfahani, 2013*). It has been well noticed many differences in hydrogeological characteristics between the north and the south of the Hobs-Serdah dividing line, already delineated by *Asfahani (2007b)*. A distinct relatively transmissive structure is observed at the south of this line, whereas the transmissivity is more complicated toward the north.

The second alternative geoelectrical methodology takes only the salinity of the groundwater into account (*Asfahani, 2016*). According to this approach, VES are firstly measured in the locations, where water samples are available. Empirical relationships between transverse resistance Dar-Zarrouck TR and modified transverse resistance MTR, and between MTR and transmissivity T are consequently constructed and calibrated for those VES points as follows:

$$MTR = 2.017^{*}\ TR - 91.84, \tag{4}$$

with R^2 of 0.691, and correlation coefficient of 0.83, and

$$T = 0.239^{*}\ MTR + 153.9, \tag{5}$$

with R^2 of 0.641, and correlation coefficient of 0.80.

Those two relationships (4) and (5) are thereafter applied and used to extrapolate and evaluate the transmissivity even in the VES points where no water samples exist. An acceptable agreement is noticed between the hydraulic conductivity values obtained by this alternative technique and those obtained by the four pumping tests, where those values range between 0.864 and 8.64 m/day (10^{-5} and 10^{-4} m/s). Fig. 12c shows the transmissivity distribution and hydraulic conductivity of the Quaternary Khanasser valley. It is shown that the transmissivity obtained by the salinity groundwater approach varies between a minimum of 79 m^2/day and a maximum of 814 m^2/day, with an average of 283 m^2/day and a standard deviation of 145 m^2/day. The average hydraulic conductivity of 13.8 m/day obtained by this second approach is overestimated in comparison with that obtained by the first alternative clay approach (2.23 m/day). This comparison between the two different developed approaches indicates to the importance of the clay effect, that must be taken into account. The presence of the clay considerably decreases the hydraulic conductivity of the studied aquifer, as it was demonstrated through the analysis of the Quaternary aquifer in the Khanasser valley region.

Finally, the present case study of Khanasser valley allows us to shows on a real field example how the geoelectrical survey can largely contribute in solving different hydrogeological problems in semi arid regions. The influences and interactions between the different hydrogeological constraints of the Quaternary and Paleogene aquifers in the Khanasser valley have been well discussed in this general review paper with a very detailed analysis. The salinity distributions and its variations in the Khanasser valley have been clarified through characterizing the two northern and southern hydrological structures delineated by *Asfahani (2007b)*.

The role of the geoelectrical surveys in characterizing and deriving the

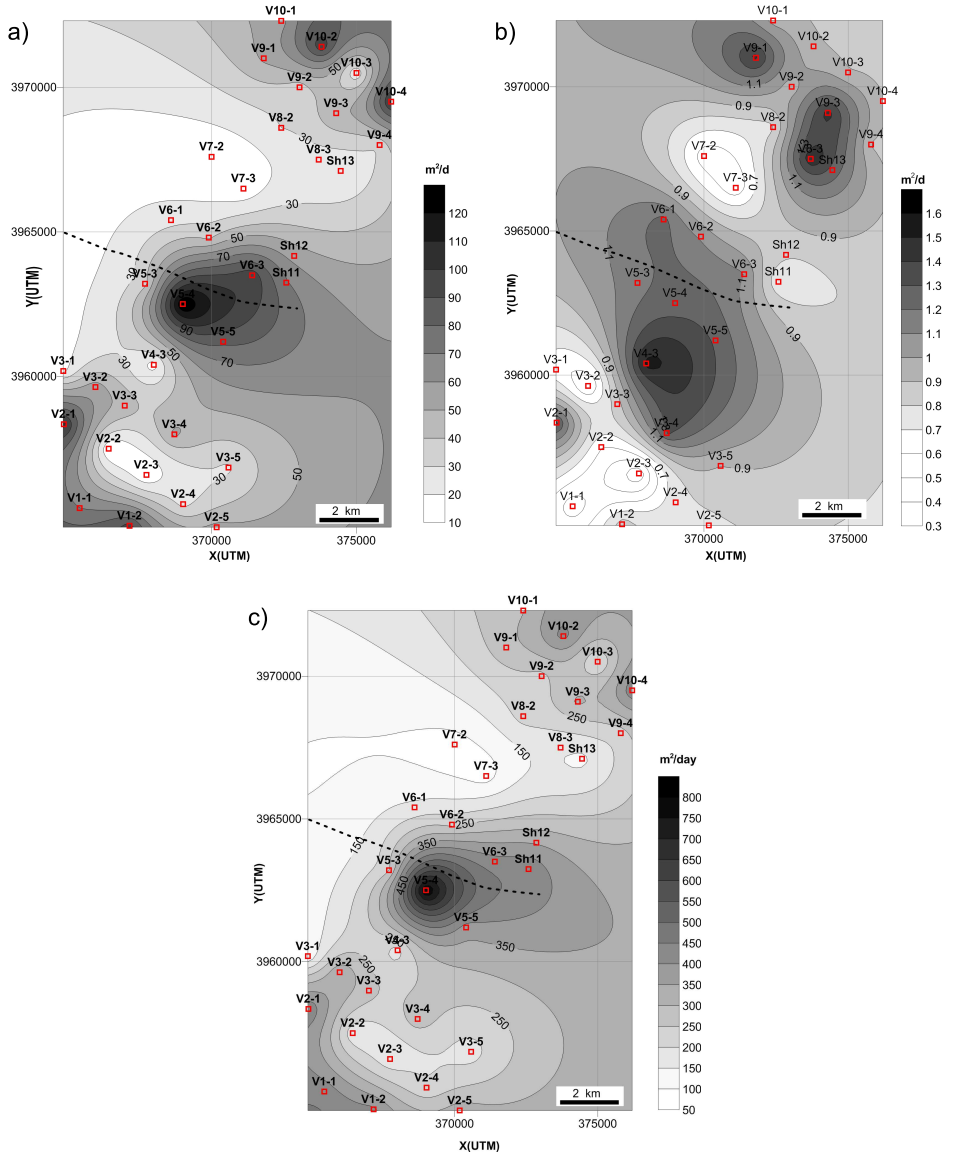

Fig. 12. (a) Established Quaternary aquifer transmisivity map derived by clay alternative approach in the Khanasser valley (*Asfahani, 2013*); (b) Established Paleogene aquifer transmisivity map in the Khanasser valley (*Asfahani, 2013*); (c) Established Quaternary aquifer transmisivity map derived by salinity alternative approach in the Khanasser valley (*Asfahani, 2016*).

hydrogeological conditions in semi arid Khanasser valley region in Syria has been proven. The cost of those surveys is relatively cheap, and their applications efficacy give rapidly important subsurface hydrological results. Those obtained results could be essentially required for future research managements and developments in the study region.

5. Conclusion

This general review paper describes and summarizes the main integrated following results that we have already obtained during the geophysical research project, carried out in the Khanasser valley:

1) The geometrical and electrical characteristics of both Quaternary and Paleogene aquifers in the Khanasser valley region have been well delineated. The depth to the top of Maestrichtian is also estimated. The subsurface basalt distributions in Jable Al-Hess in the west and Jable Shbaith in the east have been also characterized through interpreting the VES measurements, executed on those two Jables.
2) The iso resistivity lines obtained for all $AB/2$ spacings indicate the presence of two different hydrogeological structures, separated by Hobs-Serdah water divide line. Those structures have their specific influences on thicknesses, resistivity, salinity, intrusion, hydraulic conductivity, and transmissivity of both Quaternary and Paleogene aquifers.
3) The boundaries of buried paleosabkha have been well delineated.
4) All the tectonic features with the fractured zones have been delineated in the Khanasser valley region.
5) The intrusion phenomenon in the study region has been well discussed and documented.
6) Two alternative geoelectrical approaches have been developed, tested and successively practiced for estimating the hydraulic conductivity and the transmissivity of Quaternary and Paleogene aquifers in the Khanasser valley region. The first one takes the clay effect into consideration, while the second one takes only the salinity of groundwater into account. Their applications in the study region give convincible and reasonable results in comparing with the results obtained by pumping tests.

7) The role of geoelectrical surveys in characterizing and deriving the constraints and hydrogeological conditions in studying the semi arid regions is clarified through the present case study of Khanasser Valley region in Syria.

The geophysical information presented in this review paper is important, and could be regarded as a basic document for future advanced hydrological studies. All the different approaches developed in this geophysical research have been successfully applied in the semi arid Khanasser valley, and could be recommended for other similar worldwide areas.

Acknowledgements. Author would like to thank Dr. I. Othman, General Director of Atomic Energy Commission of Syria for allowing this integrated geoelectrical research results to be published. The German Ministry of Economic Cooperation and Development (BMZ) and German Agency for Technical Cooperation (GTZ) are acknowledged for financial and administrative support to the Khanasser Valley Integrated Research Site (KVIRS) project. Late Professor. Rieser Armins (coordinator of the project) from Bonn university, Germany is deeply thanked for many useful discussions during the preparation stages of this project. ICARDA is highly thanked for providing the facilities and the logistics during the realization of Khanasser Valley project. The anonymous reviewers are thanked for their critics and remarks that improved the final version of this paper. Dr. Igor Kohut, the editor of Contribution to Geophysics and Geodesy Journal is cordially thanked for his editing and collaboration with the author during the different stages of this publication.

References

ACSAD, 1984: Water Resources Map of the Arab Countries, The Arab Center for the Studies of Arid Zones and Dry Lands, Damascus, Syria.

Arétouyap Z., Nouayou R., Njandjock Nouck P., Asfahani J., 2015: Aquifers productivity in the Pan-African context. Journal of Earth System Science, **124**, 3, 527–539.

Arétouyap Z., Njandjock Nouck P., Nouayou R., Assatse W. T., Asfahani J., 2017: Aquifer porosity in the Pan-African semi-arid context. Environ. Earth Sci., **76**, 3, 134, doi: 10.1007/s12665-017-6440-0.

Arétouyap Z., Bisso D., Njandjock Nouck P., Amougou Menkpa L. E., Asfahani J., 2018: Hydrogeophysical Characteristics of Pan-African Aquifer Specified Through an Alternative Approach Based on the Interpretation of Vertical Electrical Sounding Data in the Adamawa Region, Central Africa. Natural Resources Research, **28**, 1, 63–77, https://doi.org/10.1007/s11053-018-9373-8.

Asfahani J., 2007a: Neogene aquifer properties specified through the interpretation of electrical sounding data, Sallamiyeh region, central Syria. Hydrol. Process, **21**, 2934–2943, doi: 10.1002/hyp.6510.

Asfahani J., 2007b: Geoelectrical investigation for characterizing the hydrogeological conditions in semi-arid region in Khanasser valley, Syria. J. Arid. Environ., **68**, 31–52, doi: 10.1016/j.jaridenv.2006.03.028.

Asfahani J., 2007c: Electrical earth resistivity surveying for delineating the characteristics of ground water in semi arid region in Khanaser Valley, Northern Syria. Hydrol. Process, **21**, 1085–1097, doi: 10.1002/hyp.6290.

Asfahani J., Radwan Y., 2007: Tectonic Evolution and Hydrogeological Characteristics of Khanasser Valley, Northern Syria, Derived from the Interpretation of Vertical Electrical Soundings. Pure Appl. Geophys., **164**, 2291–2311, doi: 10.1007/s00024-007-0274-8.

Asfahani J., 2010a: Application of surfacial geoelectrical resistivity technique in hydrogeology domain for characterizing saline groundwater in semi arid regions. In: Benjamin Veress, Jozsi Szigethy (Eds.), Horizons in earth science research series. NOVA Science Publishers, New York, **1**, 351–381.

Asfahani J., 2010b: Electrresistivity investigations for guiding and controlling fresh water well drilling in semi arid region in Khanasser Valley, Northern Syria. Acta Geophys., **59**, 1, 139–154, doi: 10.2478/s11600-010-0031-8.

Asfahani J., 2012: Quaternary aquifer transmissivity in semi arid region in Khanasser valley, Northern Syria. Acta Geophys., **60**, 4, 1143–1158, doi: 10.2478/s11600-012-0016-x.

Asfahani J., 2013: Groundwater potential estimation deduced from vertical electrical sounding measurements in the semi-arid Khanasser valley region, Syria. Hydrol. Sci. J., **58**, 2, 468–482, doi: 10.1080/02626667.2012.751109.

Asfahani J., Abou Zakhem B., 2013: Geoelectrical and hydrochemical investigations for characterizing the salt water intrusion in the Khanasser valley, northern Syria. Acta Geophys., **61**, 2, 422–444, doi: 10.2478/s11600-012-0071-3.

Asfahani J., 2016: Hydraulic parameters estimation by using an approach based on vertical electrical soundings (VES) in the semi-arid Khanasser valley region, Syria. J. Afr. Earth. Sci., **117**, 196–206, doi: 10.1016/j.jafrearsci.2016.01.018.

Attwa M., Günther T., Grinat M., Binot F., 2009: Transmissivity estimation from sounding data of Holocene tidal flat deposits in the north eastern part of Cuxhaven, Germany. Extended abstracts, Near Surface 2009: 15th European Meeting of Environmental and Engineering Geophysics, Dublin, Ireland, 7–9 September, 2009, P29 (Sub ID: 6710).

Bear J., 1972: Dynamics of fluids in porous media. Elsevier, New York.

Chandra S., Ahmed S., Ram A., Dewandel B., 2008: Estimation of hard rock aquifer hydraulic conductivity from geoelectrical measurements: a theoretical development with field application. J. Hydrol., **357**, 218–227, doi: 10.1016/j.jhydrol.2008.05.023.

Chandra S., Dewandel B., Dutta S., Ahmed S., 2010: Geophysical model of geological discontinuities in a granitic aquifer: analyzing small-scale variability of electrical resistivity for groundwater occurrences. J. Arid. Geophys., **71**, 4, 137–148, doi: 10.1016/j.jappgeo.2010.06.003.

Dobrin M. B., 1976: Introduction to Geophysical Prospecting. McGraw-Hill, New York.

Eleraki M., Gadallah M., Gemail K., Attwa M., 2010: Application of resistivity method in environmental study of the appearance of soil water in the central part of Tenth of Ramadan City, Egypt. Q. J. Eng. Geol. Hydrol., **43**, 171–184.

Heigold P. C., Gilkeson R. H., Cartwright K., Reed P. C., 1979: Aquifer transmissivity from sacrificial electrical methods. Ground Water, **17**, 4, 338–345.

Hoogeveen R. J. A., Zobisch M., 1999: Decline of groundwater quality in Khanasser valley (Syria) due to saltwater intrusion. Paper presented at the International Dryland Conference, Cairo, Egypt, August, 16 pp.

Jaworska-Szule B., 2009: Groundwater flow modelling of multi aquifer systems for regional resources evaluation: The Gdansk hydrogeological system, Poland. Hydrogeology Journal, **17**, 1521–1542.

Kazakis N., Vargemezis G., Voudouris K., 2016: Estimation of hydraulic parameters in a complex porous aquifer system using geoelectrical methods. Sci. Total Environ., **550**, 742–750.

Kelly W. E., 1977: Geoelectrical sounding for predicting aquifer properties. Ground Water, **15**, 420–425.

Khalil M. H., 2012: Reconnaissance of freshwater conditions in a coastal aquifer: synthesis of 1D geoelectric resistivity inversion and geohydrological analysis. Near Surf. Geophys., **10**, 427–441.

Massoud U., El Qady G., Metwaly M., Santos F., 2009: Delineation of shallow subsurface structure by azimuthal resistivity sounding and joint inversion of VES TEM data: case study near Lake Qaroun, El Fayoum, Egypt. Pure and Applied Geophysics, **166**, 701–719.

Massoud U., Santos F. M., Khalil M. A., Taha A., Abbas M. A., 2010: Estimation of aquifer hydraulic parameters from surface geophysical measurements: a case study of the Upper Cretaceous aquifer, central Sinai. Egypt Hydro. J., **18**, 699–710.

Metwaly M., Elawadi E., Moustafal S. S. R., Al Fouzan F., Mogren S., Al Arifi N., 2012: Groundwater exploration using geoelectrical resistivity technique at Al-Quwy'yia area central Saudi Arabia. Int. J. Phys. Sci. **7**, 2, 317–326.

Niwas S., Singhal D. C., 1981: Estimation of aquifer transmissivity from Dar-Zarrouk parameters in porous media. J. Hydrol., **50**, 393–399.

Niwas S., Singhal D. C., 1985: Aquifer transmissivity of porous media from resistivity data. J. Hydrol., **82**, 143–153.

Niwas S., Tezkan B., Israil M., 2011: Aquifer hydraulic conductivity estimation from surface geoelectrical measurements for Krauthausen test site, Germany. Hydrogeol. J., **19**, 307–315.

Niwas S., Celik M., 2012: Equation estimation of porosity and hydraulic conductivity of Ruhrtal aquifer in Germany using near surface geophysics. J. Appl. Geophys., **84**, 77–85.

Orellana E., Mooney H. M., 1966: Master tables and curves for vertical electrical sounding over layered structures, interciencia, Madrid, Spain.

Pichgin N. I., Habibullaev I. K. H., 1985: Methodological recommendations in studying geo-tectonic conditions of vertical electrical soundings data with application of EC computer for solving hydrogeological and geoengineering problems. Tashkend (in Russian).

Ponikarov V. P., 1964: The Geological Map of Syria, 1:200000 and Explanatory Notes. Syrian Arab Republic, Ministry of Industry, Department of Geological and Mineral Research, Damascus, Syria.

Purvance D., Andricevic R., 2000: Geoelectrical characterization of the hydraulic conductivity field and its spatial structure at variable scales. Water Resour. Res., **36**, 10, 2915–2924.

Skinner D., Heinson G., 2004: A comparison of electrical and electromagnetic methods for the detection of hydraulic pathways in a fractured rock aquifer, Clare Valley, South Australia. Hydrogeol. J., **2**. 576–590.

Soumi G., 1991: Supplemental Irrigation Systems of the Syrian Arab Republic (SAR). In: Proceeding of the Workshop on Regional Consultation on Supplemental Irrigation. ICARDA and FAO, 7–9 December 1987, Rabat, Morocco. Kluwer Academic Publishers, Dordrecht, The Netherlands, pp. 497–511.

Soupios P., Kouli M., Vallianatos F., Vafidis A., Stavroulakis G., 2007: Estimation of aquifer hydraulic parameters from surficial geophysical methods: a case study of Keritis Basin in Crete. J. Hydrol., **338**, 122–131.

Takhur J. K., 2016: Hydrogeological modelling for improving groundwater monitoring network and strategies. Applied Water Sciences, 1–18.

Taylor R. W., Fleming A. H., 1988: Characterizing jointed systems by azimuthal resistivity surveys. Ground Water, **26**, 464–474.

Tizro A. T., Kostantanous S., Voudouris K., Salehzade M., Mashayekhi H., 2010: Hydrogeological framework and estimation of aquifer hydraulic parameters using geoelectrical data: a case study from West Iran. Hydrogeology Journal, **18**, 917–929.

Tizro A. T., Voudouris K., Basami Y., 2012: Estimation of porosity and specific yield by application of geoelectrical method – A case study in western Iran. Journal of Hydrology, **454–455**, 160–172.

Wolfahrt R., 1966: Zur Hydrologie vor Syrien. Bundesanstalt für Bodenforschung und den Geologischen Landesämtern der Bundesrepublik Deutschland (in German).

Wolfahrt R., 1967: Geologie von Syrien und Lebanon, Gebrüder Bornträger, Berlin-Nikolasee (in German).

Zohdy A. A. R., 1989: A new method for the automatic interpretation of Schlumberger and Wenner sounding curves. Geophysics, **54**, 245–253.

Zohdy A. A. R., Bisdorf R. J., 1989: Schlumberger Sounding Data Processing and Interpretation Program, US Geological Survey, Denver.

sciendo

Contributions to Geophysics and Geodesy Vol. 49/1, 2019 (67–107)

Evidences of the charge fundamental asymmetry

[The origin of the rotating normal body's magnetic field and the biggest mysteries of the cosmology]

Mohsen LUTEPHY

The faculty of science, Azad University, south Tehran branch, Iran
e-mail: lutephy@gmail.com
website: https://www.researchgate.net/profile/Mohsen_Lutephy

Abstract: There is an infinitesimal small non polarizable electric inertial charge in the individual atoms or in a number neutral matter included to equal number of the electrons and protons. We refer to the pure calculations verified by the experimental laboratorial results, also planetary phenomena and cosmic observations. This inertial electric charge is origin of a part of the measurable magnetic field in addition to self-consistent dynamo, together as complementary origins to generate very complex magnetism of the celestial bodies. Ultimately we refer to the null results of the test experiments for the spinning bodies magnetic field and we see that neither used bodies in the experiments have been number neutral (no equal number of the electrons and protons), nor the simple formula of the Patrick Blackett is accurate in detail. But we have extracted a new formula in agreement for all spinning bodies magnetic fields, in agreement with both terrestrial and cosmic bodies. We verify the effect of electric charge asymmetry in expanding universe and acceleration of the universe expansion and anisotropy of cosmic microwave background and singularity paradox and solar wind and acceleration of solar wind and corona high temperature puzzle as an equilibrium between the gravity and antigravity and mysterious heat generation of the Sun and planets interiors and missing neutrino and the comets plasma tail outward direction and pendulums mysterious precessions and some other mysteries phenomena too.

Key words: electric charge asymmetry, celestial magnetic field, Nipher experiment, expanding universe, corona, excess charge, microwave background, solar wind, antigravity, missing neutrino, pendulums mysterious precession, Podkletnov effect

1. Introduction

Albert Einstein considered the origin of the Earth's magnetic field, one of the five most important unsolved problems in the physics and generally the

doi: 10.2478/congeo-2019-0005

origin of the celestial bodies magnetic fields is a long time mystery of the science.

It has been developed, the gravity driven magnetic field by relevant scientists to answer to the celestial bodies magnetic fields. Arthur Schuster (*Schuster, 1912*) initiated such a hypothesis on the base of the gravitational magnetism and Patrick Blackett (*Blackett, 1947*) formulized it in a simple correlation between magnetic moment and angular momentum of the celestial bodies. Then these theories went to the laboratories to test experimentally.

Blackett simple equation (*Blackett, 1947*) was showing that his golden rotating cylinder should show a magnetic moment greater than 10^{-9} Gauss. But the experiments did not result such an answer (*Wilson, 1923*) and Patrick Blackett (*Blackett, 1952*) announced, the failure of these gravitational magnetism theories. After negative result of the Gravitational magnetism theories, the self-consistent dynamo was developing by scientists, similar to the Einstein relativity that after null result of the Michelson-Morely experiments (*Michelson and Morely, 1887*), the Einstein relativity was growing rapidly.

The second half of the twentieth century, the dynamo theory, describing the process through which a rotating, convecting, and electrically conducting fluid acts to maintain a magnetic field, was used to explain how hot iron in the outer core of the Earth creates a magnetosphere.

Of course there are some controversial evidences opposite with self-consistent Dynamo. For example, a new article by Gregory Ryskin (*Ryskin, 2009*), is showing that the Earth magnetic field origin should be revisited. In Ryskin's paper the correlation of the secular variation of the geomagnetic field and oceans flows is opposite with the before concept of the core fluids which was theorized reasonable for self-consistent Dynamo.

Thomas Cowling's anti-dynamo theorem (*Cowling, 1934*) states that no axisymmetric magnetic field can be maintained through a self-sustaining dynamo action by an axially symmetric current and he proved that a dynamo can't exist if both flows and magnetic field are axisymmetric about the same axis. Some more of these anti-dynamo theorems are given in *Moffatt (1978)* that purely toroidal motion can't produce a dynamo, and neither can purely planar motion. However, a mix of stationary magnetic field and dynamo, strongly can resolve the paradoxes as the wave and particle complementary

did resolve many paradoxes in the physics.

There are also thermal paradoxes for self-consistent dynamo theory for example wide spread paleomagnetic evidence for a Geodynamo (*Tarduno et al., 2010*) creates the new core paradox as a puzzle that what powered the Geodynamo prior to inner core nucleation and too as noted by Denis Andrault (*Andrault et al., 2016*) that:

"the Earth is a thermal engine generating the fundamental processes of geomagnetic field, plate tectonics and volcanism. Large amounts of heat are permanently lost at the surface yielding the classic view of the deep Earth continuously cooling down."

And then we need a source to keep the Earth core temperature almost constant along the billion years and in reality the temperature constancy of the core is needed until the Geodynamo to be stable historically to resolve the thermal paradox.

The magnetic field is correlated with all spinning cosmic bodies especially about the neutron stars. The generation of extreme magnetic field in neutron stars is completely ambiguity in self-consistent dynamo mechanism and finding a dynamo region in so compressed neutron regions in these stars is almost impossible. For example, PSR J1748-246ad is rotating at the surface around the 25% of the light speed and for such a neutron star, assuming a self-consistent dynamo is almost impossible.

It is clear that we should find a next way for magnetic field generation on the neutron stars. However, it is visible that in the Sun like stars, the dynamo is working well.

It is time now to revisit the theories and never we don't allow to be sure about anything and the history of science is showing that complete sure about the scientific subjects is error. For that after a passing time, some things new are opposing the before ideas we have been completely sure about them and in reality the increase of the paradoxes is the sign for failure of the theories.

It is almost hard to exclude the theory of the self-consistent dynamo and dynamo theory may be actually in agreement with some celestial bodies. But it is too visible that the spinning bodies also have different origin to generate magnetic field.

Here in this paper we return to the origin of the celestial bodies magnetic field and we want to show why the experiments didn't result magnetic field

for rotating disks in the laboratories.

We have obtained here a universal formula for spinning bodies magnetic field completely in agreement with small and big bodies, whether terrestrial or cosmic and it is all on the base of the electromagnetism not relevant to any type of the gravitational theories, however the formula is very near in shape to the Patrick Blackett simple formula.

We find that the self-consistent dynamo is not the main origin of the planets magnetic field presently whereas that it is yet a compatible theory for some secular variations in the planets magnetic field. But the self-consistent dynamo is yet compatible mainly in some types of the celestial bodies. In reality on the base of the observations we find that both the self-consistent dynamo and stationary magnetic field of the rotating bodies is working in the celestial bodies as the complementary mechanism with different percentages in different bodies.

In addition to the magnetic field interpretations we have resulted here that the electric charge asymmetry is reason of some biggest problems in the cosmology and Earth and planetary sciences. For example, expanding universe and microwave background asymmetry (CMBR) and solar wind and its acceleration and corona puzzle and missing neutrons and comets plasma tail out ward direction and pendulums mysterious precessions and even the inflation theory and singularity paradox and many next mysterious phenomena.

2. Electric charge asymmetry

For a very short description of the subject we refer here to some sentences noted by Sujan Sengupta (*Sengupta, 2000*) that:
"Almost forty years ago Lyttleton and Bondi (1959) suggested that if the electron and proton charge differed by a part in 10^{18}, it could account for the expansion of the Universe. Consequently, interest developed on the issue of the possibility of a tiny charge asymmetry of matter in particular and the Universe in general. The subject gained general acceptance by the scientific community after the experiment of Hillas and Cranshaw (1959). There were several experiments to detect charge asymmetry in matter. However, all these experiments put definite upper limits on the charge asymmetry

which are much lower than that required by Lyttleton and Bondi (1959). It is worth mentioning that the strength of the electromagnetic interaction is 10^{39} times stronger than the gravitational interaction and so any tiny electric charge asymmetry could have profound consequence. Considering the anisotropy in the cosmic microwave background radiation (CMBR). Sengupta and Pal (1996) found that the present excess number density of particles with charge e over the particles of opposite and equal charge must be less than 8.5×10^{26} cm^{-3}."

And as noted at (*Sengupta and Pal, 1996*) that:

"We point out that an overall electric charge asymmetry in the universe will generate an anisotropy in the cosmic microwave background radiation (CMBR) via the Sach-Wolfe effect. From this, an upper limit on the electric charge asymmetry over a cosmological scale is found using the COBE data, which implies $\Delta TT \leq 10^{-4}$ for the CMBR. The same argument constrains the charge of degenerate neutrinos."

But we refer to a very precise experiment in Cavendish type series which enabling to report experimentally a repulsive force in comparison with attractive gravity. Francis E. Nipher in several consequent experiments (*Nipher, 1916, 1917, 1918, 1920*) applied electric induction into the metallic bodies as noted at *New York Times* (19 September 1917) that:

"If electricity can alter the gravitational attraction of the bodies used in my experiments," he said, "the same force can alter the Earth's attraction. If the negative electricity could be drawn from the Earth's surface, gravitational attraction suddenly would cease and the cohesion of the Earth's surface would be disastrously affected."

In a pamphlet issued (November 8, 1917), Prof. Nipher supplies experimental evidence that gravitational attraction can not only be suspended or nullified by the electrical current, but it actually can be transformed into "gravitational repulsion"! All during the summer of 1917, Prof. Nipher had his apparatus in almost continuous operation, and the experiments have been repeated time and again, always with the same result.

Before connecting any form of electric current to the modified Cavendish apparatus, Prof. Nipher took special precaution to carefully screen the moving element from any electrostatic or electromagnetic effects. His apparatus briefly consists of two large lead spheres ten inches in diameter, resting upon heavy sheets of hard rubber. Two small lead balls, each one inch in

diameter, were now suspended from two silk threads, stationed at the sides of the two large lead spheres, from which they were separated by a little distance. Moreover, the suspended balls were insulated elaborately from the large spheres by enclosing them first airtight in a long wooden box, which was also covered with tinned iron sheets as well as cardboard sheets and there was, furthermore, a metal shield between the box and the large metal spheres.

In his first experiments, Prof. Nipher applied a high tension current from a static machine to the large lead balls (Fig. 1).

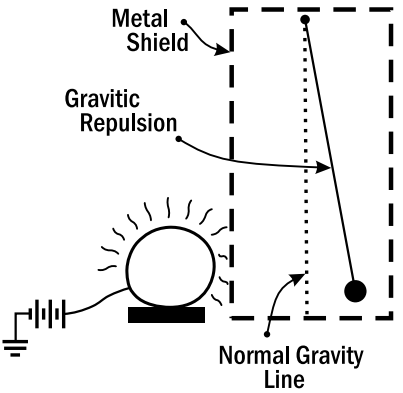

Fig. 1. Gravitational repulsion caused between large & small masses. Current on.

In one of these experiments the masses were "repelled" by a force nearly twice as great as the initial gravitational repulsion.

First, a direct current of 20 Amperes as sent through the two large masses, but no effect on the suspended masses could be detected. Next, an alternating current of 20 Amperes was sent through the two masses, with the result that the gravitational attraction was quickly reduced to zero, and not only that but in 15 to 20 minutes the small lead spheres had moved over one-half as much to the opposite direction as the distance they had been attracted originally towards the large masses. Thus gravitation had not only been completely nullified, but it was actually reversed.

In further experiments Prof. Nipher decided to check his results. To do this he replaced the large solid lead spheres with two metal boxes, each filled with loose cotton batting. These hollow boxes (having practically no mass)

rested upon insulators. The metal boxes were then charged in every way that the solid lead spheres had been, but not the slightest change in the position of the lead balls could be detected. This would seem to prove conclusively that the "repulsion" and "gravitational nullification" effects that he had produced when the solid balls were electrically charged were genuine and based undoubtedly on a true inter-atomic electrical reaction, and not upon any form of electrostatic or electromagnetic effects between the large and small masses.

If we consider simply the atoms to be electrified inertial as an electric charge asymmetry for electron and proton, it is clear that a mass included to the equal number of the electrons and protons will have an infinitesimal small inertial electric charge for infinitesimal small difference between the electric charge of the electron and proton. But on the base of the electric equilibrium, clearly along the time, the matter will be transferred to the electrical neutral body by absorption of the excess electrons involved in the matter between other particles (Fig. 2).

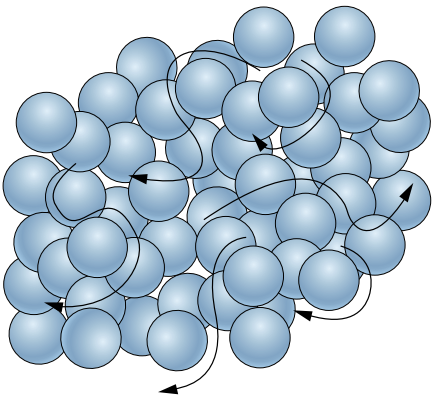

Fig. 2. Involving excess electrons in the matter.

This is a next magic of the quantum mechanics which even violates the Dirichlet principle or pigeonhole principle. Because that here we have N_p number of the protons and N_e number of the electrons and ultimately N_e number of the electrons are situated in the N_p number of the protons with $N_p < N_e$. So that ultimately we have an electrically neutral matter with different number of the electrons and protons and all electrons will be similar. However, the atoms individually are electrical, but additionally we have

electrically neutral matter and this is reason, why the rotation of the usual disks doesn't result the magnetic field whereas that fundamentally a matter included to the equal number of the electrons and protons should result the magnetic field. Then it is clear that the electrodynamics should be reformed and this modification has been realized by some scientists before, for example as noted at (*Lyttleton and Bondi, 1959*) that:
"If creation of matter, and also necessarily charge, is assumed, the Maxwell equations must be modified to avoid strict conservation. The appropriate modification is shown to involve additional terms in the current and charge-density equations proportional to the vector and scalar potentials."

Weber electrodynamics (*Assis and Silva, 2000*) is a modified electrodynamics and there are also some theories to modify electrodynamics. But for a natural modification of the electrodynamics on the base of the Mach's inertia principle or generally Mach's mechanics (*Mach, 1872, 1883, 1911, 1960*), we may refer to the book "MOED: the modification of electrodynamics by Mach's inertia principle" (*Lutephy, 2016*). MOED (Modification of Electro Dynamics) modifies electrodynamics by Mach's mechanics as the universal interconnection of the electric forces so that the Coulomb force is generated in fully relational dynamics (mere ordering upon actual objects) and the electric charge is depended to the large scale electric charge distribution and such a change in the electric charge of the fundamental particles by dependency to the universal electric potential energy is in reality a result of the Mach's mechanics as noted by *Sachs and Roy (2003)* that:
"We have seen that the qualities of localized matter, such as the inertial mass or electric charge of 'elementary particles', are really only measures of their interactions within a closed system of matter, between these entities and the rest of the system. Thus their values are dependent, numerically, on the rest of the matter of the closed system, of which they are elementary, inseparable constituents. Their masses and electric charges are then measures of coupling within a closed system, not intrinsic properties of 'things' of matter."

By the way when we have a body included to equal number of the electrons and protons, this body has inertial electric charge and to visit this inertial charged body in the laboratory we need to exclude the excess electrons by physical ways. For example, it was used AC voltage into the metallic bodies by Francis E. Nipher in his experiments and it was observed an

electric repulsive force between metallic bodies. By AC voltage, the excess electrons are assumed to be freed from atomic links transmitted to the surface of the metallic ball to appear the electric repulsive force between these bodies, where the Faraday cage was shielding in the Nipher apparatus, the electric effect of the freed electrons distributed on the surface whereas that Faraday cage not enabling to shield the effect of the non-polarizable inertial electric charge.

This non polarizable inertial charge is not affecting on the polarizable charge means not affecting on the individual free electric charges. This character is the most important feature of the inertial non polarizable electric charges, reasoning to appear mysterious phenomena in the solar system and the cosmos. Clearly this inertial non polarizable electric charge is not possible to be shielded by Faraday cage whereas that Faraday cage shields the polarizable electric charge. Of course it is possible that non-interaction of the atomic level electric charge with free electric charges to be dependent also to the quantum effect of the scale. Because that the inertial electric charge is very tiny electric charge, but free charges are very larger and then probably such a huge difference in the scale of these electric charges reasoning to avoid from interaction of them and such a probable scale dependency of the interaction can be treated by scientists in the future.

Referring to the Nipher experiments, results that this repulsive force between metallic spheres in actual size is at least two times greater than the attractive gravity as mentioned above and then we have for a pair of linked $e-p$ (electron-proton) that:

$$k\frac{(q^{\&}_{e-p})^2}{r^2} = 2\frac{Gm^2_{e-p}}{r^2}\,, \tag{1}$$

$$q^{\&}_{e-p} = \sqrt{\frac{2G}{k}\, m_{e-p}}\,, \tag{2}$$

where $q^{\&}_{e-p}$ is inertial electric charge of a pair of linked electron-proton and m_{e-p} is the mass of each pair.

Then a pair of linked electron-proton have an inertial electric charge at least equal to:

$$q^{\&}_{e-p} \cong 2 \times 10^{-37} C\,. \tag{3}$$

This inertial electric charge is very smaller than the electric charge of an electron. But as we see it is possible to detect by precise measurements in the laboratory.

By the way on the base of the electric charge asymmetry calculated by Nipher experiments analysis, the additional force between two normal bodies (equal number of electrons and protons) m and m' is addition of the inertial electric force and pure gravity. Then in actual sizes based on the Nipher experiments for two normal masses m and m' in a distance R, we have an additional repulsive force F that:

$$F = -G\,\frac{m\,m'}{R^2}\,. \tag{4}$$

Now consider schematically a spherical universe with constant density. The acceleration of the universe on a point in radii r because of shell theorem is:

$$a_r = \frac{\mathrm{d}v}{\mathrm{d}t} \to -\frac{G\int_0^r \mathrm{d}m}{r^2}\,dr = v\mathrm{d}v\,, \tag{5}$$

and because that $\int_0^r \mathrm{d}m = \rho_U V_r = \rho_U \frac{4}{3}\pi r^3$ and substituting this equation in the Eq. (5) implies:

$$-\frac{4}{3}\pi G\rho_U r\mathrm{d}r = v\mathrm{d}v\,. \tag{6}$$

Universe is expanding from an initial small radii and then by integrating from zero it is resulted by Nipher experiments that:

$$v = \frac{1}{\sqrt{2}}\,Hr \,\Big|\, H = \sqrt{\frac{8}{3}\pi G\rho_U}\ . \tag{7}$$

To obtain the Hubble law $v = Hr$ by the cosmic bodies charge asymmetry we need to reform the Eq. (2) as:

$$q^{\&}_{e-p} = \sqrt{\frac{3G}{k}\,m_{e-p}}\,, \tag{8}$$

and then the amplitude of the charge asymmetry calculated by Hubble expansion is:

$$q_{e-p}^{\&} = 2.44 \times 10^{-37} C\,. \tag{9}$$

Then referring to the Hubble constant is showing that the electric charge asymmetry obtained by universe expansion should be 1.22 times larger than that of measured by Nipher experiments as a reason to understand that the Nipher balls have not been completely ideal included to the perfect equal number of electrons and protons and this is natural because that the actual size is ever lesser than the ideal and we understand that the normal part of Nipher metallic spheres has been 80% that of the cosmic matter.

Nipher type experiments is a way to reveal the numerically neutral bodies with equal number of electrons and protons. But, there are other ways too. For example, using heat to exclude excess electrons from their linked level and there are treats in the cosmic and planetary phenomenology too. In 1993, the Nobel Prize in Physics was awarded to Russell Hulse and Joseph Taylor of Princeton University for their 1974 discovery of a pulsar, designated PSR1913+16, in a binary system, in orbit with another star around a common centre of mass. This binary pulsar was under study by Sujan Sengupta (*Sengupta, 2000*) as an example to reveal the electron-proton charge asymmetry. As noted by *Sengupta (2000)* that:

"A binary stellar system loses its orbital rotational energy by the emission of gravity wave. If there exists a charge asymmetry between electron and proton, then the system would also lose its orbital rotational energy due to electric dipole radiation provided the masses of the two objects are not exactly equal."

And too that:

"Considering this fact and adopting the observed data of the binary pulsar PSR B1913+16 an upper bound on the electric charge asymmetry between electron and proton is obtained which is more stringent than the existing bounds."

Referring to the calculations of the Sujan Sengupta it is visible a bound amplitude for charge asymmetry as

$$\left|q_{e-p}^{\&}\right| \leq 3.2 \times 10^{-20} e\,. \tag{10}$$

This amplitude is almost 2% that of calculated at Eq. (9). But these different amplitudes are not opposing each other because that a complete number neutral body that $N_e = N_P$, is an ideal body and actually the celestial bodies are not completely normal. It is not hard to conceive that the

stars are neutralized by electric equilibrium and the Sun strongly is now not a perfect number neutral body suppose main of the Sun's mass has been neutralized electrically up to now. But the percentage of the neutralization is different in different stars. Interestingly we will see that the magnetic field of the Sun is showing the same about 2% normal body visible for PSR B1913+16.

The absorption of the excess electrons is a mechanism that it is reason to separate the star's interior to the two different main parts which a part is electrically neutralized part and the next part is numerically neutral or normal. How much the age of the star to be rather, its electric neutralization is rather too. About the Sun the evidences are showing that the normal part exists at the convection zone. The absorption of the electrons by normal matter will transfer it to a pure gravity shape.

About the PSR B1913+16 also it was resulted that just 2% that of this system is normal as a source of electric dipole radiation responsible to lose the orbital energy and this is in agreement with observations for neutron stars' magnetic field which with almost constant mass and constant spinning rate, the neutron stars have widely different amplitudes of the magnetic fields. In reality, neutrons in normal body are under the electric repulsive force and then stability of the neutrons in the neutron stars needs intermediate exchange particles for example electrons, similar to the system of atoms nucleons. Then neutron stars too are being neutralized electrically by exchange particles and it is mistake to consider all the neutron stars as a completely normal body.

The heat generation in the planets has been a long time mystery and newly *Andrault et al. (2016)* claiming that lunar tidal effect is responsible to keep the temperature almost in a constant size in the planets interior whereas that such a mechanism is so far to accept. It is clear that the planets interior should be cooled along the billion years whereas that experiments are showing that temperature has been almost constant and this is a paradox.

The force between atoms is addition of the gravity and antigravity in a normal body. When this normal body is neutralized electrically then just remains gravity. By Eq. (8) the antigravity is three times stronger than the gravity and then in electrically neutralization of a normal body we have a heat generation as great as two times of the total gravitational potential

energy of the body. Now if we consider a normal sphere with mass M and radius R, then by definition of the total potential energy of this sphere we have a total heat generation as

$$H = 2G\,\frac{M^2}{R}\,. \tag{11}$$

If we consider the Earth initially as a normal body transferring gradually to the electrically neutral body among the time, then total heat generation of the Earth by Eq. (11) is 10^{33} J and this is in agreement with billion years heat generation of the Earth in average size of 4×10^{15} W. In the planets the mechanism of this phenomenon is that the absorption of the excess electrons causes ever to create heat at the bottom of the outer core which it is a normal shell. This mechanism is reason to increase ever the inner core boundary by addition of the outer core to inner core because of absorption of the excess electrons at the bottom of the outer core. This heat generation will be continued until that all the outer core be transferred to the shape of the inner core and probably this is what it has been happened for Mars which has tiny abnormal magnetic field. Inner core is electrically neutralized by excess electrons and then the additional inter-atomic force is just gravity in the inner core whereas that outer core inter-atomic force is antigravity two times as great as the gravity and this phenomenon causes to condensate the inner core highly in comparison with the outer core and probably inner core solidity.

Scientifically measurements and calculation by Raymond Davis (*Davis, 1964*) and John Bahcall (*Bahcall, 1964*) on the solar heat generation by fusion reaction was showing that the generated heat is 1/3 rather we wait from the fusion reaction in the Sun. The assumed energy of the fusion reaction is 1/3 rather than we observe from accounting the neutrinos. The discrepancy between the number of predicted neutrinos and the number Raymond Davis measured became known as "The Solar Neutrino Problem" or in new popular contexts "The Mystery of the Missing Neutrinos".

But here we see that there is no missing neutrino and in addition to the fusion reaction we have a permanent generation of the heat by transformation of the repulsive force of the atoms to the gravitational force.

Calculations on the mass of the Sun's shells is showing agreement between anti gravitational heat generation in the Sun and heat needed to resolve the missing neutrino puzzle. Absorption of the cosmic electrons at

the Sun or rejection of the positive charges is reason to generate heat by transformation of antigravity to the gravity in the convection zone. In reality the convection zone is divided to the two shells similar to the planets core. A shell is inner convection zone included to the electrically neutral matter by linked excess electrons and an outer convection zone included to the normal matter with equal number of the electrons and protons. Then ever there is a heat generation at the boundary between the inner convection zone and outer convection zone and gradually the outer convection zone is transferred to the inner convection zone similar to the transformation of the outer core to the inner core in the terrestrial planets. The heat generation by electro antigravity at the bottom of the outer convection zone causes to appear convectional cells over the outer convection zone as a source for granulation in the Sun's surface. Also this convection in the outer convection zone as a rotating shell is reasonable to create self-consistent dynamo.

But in the Sun's radiation zone boundary we have a next heat generation by transformation of the antigravity to the gravity. We refer to the reality that the electrically neutralized matter by excess electrons are divided to the two shapes. When we have a usual matter electrically neutralized by excess electrons then all electrons are similar involving between protons with no difference. Then all electrons are linked to the protons and then excess electrons are non-polarizable. But when the temperature is rising highly larger than a critical temperature, the excess electrons become polarizable and this means that matter want to stay normal with equal number of linked electrons and protons in high temperature. Then if we use from two high temperature disks in an experiment (rather than critical temperature) and shielding by a Faraday cage then against the usual matter we will observe antigravity instead gravity similar to what it was visited at the Nipher experiments. These unlinked excess electrons in high temperature matter neutralizes electrically the matter in the absence of shielding effect just in large scale. But we should notice that strongly the nearby links are yet affecting together by antigravity for that just in this condition, the excess electrons are polarizable against the linked excess electrons.

Then for each matter there is a critical temperature as a transition point between linked excess electrons and unlinked excess electrons. It is now soon to discuss this topic accurately and it needs to be continued by scientists in detail.

Unlinked excess electrons are appeared when the temperature is higher than the critical temperature. But when the temperature comes down then unlinked excess electrons are transferred to the linked level and generating heat.

In reality the Sun radiation zone is included to the hot plasma with temperature rather than the critical temperature included to the unlinked excess electrons whereas that inner convection zone is a low temperate plasma included to the linked excess electrons and normal plasma exist in the outer convection zone. This is reason that the temperature at the radiation zone boundary to be ever constant for that by cooling plasma at the boundary of the radiation zone along the time, unlinked excess electrons are transferred to the linked level in the bottom of the convection zone and then generation of heat at the boundary of the radiation zone avoids from decrease of the temperature at this boundary as a reason for constancy of the temperature at the boundary of radiation zone and as a reason to control the Sun's heat at a constant rate naturally as a natural thermostat. It is manifest that constancy of the Sun radiation is important for life in the Earth.

The heat generation at the radiation zone boundary as a kinematic energy can also generate convective overshoot as a phenomenon of convection carrying material beyond an unstable region of tachocline (*Gilman, 2000*) into a stratified stable region over a thin shell between radiation zone and convection zone. This thin shell between radiation zone and convection zone is the same what scientists have named it overshooting zone which computers are showing a value of magnetic field for that (Fig. 3).

We may consider also a high temperature plasma disk covered by metallic screens, rotating in high speed to observe magnetic field generated by inertial electric charge of the hot plasma as a new discovery.

By the way, we see that the Sun like stars are not completely normal suppose mainly transferred to the electrically neutral matter by absorption of the excess electrons or excluding the positive nucleons. This mechanism is directly resulting the source for cosmic rays. The electrically neutralization of the cosmos is accompanied with generation of the cosmic rays as a source of cosmic sea of the ionized particles, reasoning to generate shielding effect for unlinked excess electrons in high temperature plasma in large scale systems like the stars' interior.

In reality the absorption of the excess electrons and rejection of the pos-

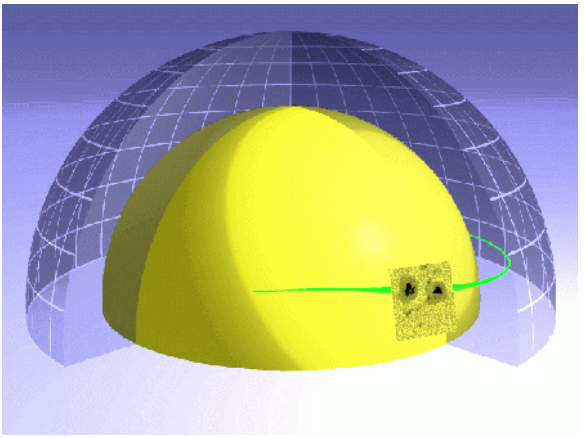

Fig. 3. Credit image: Peter Calligari, Fernando Moreno-Insertis and Manfred Schüssler. (The yellow hemisphere represents the bottom of the convection zone and the transparent one represents its surface. The green line is a bundle of magnetic field lines which has risen from the bottom of the convection zone up to the surface. The little superimposed picture with the two sunspots shows how the bundle of magnetic field lines appears to us when it emerges at the surface.)

itive ions are accompanied and then the total number of the positive cosmic rays is equal to the number of the excess electrons absorbed by matter in the stars and celestial bodies. We can say that concentration of the excess electrons in the stars is accompanied with distribution of positive nucleons in the cosmos and then all the stars and planets and galaxies are floating in a universal sea of the positive cosmic rays.

Generally, we have several clear items that:

a) In the universe the number of the electrons and protons is equal.

b) The number of electrons and protons is conserved if there is no creation of matter and disappearing of the matter.

c) The density of excess electrons is proportional with mean density of the baryonic matter.

d) The density of the cosmic ray is more where the point is farer from the massive areas (Voids).

And then it is appeared a formula for constancy of addition of the excess electrons density and cosmic ray density as:

$$\rho_{excess} + \rho_{sea} = k\,. \tag{12}$$

By this formula we find that the vacuum distance between the galaxies is the space with more density of the cosmic ray sea and this means that the large scale vacuum between the galaxies cause to shield highly polarizable electric charges. on the other hand, referring to the Poisson equation of screening effect as the dielectric generated by fluid medium (*Kamrin and Koval, 2012*), the distance between the galaxies is a factor to increase the screening effect and then the shielding effect is increasing between galaxies. Ultimately we understand that there is a transition radius which in that radii, the gravity is transferred to the antigravity by increase of the shielding effect for unlinked excess electrons in the stars as a reason for gravity at galaxy scale and antigravity at inter galactic scales and larger scales responsible for universe expansion.

3. The origin of the rotating normal body's magnetic field and cosmic big mysteries

There are several theories about non-electrical spinning bodies magnetism initiated by Arthur Schuster (*Schuster, 1912*). On the same process, Patrick Blackett (*Blackett, 1947*) on the planetary observations did result a phenomenological formula for magnetic moment of non-electrical rotating bodies. His formula went to test in the laboratory. But the experiments were not success to show the predicted magnetic field. For example, *Wilson (1923)* reported null result and *Blackett (1947)* experiment didn't show any result for rotating gold cylinder, however the accuracy of the devices was adequate. But here we refer to a reality that each body, whether terrestrial or cosmic is divided to the two parts:

a) Electrically neutral part included to the excess electrons.

b) Number neutral or normal part included to the equal number of the electrons and protons.

Fundamental charge asymmetry is reason that each normal spinning body does generate a magnetic field. For a spherical spinning normal body by assuming a charge density ρ_e, from definition of the magnetic field at poles and surface we have:

$$B = \frac{8\pi k}{3c^2}\,\frac{1}{R^3}\,\omega \int_0^R \rho_e r^4 \mathrm{d}r\,. \tag{13}$$

So that k is electric constant and c is light speed and ω is angular velocity and R is radius and r is distance from the center.

By Eq. (8), the charge density is transferred to the mass density as:

$$\rho_e = \rho\sqrt{\frac{3G}{k}}\,. \tag{14}$$

Substituting this equation in the Eq. (13) results a magnetic field at poles of a spherical normal rotating body that:

$$B = \frac{8\pi}{3c^2}\,\sqrt{3Gk}\,\frac{\omega}{R^3}\int_0^R \rho r^4 \mathrm{d}r\,. \tag{15}$$

Then mathematically on the definition of angular momentum L and the moment of inertia I we obtain by Eq. (13) that:

$$BR^3 = \frac{2}{3c^2}\,\sqrt{3Gk}\;\omega I\,, \tag{16}$$

$$BR^3 = \frac{2}{3c^2}\,\sqrt{3Gk}\;L\,. \tag{17}$$

By relation of the magnetic field B to the magnetic moment p that $4\pi BR^3 = 2\mu_0 p$ we obtain by Eq. (17) that:

$$p = \frac{\sqrt{G}}{\sqrt{3}\sqrt{k}}\,. \tag{18}$$

This is similar to the Patrick Blackett formula, both in shape and size.

This equation for magnetic moment of rotating normal body is adequate to show magnetic moment in a precise experiment similar to the Blackett experiments which it was adequate to show a magnetic field larger than 10^{-13} T.

But the measurements were not success to show magnetic field for example null result reported by *Blackett (1952)* and too reported null result by *Wilson (1923)*. But here in this paper we see that there is a big error in

the measurements about the using rotating bodies. The bodies have been electrically neutral and electrically neutral body in their theories of Gravitational magnetism should result magnetic field whereas that gravitational magnetism doesn't work right suppose magnetic field is ultimately possible to be generated by electric charge torques and the electric charge asymmetry reasons the magnetic field from rotation of normal bodies included to equal number of electrons and protons.

Simple bodies in the Earth surface are all electrically neutralized by excess electrons and they are not normal and then using these bodies in the experiments to detect magnetic field by their spinning will not generate magnetic field.

Initially it needs to exclude the excess electrons and this rejection or shielding requires some especial techniques and possibly the scientists in the future will discover several ways. But referring to the Nipher experiments is showing that applying AC voltage in the same manner the Nipher used, is suitable for excess electrons excluding. Rotating disk should be under a suitable level of AC voltage and such a rotating disk can show a magnetic field in the experiments when excited excess electrons are shielded. Strongly by such a rotating metallic disk in Nipher type experiments, we will observe a value of magnetic field as a verification for charge fundamental asymmetry.

Similar measurement has been applied before by Eugene Podkletnov (*Podkletnov and Nieminen, 1992; Podkletnov and Vuorinen, 1996; Podkletnov, 1997*). Eugene Podkletnov did use a super conducting rotating disk under high frequency AC voltage and it was visited a few percent loss of the weight for a body hanging above the disk. Podkletnov effect is now a mystery in the science. But we see here a similarity between Nipher outstanding sphere which was under AC voltage and Podkletnov rotating superconducting disk under AC voltage.

As it is visible in the Nipher experiments, the metallic sphere under the AC voltage is reason to induct electromagnetic effect to an electrically neutral metallic body inside the Faraday cage which it causes to transfer it to the side of a normal body. Such an electromagnetic induction is being observed between conductive cores of the planets when they are under Sun's magnetic field variation (*Lutephy, 2018*) reasoning external driven planetary origin of the geomagnetic jerks and LOD variations and relevant gravity

anomalies. Here in the Podkletnov effect we see that he has used from a superconducting rotating disk, inducting electromagnetically on the test mass above the disk, reasoning to transfer it to the side of a normal body including a percentage of non-polarizable inertial electric charge. Then it has been generated an electric inertial force between the Earth's outer core inertial charge and test mass used by Eugene Podkletnov, above the rotating superconducting disk which the total effect is reduced highly by the Earth's mantle. Of course it should be noted that dielectric effect of the Earth's mantle is working to decrease electro anti gravitational effect of the Earth's interior inertial electric charge.

The electric force between the Earth outer core and Podkletnov experiment test mass is possible to calculate purely by electric charge asymmetry. If we assume an ideal shape of the Podkletnov test mass as the perfect normal body and we render from dielectric effect of the mantle, then from the Eq. (9) we have an acceleration between the Earth's outer core and Podkletnov ideal test mass generated by Coulomb force that:

$$a = k\frac{M_{outer-core}\sqrt{\frac{3G}{k}}\, m_{disk}\sqrt{\frac{3G}{k}}}{(\sim R_{earth})^2\, m_{disk}} = -9.8\,(\mathrm{m/s^2})\,. \tag{19}$$

And this equation results an electro antigravity on the test mass exactly inverse of gravity as a complete buoyancy.

But we need to notice that the Earth's mantle is a very big dielectric which it causes to decrease highly the effect of the Earth's antigravity in the near Earth's surface on the normal bodies and also it is not clear how much Podkletnov measurement has been success to exclude excess electrons from the test mass transferring them to unlinked level. In fact, the equation (19) is showing that if the excess electrons to be completely excluded then in the absence of the earth big mantle dielectric we can prevail to the gravity and it seems this is what we observe in some versions of the flying saucers and we see that the ultimate power of the Podkletnov machine is perfect buoyancy of bodies at Earth surface.

Then in the Nipher type experiments if we use a method to measure the pendulums weight, when we apply AC voltage, it should be visited the loss of pendulums weight as a prediction of the electric charge asymmetry. However, the Earth's mantle decreases the effect highly, but when we have observed a weight loss in the Podkletnov experiment we should see it in this

assumed experiment too.

Nipher did not use any weight measurement and then for such a prediction in Cavendish type measurements it needs to repeat the measurement carefully again included to the weight measurements similar to measurements by electrically charged torsion pendulums used by Erwin Saxl (*Saxl, 1964*).

In reality the measurement of this buoyancy at the Earth surface is hard because of the Earth's mantle dielectric effect and it needs some measurements in high latitudes and in reality for direct effect of the Sun and planets on the test masses in the Earth surface because of the earth inertial system we need to exist from the Earth inertial boundary otherwise we will detect null result exactly similar to the null result of the Michelson-Morely experiments (*Michelson and Morely, 1887*). This subject is itself a different issue on specification of the Geodynamo we can continue it in the book "MOED" (*Lutephy, 2016*) which we have resolved logically the puzzles of the flat earth theory.

We can use from pendulums to measure the electro anti-gravitational effect of the Moon and Sun and planets on the Earth which can generate drag forces on these pendulums because of differential effect of the anti-gravity as a kind of tidal force. Then drag forces generate relevant precessions and variations in oscillation of the pendulums. Such a variation by electro anti-gravity in the pendulums precessions and periods is appeared in the eclipse times or syzygy effects where we have noticeable changes in the Earth electromagnetic features detected initially by Maurice Allais (*Allais, 1959a, 1959b)* as noted by Maurice Allais that:

"The observed effects are only seen when the pendulum is moving. They are not connected with the intensity of weight (gravimetry), but with the variation of weight in the space swept by the pendulum. Actually, while the movement of the plane of oscillation of the pendulum is inexplicable by the theory of gravitation, the deviations from the vertical are explained perfectly by that theory. The deviations from the vertical ... correspond to a static phenomenon, while m experiments correspond to a dynamic phenomenon."

Other scientists have tried in this way and yet the pendulum measurements are being continued. For example, Romanian physicists *Jeverdan et al. (1961, 1981)* did observe the Allais effect and the so-called *Jeverdan-Rusu-Antonescu effect* or *Jeverdan effect* as the change of oscillation period

of a pendulum during an eclipse. Also a result during the annular solar eclipse of September 22, 2006 has been presented by a Romanian team, with a quantization of the behavior of the paraconical pendulum (*Popescu and Olenici, 2007*).

Various other experiments using atomic clocks and gravimeters instead the pendulums also recorded significant anomalous gravitational effects (*Zhou et al., 1995; Mishra et al., 1997; Wang et al., 2000*). But gravimeters never detected any report comparable in size with the pendulums mysterious effect as a paradox about the incompatibility between the pendulums and gravimeters measurements. The direction of the pendulums effects is aligned with gravitational tidal forces but amplitudes are not in agreement with gravitational theories. But electro antigravity is not in proportion with total mass of the Sun and planets and Moon versus the gravity theories suppose dependent on the normal part of these celestial bodies and also dependent to the electrical screening effects. These effects of the Moon and Sun have been reported by Maurice Allais (*Allais, 1999*) as monthly and seasonal changes in the precession of the pendulums. Sun and Moon have electro anti-gravitational force on the Earth and then it will be appeared tidal effects on the pendulums and the tidal forces as the drag forces based on the Pippard precession (*Pippard, 1988*) generate such a phenomenon so that referring to the Pippard solution (*Pippard, 1988*) for spherically oscillating pendulum on the perturbations it is deduced that:

$$\Omega_p = \frac{a_{az}}{2A\omega} \cos(2\,(\theta - \Sigma_i))\,. \tag{20}$$

So that Σ is direction of the force on the azimuth plane and θ is direction of major axis A with angular velocity ω and a_{az} is component of acceleration on azimuth plane.

This equation results in each moment a precession for pendulums in relation with direction of the oscillation plane and direction of the drag force. By Pippard solution we observe that discrete forces occurring about the periods larger than a half of oscillation of the pendulums will generate angular velocity, no requirement to continuum force. Then discrete variations in the Normalization of the Earth by electromagnetic influences will cause to appear continuum precessions whereas that gravimeters are showing the effects just with continuum forces. Then we understand here what is difference between gravimeters and pendulums for showing mysterious effect of

the pendulums.

Even the solar wind mystery is strongly on this procedure and electric charge asymmetry will result directly the solar wind and even the solar wind acceleration. *Parker (1958)* theorized that since gravity weakens as distance from the Sun increases, the outer coronal atmosphere escapes supersonically into interstellar space. But it is clear that early models of the solar wind relied primarily on thermal energy to accelerate the material, alone cannot account for the high speed of solar wind. An additional unknown acceleration mechanism is required. In the late 1990s the Ultraviolet Coronal Spectrometer (UVCS) instrument on board the SOHO spacecraft observed the acceleration region of the fast solar wind emanating from the poles of the Sun and found that the wind accelerates much faster than can be accounted for by thermodynamic expansion alone. Parker's model predicted that the wind should make the transition to supersonic flow at an altitude of about 4 solar radii from the photosphere (surface); but the transition (or "sonic point") now appears to be much lower, perhaps only 1 solar radius above the photosphere, suggesting that some additional mechanism accelerates the solar wind away from the Sun. Then the acceleration of the solar wind is still not understood and cannot be fully explained by Parker's theory.

AC voltage application is not alone way to exclude excess electrons from links with protons suppose the heat is too a next way. The heat is reason to increase the entropy in the matter and cut the electron-proton links. Then after passing from a transition point and the bound of entropy, the excess electrons will be separated from atomic level links because that in high temperature, the atomic links tends to be in number equilibrium resulting equality of the electrons and protons numbers as a critical point to appear observable high temperature plasma's electrical features.

Then Plasma is in reality a normal matter included to the equal number of the electrons and protons and how much the temperature is higher, the number equality of the electrons with protons is nearer to perfect and expanding of the universe by electric charge asymmetry is itself a reason for the reality that our universe is mainly a plasma and expansion of the universe is appeared by plasma-plasma antigravity almost three times as great as the gravity.

When we consider the Sun as a hot plasma below the convection zone then it should be an electric acceleration from the Sun to each normal

plasma out of the Sun where the unlinked excess electrons are shielded by electric double layer of the Sun surface. Clearly the shielding effect of the Sun's surface double layer is in the scale of the solar system and the Sun's electric double layer is reason to appear antigravity between the Sun and a normal plasma in the inertia system of the solar system. We should notice that the Sun's surface double layer is working at the solar system scale to shield unlinked excess electrons and then the electric force between the Sun and a next star in the inner of the Milky way galaxy is pure gravity.

The Sun's core and radiation zone are almost 98% of Sun's mass and then ever exist a repulsive electric force by the Sun on the normal plasma out of the Sun surface. From Nipher experiments and calculation of Hubble law by electro antigravity it was resulted that the repulsive force of number neutral body is almost 3 times as great as the pure gravity and then additional force of gravity and antigravity results an acceleration on a normal test body equal to:

$$a_r = -2\frac{GM}{r^2}\,. \tag{21}$$

Now we can calculate the speed of plasma by Sun force ranging from Sun's surface (radius R) to a distance r so that:

$$v^2 = 2\int_R^r a_r \mathrm{d}r\,. \tag{22}$$

And by substituting Eq. (21) in the Eq. (22) we can calculate the speed of solar wind as (Fig. 4):

$$v^2 = -4GM\left(\frac{1}{R} - \frac{1}{r}\right)\,. \tag{23}$$

This is remembering the Parker diagrams of the solar wind speed (*Parker, 1965, 2001*) and the Sun's magnetic field is reason to appear spiral motion of the solar wind at the solar system. It is so excellent that the same force which generating the universe expansion is generating exactly solar wind at the same amplitude and this is a very strong confirmation for fundamental charge asymmetry.

This phenomenon may be used to build the plasma flying saucers or generally normal body flying saucers because we can use some devices included

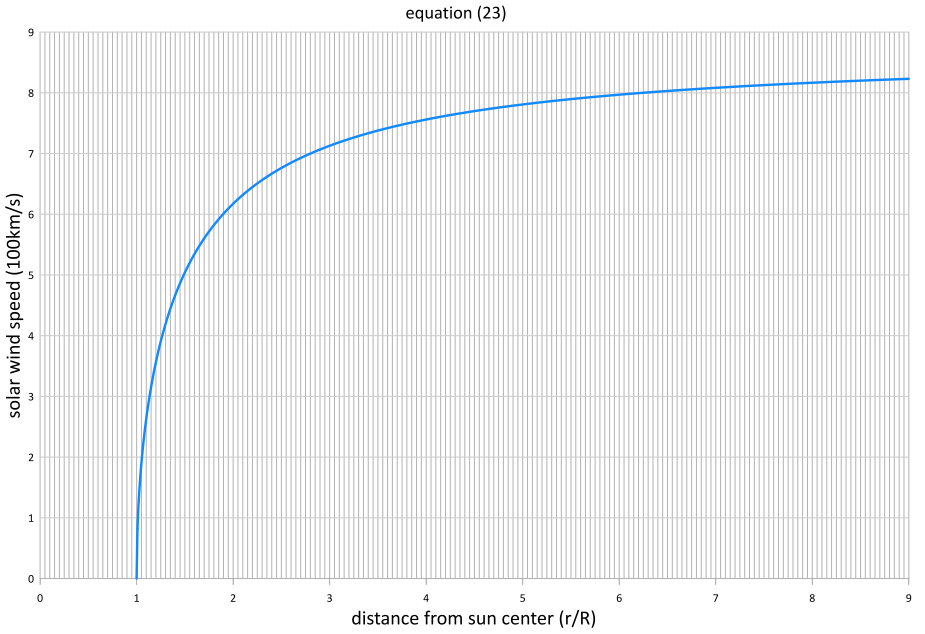

Fig. 4. Speed of plasma in the absence of the Sun's atmospheric dielectric.

to the normal body under the Sun electro anti-gravity similar to the solar wind. Then we will have very rapid interplanetary plasma flying saucers. Continuation of this especial issue will connect to the capacitors mysteries effect and also quantization and boundary dependency of the forces which we can continue it in the book "MOED": Modification of electro dynamics with Mach inertia principle and electro anti-gravity (*Lutephy, 2016*). There are important questions we have answered there for that if we want to continue here, the paper will inter to some new sections out of our target here. Of course there are other phenomena which we have not explained them here for example Sun flairs and Sun spots and coronal mass rejection (CMR) which for shortening the paper we have explained them in the book "MOED": Modification of electro dynamics with Mach inertia principle and electro anti-gravity.

Of course we should notice that the completeness of the normal body ($N_e = N_p$) is dependent to the temperature of the plasma means how much the temperature to be rather, the plasma is nearer to a perfect equality for

number of the electrons and protons. Also at the coronal radii, the repulsive force on the plasma becomes rapidly decreased reasoned by the Sun's atmospheric dielectric and this is resulting the corona as an equilibrium between the gravity and antigravity at the corona.

Too the solar wind is observed to exist in two states, termed the slow solar wind and the fast solar wind, though their differences extend well beyond their speeds. In near-Earth space, the slow solar wind is observed to have a velocity of 300–500 km/s, a temperature of $1.4–1.6 \times 10^6$ K and a composition that is a close match to the corona. By contrast, the fast solar wind has a typical velocity of 750 km/s, a temperature of 8×10^5 K and it nearly matches the composition of the Sun's photosphere (*Geiss, 1995*). As we see here, the high temperature solar wind is for slow solar wind in contrast with some theoretical alternatives for corona mystery.

On the other hand, the Sun has an atmosphere extended between surface and a radii r_t in the top of the chromosphere mainly included to the plasma and then we have atmospheric dielectric effect generated by Sun's atmosphere. Of course we should notice that the atmosphere of the Sun can't be a dielectric for Sun's inertial electric charge in usual case. But the Sun inertial electric charge is very big at surface position on the plasma (Earth mantle too is a dielectric for inertial charge because of its very width and dense structure). Such a very big amplitude of the electric force is enable to create a noticeable polarization at the Sun atmosphere and then resulting dielectric effect on the Sun's inertial electric force. Then atmosphere of the Sun causes to decrease the Sun total inertial charge to a value as effective inertial charge of the Sun. It is clear that the width of the atmosphere is reason to increase the dielectric effect (*Kamrin and Koval, 2012*) and then the Sun effective inertial charge is decreased by distance from the Sun surface until the radii r_t, above the Sun atmosphere.

In this radii r_t, the atmospheric dielectric effect arrives to its maximum size and there is a chirality in this radii for effective inertial electric charge of the Sun so that by increase of the distance above this chirality radii, the effective inertial electric charge begins to increase again asymptotically arriving to the Sun total inertial charge. Then we have a chirality radii r_t above the Sun atmosphere with minimum of Sun's effective inertial charge $q_t^{\&}$ there, because of maximum dielectric effect in this radii. Then above the chirality radii r_t we have suddenly increase of the Sun effective electric

charge asymptotically and below this transition radius we have exponentially increase of the Sun effective electric charge to a size equal to the Sun's total inertial charge at the Sun's surface. Then it is resulted that the asymptotic inertial electric charge of the Sun is equal with inertial electric charge below the atmosphere on the Sun's surface so that:

$$q_{sur}^{\&} = q_{asy}^{k} \,. \tag{24}$$

We need a function for effective charge of the Sun that:

1. Sun inertial electric charge on the surface to be equal with Sun total inertial charge.
2. Sun asymptotic inertial electric charge to be equal with Sun total inertial charge.
3. The Sun effective inertial charge to be minimum $q_t^{\&}$ at the chirality radii r_t.
4. Exponentially increase of the inertial charge below the chirality radii until surface.
5. Rapid increase of the Sun's inertial charge above chirality radii asymptotically.

What we should know here it is the variation of the electric permittivity by distance from the Sun surface which it causes to vary the Sun effective inertial charge by distance.

At the atmosphere of the Sun we have a plasma dielectric feature enable to decrease highly the Sun's inertial electric force similar to the simple electric screening effect and also for plasma dielectric generated from a fluid medium we can use from the solution of Poisson equation (*Kamrin and Koval, 2012*) in the fluid that it results an exponential function as screened Poisson equation that:

$$\varphi(r) = \frac{q}{4\pi\varepsilon_0 r} e^{-k_0 r} \,, \tag{25}$$

so that φ here is electric potential energy of the number charge in a large scale sphere and k_0 is assumed constant for cosmic plasma and in reality this function is the same Yukawa potential in the strong nuclear force.

A simple analysis shows that all functions with mentioned characters above, are near to the diagram generated by below function that:

$$q^{\&}_{sun} = q^{\&}_{t} + \frac{4^2}{\pi^2}\left(q^{\&}_{sur} - q^{\&}_{t}\right)\arctan^2\left(1 - \frac{r^n_t}{r^n}\right). \tag{26}$$

It is manifest that $q^{\&}_t$ is minimum inertial electric charge of the Sun at chirality radii because that the minimum inertial electric charge is occurred at this equation where the function arc tan is zero and clearly asymptotic inertial electric charge is equal to the Sun total inertial electric charge.

In the Eq. (26), the Sun's surface inertial charge should be equal to asymptotic inertial electric charge and the Eq. (26) is in agreement with exponential increase, below the chirality radii until to the radius R and too in agreement with rapid increase of the inertial electric charge above the chirality radii.

Geometrically the Eq. (26) is good approximate formula to show the Sun's effective inertial charge, above the Sun surface limited to the solar system and best fitting is showing that assumed power n in Eq. (26) is suitable to be considered at $n = 8$. Observationally it is good approximation to consider Sun's chirality radii r_t in proportion to the Sun's radii R as:

$$r_t/R = 1.08\,. \tag{27}$$

Substituting Eqs. (24) and (27) in the Eq. (26) and $n = 8$ and using the Sun's total inertial charge we result that

$$q^{\&}_{sur} = 5.92\, q^{\&}_{t}. \tag{28}$$

Then the Eq. (26) in unit (q_t, r_t) is

$$q^{\&}_{sun} = 1 + 8\arctan^2\left(1 - \frac{1}{r^8}\right). \tag{29}$$

And this Eq. (29) geometrically in units (r_t, q_t) is showing at Fig. 5.

By Eq. (8) we result for additional acceleration from the Sun on the plasma that:

$$a_r = \frac{GM}{r^2} - \frac{q^{\&}_{sun}}{r^2}\sqrt{3Gk}\,. \tag{30}$$

Mixing the atmosphere dielectric effect at Eq. (29) with this simple formula implies an approximately suitable function for Sun's force on the plasma acceleration that:

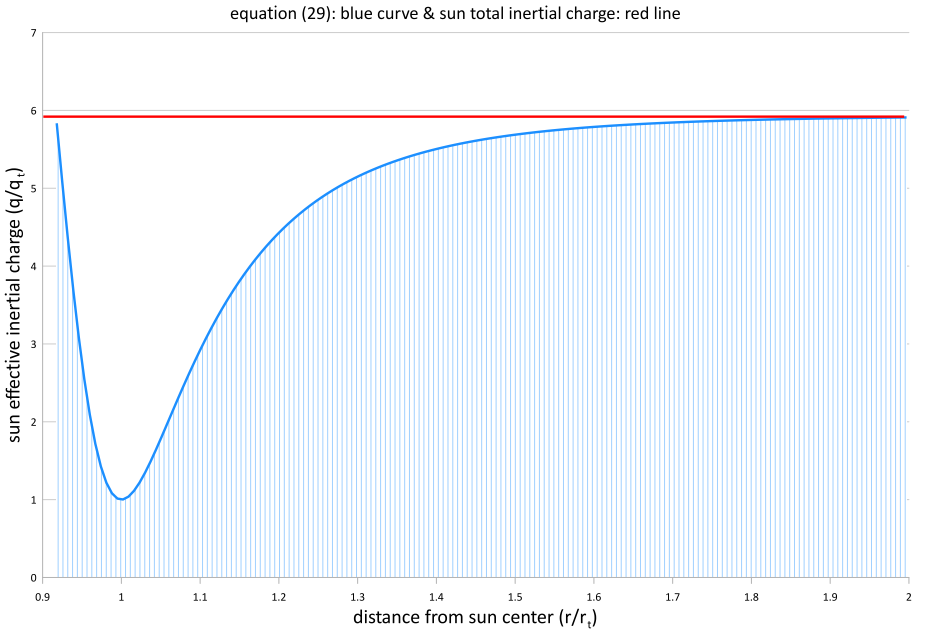

Fig. 5. Function of Sun effective inertial charge versus distance. The red line is the Sun's inertial charge in the absence of the dielectric effect of the Sun's atmosphere ($R = 0.927\, r_t$).

$$a_r = \left(\frac{GM}{r_t^2}\right)\left(\frac{r_t}{r}\right)^2\left[\frac{1}{2} - 4\arctan^2\left(1 - \left(\frac{r_t}{r}\right)^8\right)\right]. \tag{31}$$

This function is visible at Fig. 6.

Then we see that how much the beginning point of the solar wind is nearer to the Sun's surface, the speed of the solar wind will be asymptotically greater, as a strong verification for acceleration of the plasma by Sun's electric force. When the plasma is speeding from the coronal shell it is manifest that acceleration of the plasma is lower and proportionally the asymptotic speed is lesser. Then it should be appeared two level of the solar winds here so that one at the photosphere below the corona and next the plasma accelerating from the outer regions of the corona. Reason of this separation is that at coronal layer, the equilibrium between gravity and antigravity is zero and then the Sun has no electric force on the plasma at the corona center and this effect divides the solar wind to the fast and slow

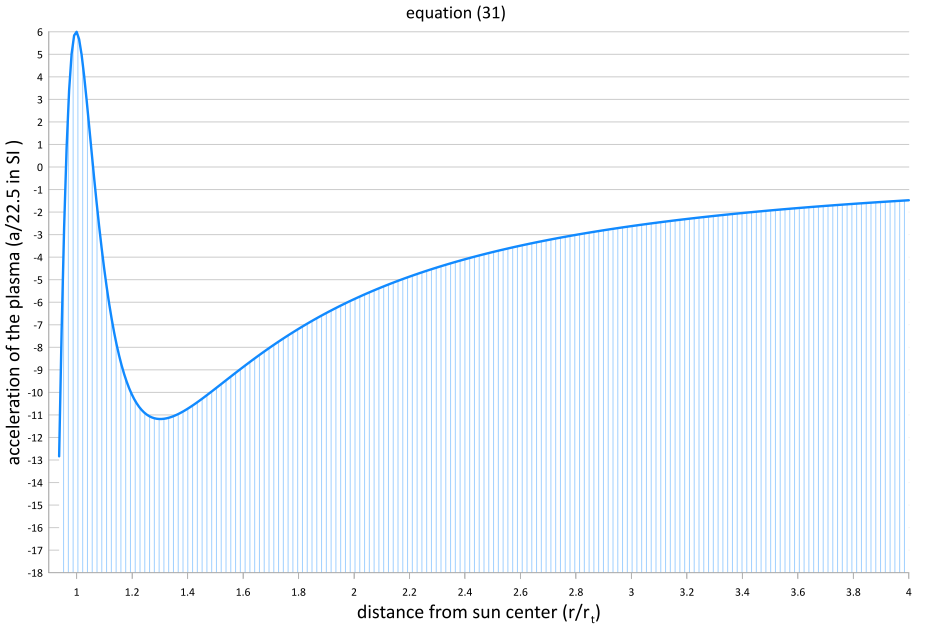

Fig. 6. Diagram of the Sun effective acceleration on the plasma in unit r_t and acceleration unit $22.5\,\mathrm{m/s^2}$.

levels completely compatible with the observations and records for solar wind.

On the other hand, for acceleration by Sun's inertial electric force on a normal plasma we have:

$$a_r = \begin{cases} +|r_c < r < r_t \\ 0\,|r_c \\ -|r\,(-a(r_t)) < r < r_c \end{cases} . \tag{32}$$

So that r_c is corona radius. Then plasma is pressed in a shell between maximum gravity and a radius with inverse size at antigravity which in the middle of this shell, the acceleration is zero as equilibrium point between gravity and antigravity.

We should notice that gravity is almost maximum at the chirality radius r_t because that at this radius we have minimum effective inertial charge.

Observations and mathematical calculations are showing that it is good approximation $d = R/10$ so that d is width of the assumed corona shell and for hydrostatic equilibrium it needs the pressure of the force on the shell to be equal with pressure of the coronal plasma inside the shell. According to the state equation $p = \rho kT/\mu$ we have:

$$\frac{\overline{m}a(r_t)}{4\pi r_c^2} = \frac{mkT}{4\pi r_c^2 \left|r(-a(r_t)) - r_t\right| \mu} \,. \tag{33}$$

So that $\overline{m}$ is average mass of the corona shell affected in each moment by force in assumed shell between maximum gravity and inverse antigravity and m is total mass inside the shell and then:

$$T = \frac{\mu}{k}\frac{\overline{m}}{m} = \left|r(-a(r_{ch})) - r_t\right| a(r_{ch}) \,. \tag{34}$$

In agreement with equation of the state we have $k = 8300$ and $\mu = 1.5$. In the maximum effect, the average size of the mass affected in each moment by force is equal with total mass and then:

$$T = 2 \times 10^6 \,\mathrm{K} \,. \tag{35}$$

And this is in agreement with observations as high temperature of the Sun's corona as a very strong verification for the reality that the corona is where the gravity and antigravity are in equilibrium in amplitudes and as a very clear verification, again for fundamental charge asymmetry (Fig. 7).

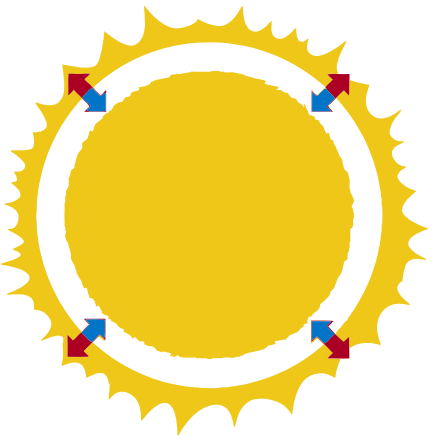

Fig. 7. Corona as equilibrium between gravity and antigravity.

Referring to the Parker diagrams of the solar wind shows a maximum amplitude of the asymptotic speed at 1000 m/s for solar wind at very high temperature whereas the calculation by electric charge asymmetry on the base of the Nipher experiments and modified in size by expanding universe is showing a maximum amplitude at 800 m/s calculated by Eq. (23). Then the calculated electric charge asymmetry by Hubble constant is showing that the normal matter in the universe is not perfect suppose universe matter should be 66% of a complete high temperature plasma. Then by electrically neutralization of the normal matter of the universe along the time and then decrease of the normal matter of the universe, ultimately the expansion of the universe will end and it will be started the contraction of the universe when the antigravity is diminished. Contraction of the universe will generate very condensed high temperature universe in a very small volume. Then the normalization of the matter will be increased again reasonable to start again the expansion of the universe consequently. This section is discussed in detail at the book "MOED" (*Lutephy, 2016*) and such a periodical acceleration of the universe is resolving too the paradox of the singularity in early universe.

The plasma tail of the comets is too under the effect of the Sun's electric force and then the comets plasma tail is directed to out radially. Biermann postulated that comets tail out ward direction happens because the Sun emits a steady of particles that pushes the comet's tail away (*Biermann, 1951*). Of course it seems that Paul Ahnert was the first to relate solar wind to comets tail direction based on the observations of the comet Whipple-Fedke. By the way, these theories are weak in comparison with the reality of electric repulsive force from the Sun on the plasma tail of the comets and reason is that the contact of the solar wind to comet's tails will ride away all material tails whereas here just the plasma tail is directed away.

Ultimately with return to the magnetic field of spinning bodies, the used body should be normal until to result inertial magnetic field and in the terrestrial planets, naturally we have a normal rotating shell as the outer core and this shell will generate inertial magnetic field manifestly.

For a neutron star which it be completely normal, calculations by Eq. (15) we obtain at the poles that:

$$B = 70\,\frac{R^2}{T}\,. \tag{36}$$

So that R is radius of neutron star and T is its period. This is completely in agreement with observations of the magnetic fields for magnetars which is a type of neutron star believed to have extremely powerful magnetic field $(10^{10} - 10^{11}\,T)$.

This is showing that the magnetars are completely normal neutron stars and short age of the magnetars verifies this reality for that a completely normal matter will be neutralized electrically rapidly and manifestly different percentages of the normalization in the neutron stars will generate wide range of the magnetic field for neutron stars completely in agreement with observations of the magnetic fields for neutron stars as visible above that the binary neutron star PSR1913+16 is just 2% that of a complete normal body.

But the planets magnetic fields are relevant to their conductive outer cores in terrestrial planets and the conductive cores of the Jovian planets, whether theoretical metallic hydrogen or probable metallic inner regions verified in the paper (*Lutephy, 2018*) reasonable for strong interplanetary electromagnetic inductions generating relevant geomagnetic jerks and LOD variations and gravity anomalies in the Earth position.

Inner cores of the planets are electrically neutral, reasoning to keep ever the outer cores as a normal shell. But inner core is tiny in comparison with outer core for all planets except probably at Mars and then as a good approximate formula for magnetic field of the terrestrial planets we can integrate over whole of the core whereas that inner core doesn't generate magnetic field. Then from Eq. (15) for magnetic field of the terrestrial planets we have:

$$B = \frac{8\pi}{3c^2}\sqrt{3Gk}\,\frac{\omega}{R^3}\int\limits_{outer-core} \rho r^4 \mathrm{d}r\,. \tag{37}$$

From planets magnetic field observed amplitudes embedding to Eq. (37) we obtain the radius of the electrically conductive core of these planets as the answers visible at the Fig. 8.

We observe that the percentage of the outer core radiuses of the giant planets per their radiuses is equal for all giant planets as a very strong confirmation for stationary magnetic field of spinning conductive regions in the interior of the planets and the calculated radiuses for CMB at the terrestrial planets is completely in agreement with observations. Then all

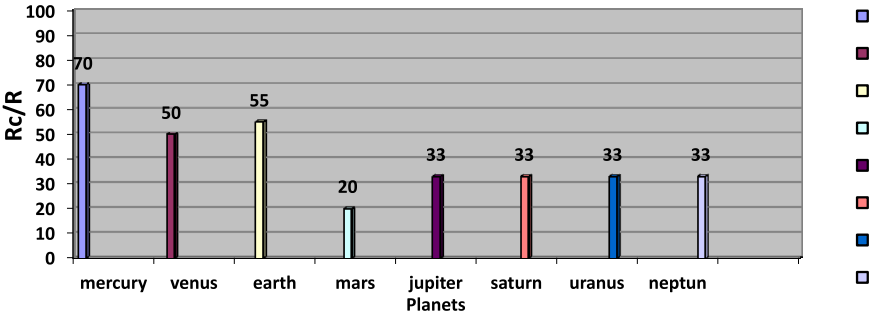

Fig. 8. Diagram of radius of conductive core of the planets per planets radius in % calculated by Eq. (37).

planets except Mars are in agreement with Eq. (37). As it was stated above, the Mars outer core may be transferred highly to the inner core. It is impossible that the radius of the outer core to be small because that the Mars has had a noticeable paleomagnetic field.

For Sun like stars means yellow dwarfs it was resulted above that outer convection zone is normal. Then for inertial magnetic field with assuming total convection zone as a normal shell we obtain that:

$$B = \frac{8\pi}{3c^2}\sqrt{3Gk}\,\frac{\omega}{R^3}\int\limits_{convection}\rho r^4 \mathrm{d}r\,. \tag{38}$$

According to Dalsgaard density profile of the Sun (*Christensen-Dalsgaard et al., 1996*), approximately we have:

$$\rho = 10\left(5\times 10^4\right)^{1-r/R}\,|r \le 0.95\,R\,. \tag{39}$$

This density profile is deviated about the surface, but it is a good approximation and by embedding Eq. (39) into Eq. (38) we obtain the Sun's inertial magnetic field if total convection zone was normal from below formula:

$$B = \frac{8\pi k\omega}{3c^2R^3}\sqrt{\frac{3G}{k}}\int\limits_{R_{con}}^{R}\left[10\left(5\times 10^4\right)^{1-r/R}\right] r^4 \mathrm{d}r\,. \tag{40}$$

So that R_{con} is bottom radii of conductive zone and by this equation we obtain an answer for Sun's magnetic field near to the observations for Sun's

magnetic field. But Sun's magnetic features especially its dipole reversal is showing that the self-consistent dynamo is working there and this reversal is not an historical report suppose it is doing cyclical in each eleven years presently. Then strongly dynamo is prevailing mechanism in the generation of the Sun's magnetic field and this is a real paradox here because that both of the mechanisms are in agreement whereas that it seems the dynamo is the main effect on the Sun's magnetic field.

We should notice that the convection zone is divided to the two shells which inner convection zone is electrically neutral low temperature plasma, not producing the magnetic field. Then stationary magnetic field will be generated just by rotation of the outer convection zone and this is a confirmation why in the Sun, the stationary magnetic field is weaker than that of what we measure it for total convection zone by Eq. (40) responsible to resolve the paradox.

On the other hand, we have used from Dalsgaard model (*Christensen-Dalsgaard et al., 1996*)) to calculate stationary magnetic field of the Sun generated by rotating convection zone as a spinning normal body and Dalsgaard model is based all on the pure gravity whereas that outer convection zone is being antigravity two times as great as the gravity, yet not electrically neutralized by excess electrons. Then clearly we need to revise the Sun's density profile and rewriting the density dependent equations with assuming that the outer convection zone is antigravity as a reason to decrease the density of the matter in the convection zone means the density in the outer convection zone is ever lesser than what calculated by Dalsgaard model. Then real size of the density profile will result lesser amplitude for stationary magnetic field generated by outer convection zone for Sun. This is a next reason for reality that the magnetic field source of the Sun should be mainly self-consistent dynamo.

Of course we should notice that by increase of the temperature, the electric conductivity will decrease and decrease of electric conductivity is reason to appear condition for gradual electronic flows in the convection zone by self-consistent dynamo. Then the reversal mechanism probably has been doing in the terrestrial planets when the outer core has been hotter and then self-consistent dynamo in the planets have been reduced before and prevailing mechanism is now rotation of the normal interior regions of the planets. But about the Sun, we see a current reversal and then strongly the

self-consistent dynamo is prevailing mechanism in the Sun in proportion to the normal body spinning magnetic field. In reality ever there are a complementary mechanism of the self-consistent dynamo and spinning normal body, aligned each other to generate celestial bodies magnetic field. Sometimes dynamo is prevailing and some times normal body spinning.

Referring to the above results and in detail to the book "MOED" (*Lutephy, 2016*), the universe expansion rate is dependent on the universal distribution of the number charges (universal electric potential energy) and percentage of the universe normal matter (equal number of electrons and protons) and also the density of universe and ultimately it is deduced that the universe expansion is not accelerating. The discovery of accelerating expansion led to the widespread acceptance of the idea that our Universe is dominated by a mysterious force called dark energy. But now physicists are questioning the conclusion, and they have a much larger dataset to back them up. Now, a team of scientists led by Professor Subir Sarkar of Oxford University's Department of Physics has cast doubt on this standard cosmological concept. Making use of a vastly increased data set – a catalogue of 740 Type Ia supernovae, more than ten times the original sample size – the researchers have found that the evidence for acceleration may be flimsier than previously thought, with the data being consistent with a constant rate of expansion. The study is published in the Nature Journal Scientific Reports by J. T. Nielsen, A. Guffanti and S. Sarkar (*Nielsen et al., 2016*).

In the book "MOED" (*Lutephy, 2016*) we have a pure argument for electric charge asymmetry at the Earth position correlated to the universal electric potential energy obtained by largest material concentration in the universe for Earth which it is local supercluster "the Laniakea" discovered newly. The Laniakea Supercluster is the galaxy supercluster that is home to the Milky Way and approximately 100,000 other nearby galaxies. it was defined in September 2014, when a group of astronomers including R. Brent Tully of the University of Hawaii, Hélène Courtois of the University of Lyon, Yehuda Hoffman of the Hebrew University of Jerusalem, and Daniel Pomarède of CEA Université Paris-Saclay published a new way of defining superclusters according to the relative velocities of galaxies. The Laniakea Supercluster is largest concentrated local structure at the observable universe so that such a concentrated matter can generate noticeable scalar electric potential to generate electric charge asymmetry at the Earth

position emerged by the electric binding energy of the quarks at the proton (*Lutephy, 2016*) arriving to the below formula that:

$$q_{e-p}^{\&} = e\frac{\sqrt{M_p/R_p}}{\sqrt{\sqrt{2M_{Laniakea}}}} \cong 2.5 \times 10^{-37} C\,. \tag{41}$$

So that M_p is the proton mass and R_p is the proton radius and e is fundamental electric charge.

In reality the electric charge asymmetry is not at the same value everywhere in the cosmos suppose it may be different in different positions and also the electric charge asymmetry is not ever constant in time suppose at different times maybe different in size, reasonable for inflation theory (*Guth, 1997*) discussed in detail at the book "MOED" (*Lutephy, 2016*).

Inflation is a theory of exponential expansion of the space in early universe. Inflation was a hypothetical very brief episode of highly accelerated expansion enable to explain some features of the universe as noted by Alan Guth himself that:

"I will begin by giving a quick rundown of how inflation works... The key idea – the underlying physics – that makes inflation possible is the fact that most modern particle theories predict that there should exist a state of matter that turns gravity on its head, creating a gravitational repulsion. This state can only be reached at energies well beyond those that we can probe experimentally, but the theoretical arguments for the existence of the state are rather persuasive. It is not merely the prediction of some specific theory, but it is the generic prediction for a wide class of plausible theories. Thus, gravity does not always have to be attractive. The gravitational repulsion caused by this peculiar kind of material is the secret behind inflation. Inflation is the proposition that the early universe contained at least a small patch that was filled with this peculiar repulsive-gravity material. There are a variety of theories about how this might have happened, based on ideas ranging from chaotic initial conditions to the creation of the universe as a quantum tunneling event... Once the patch exists it starts to rapidly expand because of its internal gravitational repulsion."

And in relation with Alan Guth inflation theory (*Guth, 1997*) we see here that the matter is possible to be transferred between the gravity and antigravity in different conditions appropriate for inflation theory. Manifestly

early universe has been different highly and then the charge asymmetry in early universe has been very different in size and in reality we obtain that the charge asymmetry is much bigger in early universe in agreement with inflation theory.

4. Conclusion

Experimental results in laboratories and phenomenological results in the solar system and the cosmos, are showing the evidences of the fundamental electric charge asymmetry as the origin of a section of the planets and stars magnetic field accompanied with self-consistent dynamo. Also we see that the electric charge asymmetry as a difference between electron and proton electric charges is responsible for many number of the planetary and cosmological big unsolved puzzles. For example, Cosmic microwave background anisotropy and expanding universe and accelerating expansion of the universe and solar wind and solar wind acceleration and Sun's corona and missing neutrinos and inflation theory and singularity paradox and comets plasma tail direction and pendulums mysterious precessions. Too we have suitable interpretations for some mysterious experimental results for example Nipher experiments electro antigravity and Eugene Podkletnov superconducting disk antigravity and also we have proposed some experiments to do in the laboratories.

Acknowledgements. We offer this article to the spirits of the scientists, Francis E. Nipher, Maurice Allais, Patrick Blackett, Eugene N. Parker, Erwin Saxl, Thomas Townsend Brown, Arthur Schuster, Herman Bondi and other relevant scientists who have developed the science by their hard trying.

References

Allais M., 1959a: Should the Laws of Gravitation Be reconsidered? Part I – Abnormalities in the Motion of a Paraconical Pendulum on an Anisotropic Support. Aero/Space Engineering, 46–52.

Allais M., 1959b: Should the Laws of Gravitation Be reconsidered? Part II – Experiments in Connection with the Abnormalities Noted in the Motion of the Paraconical Pendulum With an Anisotropic Support. Aero/Space Engineering, 51–55.

Allais M., 1999: The Allais effect and my experiments with the paraconical pendulum (1954–1960). Memoir C-6083 prepared for NASA (report).

Andrault D., Monteux J., Le Bars M., Samuel H., 2016: The deep Earth may not be cooling down. Earth and planetary science letters, **443**, 195–203.

Assis A. K. T., Silva H. T., 2000: Comparison between Weber's electrodynamics and classical electrodynamics. Pramana, **55**, 3, 393–404.

Bahcall J. N., 1964: Solar Neutrinos I. Theoretical. Phys. Rev. Lett. **12**, 300–302.

Biermann L., 1951: Kometenschweife und solare Korpuskularstrahlung. Zeitschrift für Astrophysik, **29**, 274 (in German).

Blackett P. M. S., 1947: The magnetic field of massive rotating bodies. Nature **159**, 658–666.

Blackett P. M. S., 1952: A negative experiment relating to magnetism and the Earth's rotation. Phil. Trans. R. Soc., **A 245**, 309–370.

Christensen-Dalsgaard J., Däppen W., Ajukov S. V., Anderson E. R., Antia H. M., Basu S., Baturin V. A., Berthomieu G., Chaboyer B., Chitre S. M., Cox A. N., Demarque P., Donatowicz J., Dziembowski W. A., Gabriel M., Gough D. O., Guenther D. B., Guzik J. A., Harvey J. W., Hill F., Houdek G., Iglesias C. A., Kosovichev A. G., Leibacher J. W., Morel P., Proffitt C. R., Provost J., Reiter J., Rhodes E. J. Jr., Rogers F. J., Roxburgh I. W., Thompson M. J., Ulrich R. K., 1996: The current state of solar modeling. Science, **272**, 5266, 1286–1292, doi: 10.1126/science.272.5266.1286.

Cowling T. G., 1934: The Magnetic Field of Sunspots. Monthly Notices of the Royal Astronomical Society, **94**, 39–48, doi: 10.1093/mnras/94.1.39.

Davis R. Jr., 1964: Solar Neutrinos. II. Experimental. Phys. Rev. Lett., **12**, 303–305.

Geiss J., Gloeckler G., Von Steiger R., 1995: Origin of the solar wind from composition data. Space Science Reviews, **72**, 1–2, 49–60, doi: 10.1007/BF00768753.

Gilman P. A., 2000: Fluid Dynamics and MHD of the Solar Convection Zone and Tachocline: Current Understanding and Unsolved Problems (Invited Review). Helioseismic Diagnostics of Solar Convection and Activity, p. 27.

Guth A. H., 1997: The inflationary-universe. Reading, Massachusetts, Perseus books, ISBN 0-201-14942-7.

Hillas A. M., Cranshaw T. E., 1959: A Comparison of the Charges of the Electron, Proton and Neutron. Nature, **184**, 892–893, doi: 10.1038/184892a0.

Jeverdan G. T., Rusu G. I., Antonescu V. I., 1961: Preliminary data about the behavior of a Foucault pendulum during the Sun eclipse of 15 February 15, 1961 (Date preliminare asupra comportarii unui pendul Foucault in timpul eclipsei de soare de la 15 februarie 1961). Annals of the Alexandru Ioan Cuza University, **7**, 2, 457 (in Romanian).

Jeverdan G. T., Rusu, G. I., Antonescu V. I., 1981: Experiments using the Foucault pendulum during the solar eclipse of 15 February, 1961 (PDF). The Biblical Astronomer, **1**, 55, 18–20.

Kamrin K., Koval G., 2012: Nonlocal Constitutive Relation for Steady Granular Flow. Physical Review Letters, **108**, 17, 178301, doi: 10.1103/PhysRevLett.108.178301.

Lutephy M., 2016: MOED: Modification of electric dynamics by Mach's inertia principle and electro anti-gravity. Edition 1st. ISBN: 9781537165691.

Lutephy M, 2018: Interplanetary external driven quasidynamo as the origin of geomagnetic jerks correlated with length of day and gravity anomaly. Contributions to Geophysics and Geodesy, **48**, 1, 23–74.

Lyttleton R. A., Bondi H., 1959: Physical consequences of a general excess of charge, Proc. Roy. Soc. Lond., **A252**, 1270, 313–333, doi: 10.1098/rspa.1959.0155.

Mach E., 1872: Die Geschichte und Wurzel des Satzes von der Erhaltung der Arbeit. Prague (in German).

Mach E., 1911: History and Root of the Principle of the Conservation of Energy. Open Court, Chicago.

Mach E., 1883: Die Mechanik in ihrer Entwicklung Historisch-Kritisch Dargestellt (in German).

Mach E., 1960: The Science of Mechanics. Open Court.

Michelson A. A., Morely E. W., 1887: On the relative motion of the Earth and the luminiferous Eather. American Journal of Science, **34**, 333–345.

Mishra D. C., Vyaghreswara Rao M. B. S., 1997: Temporal variation in gravity field during solar eclipse on 24 October 1995. Current Science, **72**, 11, 782–783.

Moffatt H. K., 1978: Magnetic Field Generation in Elecrically Conducting Fluids, Cambridge University Press.

Nielsen J. T., Guffanti A., Sarkar S., 2016: Marginal evidence for cosmic acceleration from Type Ia supernovae. Scientific Reports, **6**, 35596.

Nipher F. E., 1916: Gravitation and electrical action. Trans. Acad. Sci. St. Louis, 163–175.

Nipher F. E., 1917: Gravitational Repulsion. Trans. Acad. Sci. St. Louis, **XXIII**, 5.

Nipher F. E., 1918: Can Electricity Destroy Gravitation. Electric Experimenter.

Nipher F. E., 1920: New evidence of a relation between gravitation and electrical action and of local charges in the electrical potential of the Earth. Trans. Acad. Sci. St. Louis, **XXVII**, 383–387.

Parker E. N., 1958: Dynamics of the Interplanetary Gas and Magnetic Fields. The Astrophysical Journal, **128**, 1, 664, doi: 10.1086/146579.

Parker E. N., 1965: The dynamical theory of the solar wind. Space Science Reviews, **4**, 666–708.

Parker E. N., 2001: A history of the solar wind concept. The Century of Space Science, 225–255, Kluwer Academic Publishers.

Pippard A. B., 1988: The parametrically maintained Foucault pendulum and its perturbations. Proc. R. Soc. Lond., **A 420**, 81–91.

Podkletnov E., Nieminen R., 1992: A possibility of gravitational force shielding by bulk YBa2Cu3O7-x superconductor. Physica C, **203**, 3–4, 441–444.

Podkletnov E., Vuorinen P. T., 1996: Gravitation shielding properties of composite bulk YBa2Cu3O7-x superconductor below 70 K under electromatic field. Journal of Applied Physics D. Retrieved April 29, 2014.

Podkletnov E., 1997: Weak gravitation shielding properties of composite bulk YBa2Cu-3O7-x superconductor below 70 K under e.m. field. Retrieved April 29, 2014. This is believed to be substantially the same paper accepted for publication in 1996 by Journal of Physics D which was later withdrawn by the author.

Popescu V. A., Olenici D., 2007: A confirmation of the Allais and Jeverdan-Rusu-Antonescu effects during the solar eclipse from 22 September 2006, and the quantization of behaviour of pendulum. 7th Biennial European SSE Meeting. Røros, Norway, Society for Scientific Exploration.

Ryskin G., 2009: Secular variation of the Earth's magnetic field: induced by the ocean flow? New journal of physics, **11**, 6, 063015, doi: 10.1088/1367-2630/11/6/063015.

Sachs M., Roy A. R., Eds., 2003: Mach's Principle and the Origin of Inertia. Apeiron.

Sanders R. H., 1996: The Published Extended Rotation Curves of Spiral Galaxies: Confrontation with Modified Dynamics. The Astrophysical Journal, **473**, 1, 117–129.

Saxl E. J., 1964: An electrically charged torque pendulum. Nature, **203**, 4941, 136–138, doi: 10.1038/203136a0.

Schuster A., 1912: A critical examination of the possible causes of terrestrial magnetism. Proc. Phys. Soc. Lond., **24**, 121–137.

Sengupta S., Pal P. B., 1996: Constraints on cosmic charge asymmetry and neutrino charge from the microwave background. Phys. Lett., **B365**, 175–177, doi: 10.1016/S0370-2693(96)01532-8.

Sengupta S., 2000: Binary Pulsar PSR B1913+16 constraints the electron-proton charge asymmetry. Physics letters B., **484**, 3–4, 275–277.

Tarduno J. A., Cottrell R. D., Watkeys M. K., Hofmann A., Dobrovine P. V., Mamajek E. E., Liu D., Sibeck D. G., Neukirch L. P., Usui Y., 2010: Geodynamo, Solar wind, and magnetopause 3.4 to 3.45 billion years ago. Science, **327**, 5970, 1238–1240, doi: 10.1126/science.1183445.

Wang Q. S., Yang X. S., Wu C. Z., Guo G. H., Liu H. C., Hua C. C., 2000: Precise measurement of gravity variations during a total solar eclipse (PDF). Physical Review D, **62**, 4, 041101. arXiv: 1003.4947, doi: 10.1103/PhysRevD.62.041101.

Wilson H. A., 1923: An experiment on the origin of the Earth's magnetic field. Proc. R. Soc. Lond., **A 104**, 451–455.

Zhou S. W., Huang B. J., Ren Z. M., 1995: The abnormal influence of the partial solar eclipse on December 24th, 1992, on the time comparisons between atomic clocks. Il Nuovo Cimento C, **18**, 2, 223–236, doi: 10.1007/BF02512022.